Impact of Neutral Density on the Operation of High-Power Magnetically Shielded Hall Thrusters

by

Sarah Elizabeth Cusson

A dissertation submitted in partial fulfillment
of the requirements for the degree of
Doctor of Philosophy
(Aerospace Engineering)
in the University of Michigan
2019

Doctoral Committee:

Professor Alec D. Gallimore, Co-Chair
Assistant Professor Benjamin A. Jorns, Co-Chair
Professor John E. Foster
Dr. Richard R. Hofer

Far better it is to dare mighty things, to win glorious triumphs even though checkered by failure, than to rank with those poor spirits who neither enjoy nor suffer much because they live in the gray twilight that knows neither victory nor defeat.

–President Theodore Roosevelt

Sarah Elizabeth Cusson

cusson@umich.edu

ORCID iD: 0000-0002-0172-0750

For my father, who inspired me to be an engineer and my grandfather, who encouraged me to pursue my doctorate.

ACKNOWLEDGMENTS

While the culmination of doctorate studies results in a single-author dissertation, I doubt there are many in this world with PhDs who believe this task is possible alone. There are an incredible number of people who have shaped my path to this point, and they are all deserving of my gratitude and acknowledgement.

I must first and foremost thank my advisor, Dean Alec Gallimore. I had the privilege of having multiple advisors throughout my graduate career, however it was Alec who read my application to the University of Michigan and still thought it was a good idea to accept me. It was Alec who helped me formulate a research plan. He is an endless source of guidance and support. During some of the toughest moments of grad school, Alec was always there to remind me that I was going to get through it. His vision for the future continuously inspires me and I know I will continue to be inspired for years to come.

Professor Ben Jorns joined the university during my third year of graduate school and graciously became my co-advisor. I never understood how, as a first-year professor, Ben was able to advise nearly 10 PhD students. Regardless, he certainly pulled it off and turned us all into the researchers we are today. No doubt Ben has had the largest impact on the way I think about research and my writing style. Some of the biggest compliments I've received recently by colleagues are about the quality of my writing, and this is in large part due to Ben. Dr. Jorns is one of the smartest people I've ever met and knowing this has helped broaden my capabilities and the impact I have had on the field.

At the university, I technically had two advisor: Alec and Ben. However, I always tell people I had three advisors. Dr. Richard Hofer, at NASA's Jet Propulsion Laboratory, is truly my third advisor. My labmates always joke that if you don't know where Sarah is, she is probably in California at JPL. I recently calculated how long I spent at JPL throughout my graduate career, and cumulatively, it was approximately 9 months (a significant fraction). Rich is most responsible for my understand of how Hall thrusters work. I have learned an incredible amount from Rich. My success in graduate school can be linked directly to his guidance. He was always there for me (even when I was at UM) to take phone calls whenever something went wrong. I am honored to call Rich not only an advisor, but also a friend. I would also like to acknowledge Dr. John Foster for serving on my committee and providing invaluable feedback throughout my pre-defense and defense time.

My graduate career was financially supported by a number of sources. Most prominently, I was honored to serve as a NASA Space Technology Research Fellow supported under grant

number NNX15AQ43H and, as mentioned above, Dr. Rich Hofer. The NSTRF program (now called NSTRGO) is truly a one of kind fellowship and I encourage all first-years to apply for this opportunity. I also had the honor of receiving the Amelia Earhart Fellowship and the AIAA Orville and Wilbur Wright Graduate Fellowship which supported me throughout graduate school. The namesakes of these two fellowships embody the type of impact I hope to have on my community.

Beyond my committee and financial support, there are a number of people who contributed to this work. The H9 (and N30) build on over a decade of Hall thruster research, and the contributors to these programs are vast in numbers. Ray Liang developed the X2 and provided a vast number of reseach questions to be explored for NHTs. Dan Goebel fixed all the cathodes I broke and taught me so much throughout my time at JPL. Aaron Borgman, Chris Chartier, Cindy Collins, Tom Griffin, Jessica Jones, Courtney Krzyzaniak, Terry Larrow, Dave McLean, Kathy Miller, Kristin Parrish, Denise Phelps, Julie Power, J.P. Sheehan, Zackary Smith, and Eric Viges all helped my throughout my time at the University of Michigan. Kathleen Grimes, Alec's assistant, deserves a special shoutout. She took me in, like one of her own, and helped me with anything she could. Thank you for everything and letting me onto Alec's schedule even though he is the dean. There are many professors at the University that I had the pleasure of taking classes from. Bill Cleveland and the whole team at Precision Manufacturing Services in Ann Arbor machined the majority of the H9 and N30. The quality was incredible and they dealt with my unreasonable timelines with grace.

Considering that I spent close to 20% of my graduate school career at NASA JPL, there is a long list of contributors there as well. I would like to acknowledge: Giulia Becatti, John Bropy, Vernon Chaplin, Ryan Conversano, Lee Johnson, Ira Katz, Robbie Lobbia, Alejandro Lopez-Ortega, Arpine Margaryan, Yiangos Mikellides, Nowell Niblett, Jay Polk, and Steve Snyder. I'm sure there are others as well that I am forgetting. A special thanks goes Ray Swindlehurst who taught an engineer how to actually put things together. I spent some time at AFRL, NASA Glenn, and the Aerospace Corporation during my graduate career as well and I would like to thank everyone there for welcoming me and supporting my work.

When it comes to my peers at Michigan, the list of people who influenced me is quite lengthy. To those who were there when I arrived: Ethan Dale, Chris Durot, Frans Ebersohn, Scott Hall, and Kim Trent. Thank you for showing me how the lab works and being a source of insight and inspiration. During those early years, I spent most of my time with Ethan, Frans, Scott, and Marcel. Thank you for being an absolute joy to work with, making me want to come to the lab everyday, and quite literally traveling the world with me. While most of us have gone separate physical ways at this point, you know the special place you hold in my heart and I can wait for our reunion trip to Japan someday. You all have supported me endlessly, even if it meant sacrificing your work. And a special shoutout to Scott who took me under his wing my first year and taught me about nested Hall thrusters. Those who came after me: Zach Brown, Matt Byrne, Angela Kimber, Shad Hepner, Chris Sercel, Leanne Su, Ben Wachs, and Josh Woods have also helped tremendously throughout this experience. I have always enjoyed the incredibly sociable environment at PEPL and

I'm glad to see it continuing. There were many times you all helped me on my endless test campaigns and I can't thank you enough for it. Especially Matt and Josh who particularly understand the challenges of testing in LVTF. Leanne, I'm so glad such a capable and amazing human is continuing on this work. To all of PEPL: Continue making me proud and keep PEPL going strong. I would also be remiss to not mention Horatiu Dragnea from NGPDL who become my close friend and Hall thruster buddy. Finally, I was involved in a number of organizations on campus throughout my career. In particular, I would like to acknowledge GradSWE and WAA for providing a place to belong and make impact on campus.

Outside of school, my family was instrumental in my success and getting me to graduate school. To my parent, who let their 18 year old go to school in California and encouraged me to do whatever made me happy in life. To my grandparents, who continue to support and inspire me everyday. To my sister, Anthony, Colton, and Lila, who make me laugh continuously and provide endless support. To my new family, Liz, Marc, Ben, and Paul, who treat me like one of their own. Thank you. There is absolutely no doubt in my mind that I would be here today without all of you.

Finally, to my husband, Marcel. First and foremost, I won! More seriously, I barely know how to put into words your impact on not only this degree but my whole life. Fortunately for me (put perhaps unfortunately for you), we were in the same lab. That meant that you could always be my testing buddy staying at the lab late at night, always be my editor for both technical and grammatical mistakes, and always be my sounding board for when I was stuck in research. Your sacrifices for this work here are endless and uncountable. You've pushed me to become a better researcher and a better human. I can only hope that I can provide for you throughout your dissertation writing and graduation process, what you have done for me. You constant support and tolerance has been critical to my success. With everything I am and hope to become, I thank you.

Sarah E. Cusson, 2019

TABLE OF CONTENTS

LIST OF FIGURES

Figure

LIST OF TABLES

Table

LIST OF APPENDICES

NOMENCLATURE

Roman

A_{exit}	thruster exit area
B	magnetic field
d	diameter
E	Electric field
F_{dual}	X2 dual channel thrust
F_{th}	total thrust
F_{inner}	X2 inner channel thrust
F_{outer}	X2 outer channel thrust
$F_{ingestion}$	thrust due to neutral ingestion
F_{div}	thrust due to divergence changes
$f(u)$	ion velocity distribution function
I_b	beam current
I_{sp}	specific impulse
j	current density
L	length
$\dot{m}$	mass flow rate
n	neutral density
P	power
r	radial distance
r_L	Larmor radius
T	Temperature
$\bar{u}$	average velocity
u	velocity
V	voltage
V_{accel}	acccelerating voltage
z	axial distance

Greek

α_i	ionization probability
Γ	flux of background particle
γ_e	secondary electron emission yield
δv	change in velocity
η	total efficiency
η_b	beam utilization
η_c	cathode utilization
η_d	divergence utilization
η_m	mass utilization
η_p	power utilization
η_q	charge utilization
η_t	thrust divergence efficiency
η_v	voltage utilization
θ	divergence angle
ν	collision frequency
ϕ	azimuthal angle
Φ	potential
Φ_s	sheath potential
χ	mass flow fraction
Ω	Hall parameter
ω	cyclotron frequency

Subscripts (Unless Specified Above)

0	initial
$\parallel$	parallel (to field line)
a	anode
b	background (facility)
c	cathode
d	discharge
cc	cathode coupling
cg	cathode to ground
$cham$	chamfer (of discharge chamber)

e	electron
i	ions
ing	ingested
mag	magnet
OC	X2 outer channel
p	plasma
t	total
Xe	xenon

Constants

e	Elementary charge, 1.602×10^{-19} C
E_1	Threshold crossover energy, 40 eV
g	Earth's gravitational acceleration, 9.81 m/s^2
k_b	Boltzmann constant, 1.38×10^{-23} J/K
ϕ_0	Effective yield at zero energy, 0.54
m_{xe}	Mass of xenon atom or ion, 2.18×10^{-25} kg

Abbreviations

AEPS	Advanced Electric Propulsion Systems
AFRL	Air Force Research Laboratory
AR	Aerojet Rocketdyne
BaO	Barium Oxide
BN	Boron Nitride
BPT	Busek Primex Thruster
CFF	Cathode Flow Fraction
DSMC	Direct Simulation Monte Carlo
EP	Electric Propulsion
H6MS	Magnetically Shielded H6
HEFT	Human Exploration Framework Team
HERMeS	Hall Effect Rocket with Magnetic Shielding
IEDF	Ion Energy Distribution Function
IVDF	Ion Velocity Distribution Function

JIMO	Jupiter Icy Moons Orbiter
JPL	Jet Propulsion Laboratory
LaB_6	Lanthanum hexaboride
LIF	Laser-induced fluorescence
LP	Langmuir Probe
LVTF	Large Vacuum Test Facility
NASA	National Aeronautics and Space Administration
NextSTEP	Next Space Technologies for Exploration Partnerships
NHT	Nested Hall Thruster
OASIS	Orbital Aggregation and Space Infrastructure System
P2P	Peak-to-Peak
PEPL	Plasmadynamics and Electric Propulsion Laboratory
PID	Proportional, Integral, Derivative
RMS	Root mean square
SCCM	Standard cubic centimeters per minute
SHT	Single-channel Hall Thruster
SMART	Small Missions for Advanced Research in Technology
SPT	Stationary Plasma Thruster
TAL	Thruster with Anode Layer
UM	University of Michigan
XR	Xenon Rocket

ABSTRACT

High-power Hall thrusters (>5 kW) are enabling for a variety of space missions from near-Earth communication satellites to deep space human missions. Developments in the field have led to both an increase in the achievable power levels and the overall lifetime of these devices. Magnetic shielding increases the lifetime of Hall thrusters by three orders of magnitude, while nested Hall thrusters allow these devices to be scaled to the very high powers necessary for Mars missions. Despite these advancements, there remain open questions about the exact implications on Hall thruster operation. These open questions pose large risks for transitioning the thrusters to flight. One of the most critical is how neutral gas particles emanating from various sources influence the overall performance and lifetime of these thrusters. There exist several sources of neutrals such as the background facility pressure, the cathode, and adjacent channels on nested Hall thrusters.

This work examines the role neutrals can play on both the performance and lifetime of high power Hall thrusters. To begin, we provide a theoretical framework for how neutrals should impact these parameters. In particular, we detail how neutrals will shift the main acceleration region of the Hall thrusters resulting in a reduced divergence angle and increased thrust. We also discuss how this shift could lead to changes in the erosion profile of these thrusters. Previous results on nested Hall thrusters indicated that the performance in multi-channel operation was higher than the sum of each individual channel operating alone. We postulate that these difference are due to the increased neutral density when moving from single-channel to multi-channel operation. Again, the neutrals drive the acceleration region inward which improves the thrust. Additionally, neutrals from an adjacent channel can be ingested resulting in higher performance. We provide a framework to calculate the increased thrust due to both of these parameters.

In order to experimentally characterize these impacts, we use three Hall thrusters: the H9, a 9-kW magnetically shielded Hall thruster, the X2, a two-channel 10-kW nested Hall thruster, and the N30, a two-channel magnetically shielded 33-kW nested Hall thruster. We employ a variety of diagnostics including a thrust stand, a neutral pressure probe, a Faraday probe, and laser-induced fluorescence to measure the thruster properties in addition to the standard telemetry. Our results show that the acceleration region of Hall thrusters does shift with a change in neutral density. We show this shift is independent of the neutral source and the critical parameter is the neutral density at the exit plane. Crucially, we also show that this shift can lead to changes in performance. For nested Hall thrusters,

we show that the thrust improves 5% when moving from single channel to dual channel operation on the X2. This 5% increase is explainable by our theoretical framework which shows that this improvement is due to neutral effects. Finally, we show that the near-wall ion trajectories (for both single-channel and nested-channel magnetically shielded thrusters) are not substantially changed with varying local neutral density – indicating that the erosion profile of the thruster does not depend on the outside pressure environment substantially.

Ultimately, we have improved our understanding of the mechanisms behind neutral impacts on the performance and lifetime of magnetically shielded and nested Hall thrusters. This improves of fundamental understand of Hall thruster operation and decreases the risk for transitioning to flight. For nested Hall thrusters, we have expanded our understanding into the differences between them and traditional Hall thruster and increased the technology readiness level.

CHAPTER 1

Introduction

1.1 Introduction

In this chapter, we provide a description of the question investigated throughout this work as well as an overview of electric propulsion (Section 1.3). Particular emphasis is placed on Hall thrusters to better frame the problem statement. Section 1.4 describes, in brief, the advantages and types of Hall thrusters as well their basic operation. Next, Section 1.4.3 describes recent innovations and on-going challenges in the Hall thruster research and development community. Finally, we present a full motivation for the development of very high power electric propulsion and specifically Hall thrusters. To end, we detail the organization and objectives of the work presented herein.

1.2 Problem Statement

According to NASA's *In-Space Propulsion Technologies Roadmap* [7], one of the goals for electric propulsion research in the coming years is to increase the maturity of higher-power thrusters as well as improve the lifetime of these systems. Historically, Hall thrusters have suffered from lifetime issues that limited their applicability for deep space missions. [8–17] However, recent advances in the field have successfully demonstrated a life-prolonging technology. [3, 18–20] This advancement has opened up a new and exciting mission space for Hall thrusters. The technology, called "magnetic shielding," is predicated on the ability

to carefully control the shape of the magnetic field and the location of the plasma as well as maintain state-of-the-art performance throughout the thrusters' lifetime.

Despite the fact that this technology has been shown to increase thruster lifetime by up to three order of magnitudes, there remain open questions about the exact implications of this new magnetic field configuration on Hall thruster operation. For example, traditional Hall thrusters, i.e. those without shielding, are known to be impacted by ground test facilities. [21–25] That is to say that the thrusters operate differently in-orbit as compared to ground testing. This change is attributed to the finite pressure present in vacuum chambers. Many parameters are known to be influenced; however, one of the most critical is the movement in the location of the bulk plasma which can affect the performance of thrusters and its interactions with spacecraft. [6, 26, 27] More pivotal is that movement of the plasma due to changes in neutral density has the potential to impact the lifetime of Hall thrusters. Hall thrusters employing magnetic shielding are not immune to these effects. [28] The fundamental mechanism driving these changes is not predicted by our current understanding of Hall thruster physics making them challenging to understand. Furthermore, due to the limitations of ground testing facilities, these problems become amplified when scaling devices to high power.

Beyond neutrals existing in the background of our ground test facilities, there exists a second pertinent example. Next generation thrusters, such as nested Hall thrusters (NHTs), offer another source of neutrals that may impact thruster operation. These thrusters concentrically nest multiple discharges together and can be operated in single- or multi-channel mode. In multi-channel operation, adjacent channels act as a significant neutral source. Indeed, studies have shown shifting the location of the plasma depends on how many channels are operating. [6] Ultimately, this implies that similar to traditional Hall thrusters, magnetically shielded NHTs could suffer lifetime and performance changes

depending on the near-field neutral density. Thus, it is critical for Hall thruster technology (traditional and nested) to understand and quantify the impact these differences in operation have on magnetically shielded Hall thrusters and potential mechanisms to mitigate them.

1.3 Electric Propulsion

1.3.1 Motivation

The ability to travel in space is based on the capability to impart a sufficient change in velocity on the spacecraft. This capability is dictated by the rocket equation, $\Delta v = u_e \log\left[\frac{m_0}{m_f}\right]$, where Δv is the change in velocity, u_e is the exhaust velocity of the propellant, and m_0 and m_f are the initial and final masses respectively. Typically, the Δv is "set" by given mission parameters, such as destination. Therefore, there is an intrinsic link between the delivered mass (m_f) and the exhaust velocity of the propulsion system. Higher exhaust velocities are desired because less of the initial mass is dedicated to propellant (aka higher "fuel efficiency"). Therefore, a high exhaust velocity leads to a larger delivered mass. Because of this, a plethora of earth-orbiting and deep space missions are enabled by thrusters with high exhaust velocity. [8]

Electric propulsion (EP), at its core, uses external electric power to increase a propellant's exhaust velocity as opposed to the more traditional chemical propulsion, which releases the internal energy held in chemical bonds through reactions. More specifically, EP typically uses electric and magnetic fields to ionize and/or accelerate a propellant in order to impart momentum on a spacecraft. The main motivation for studying electric propulsion systems is that chemical propulsion has inherent and insurmountable limitations to its exhaust velocity. This upper bound stems from the available specific energy in the bonds of propellants used for these systems. This limit places the highest achievable exhaust velocity using chemical propulsion at about 5 km/s. More practically, there are also limitations to

the pressure and temperatures the materials of the combustion chamber and nozzle can handle. Electric propulsion, on the other hand, does not have this limitation as all the energy/acceleration imparted on the propellant is delivered from an external source. Thus, there is no inherent upper bound to the thruster's achievable exhaust velocity. The limit is based on available electric power on orbit. Because of this advantage, exhaust velocities an order of magnitude higher than chemical propulsion (up to 50 km/s) are easily achievable.

1.3.2 Types

There are three main types of electric propulsion: electrothermal, electrostatic and electromagnetic. Each of their respective names stems from the accelerating method. Electrothermal thrusters, for example, typically resistively heat a propellant and then expand it out a conventional converging-diverging nozzle. Of the three classes of electric propulsion, electrothermal thrusters are the closest to traditional chemical systems and thus tend to have the lowest performance, with typical specific impulses (a proxy for exhaust velocity) of 300-600 seconds. [8] However, their simplicity often makes them attractive for certain space missions, since they have improved performance over many chemical systems. [29, 30] Examples of electrothermal thrusters include resistojets and arcjets. Electrostatic thrusters use a static electric field to accelerate an ionized propellant. Thus, they use the Coulombic (electrostatic) force. These devices can range from 1000 to 10000 seconds of I_{sp} and are the class of electric propulsion most widely implemented in space missions. Ion engines, Hall thrusters, and electrospray thrusters are common examples of electrostatic EP devices. Finally, electromagnetic thrusters use magnetic and electric fields to accelerate ionized propellant. Similar to electrostatic thrusters, they also have a wide range of performance. Examples include pulsed plasma thrusters, magnetoplasmdynamics thrusters, and field-reversed configuration thrusters. While there are a wide variety of thrusters in the electric propulsion space, ion engines and Hall thrusters have, by far, been the most studied thruster types in the United

States for the past twenty years. This is likely because ion engines and Hall thrusters excel in the power and size ranges that have historically been practical and available on orbit.

Figure 1.1 shows the trade-off between thrust and specific impulse for a variety of chemical and electric propulsion systems. The chart highlights the capabilities of both Hall and ion thrusters. The entirety of the work described here is focused on Hall thrusters.

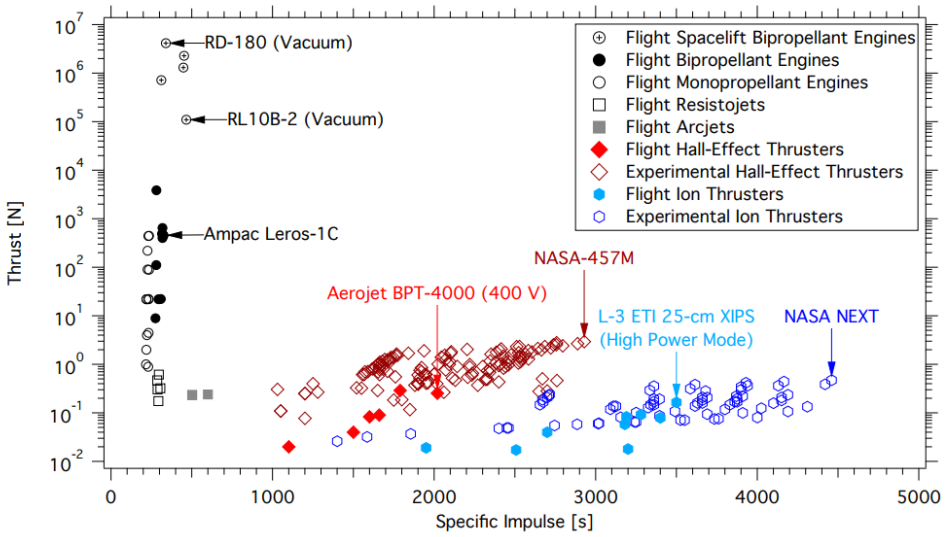

Figure 1.1: Specific impulse ($u_e = g_0 I_{sp}$) versus thrust for a variety of chemical and electric propulsion types. Reproduced from Liang [1].

1.4 Hall Thrusters

1.4.1 Advantages and Types

Hall thrusters are a type of electric propulsion that use a crossed electric and magnetic field to ionize and accelerate plasma. Research on Hall thrusters has been on-going since the 1960s, and these thrusters have been flying since the 1970s. [16, 31–33] There are two main sub-types of Hall thrusters: the stationary plasma thruster (SPT) and the thruster with anode layer (TAL). The main differences between the two types is that TALs have spatially

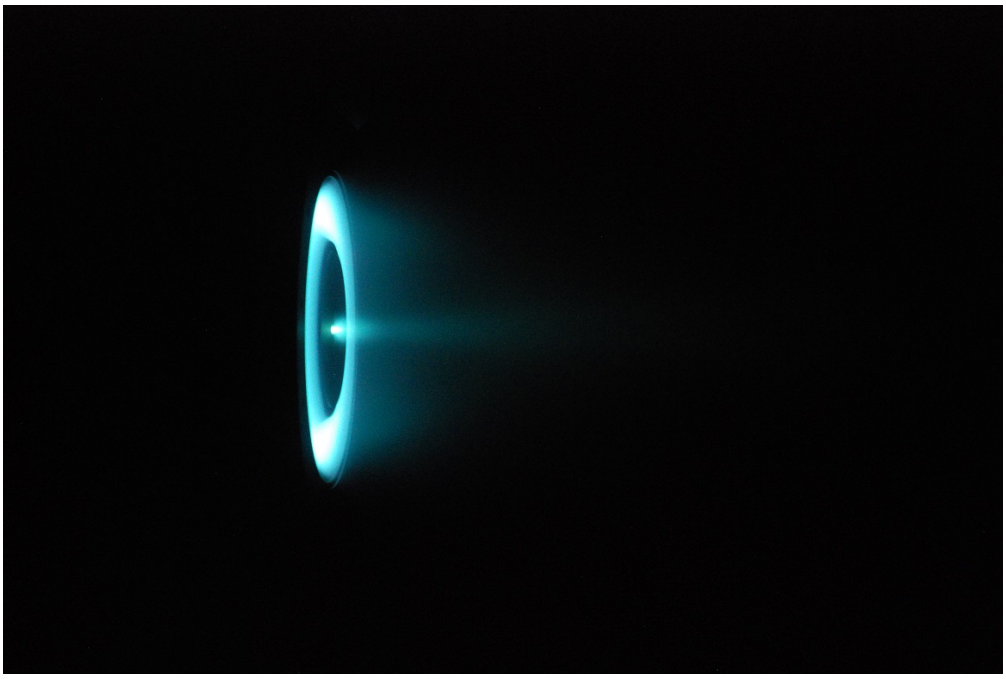

Figure 1.2: A picture of the H9 Hall thruster operating at 4.5 kW with xenon propellant.

shorter electric fields and metallic walls whereas SPTs typically have dielectric walls. [34] The majority of the early work on both thruster varieties, as well as all early flights, occurred in the Soviet Union. However, the end of the Cold War (in the 1990s) made it possible for the technology to be transfered from the Soviet Union to the United States. Early efforts focused on the SPT-100 Hall thruster, which is a 1.35 kW stationary plasma thruster. [35, 36] Since the majority of Hall thruster research in the United States has focused on SPT-type Hall thrusters, the work herein only focuses on those. Based on the success of initial research, in addition to early flight tests, research on Hall thrusters in the United States has flourished since the 1990s. Since then, research worldwide on Hall thrusters has expanded their power ranges down to 100 W and up to 100+ kW. [37–43] Beyond the mission benefits that many electric propulsion systems offer, there are a few key advantages Hall thrusters provide over other electric propulsion devices that have contributed to their widespread use and study. One advantage is that their geometry is quite simple and thus implementation is more straight-forward. Another is that, compared to ion engines, this simple geometry reduces

the number of power supplies and complexity of the system. Additionally, Hall thrusters typically produce higher thrust densities as compared to ion engines because there is no space-charge limit effects. Finally, many missions (as well as Hall thrusters) optimize for specific impulses of 1000-3000 seconds, which is lower than ion engines typically produce.

1.4.2 Basic Operation

A schematic of a typical Hall thruster is seen in Figure 1.3. These devices, which are axisymmetric, have four major components: the cathode, the anode, the discharge chamber, and the magnetic circuit. The cathode is the electron source for the primary thruster discharge and neutralizes the ion beam being exhausted. Due to efficiency, lifetime, and heater power considerations, most Hall thrusters (and ion engines) use a hollow cathode. [8, 44–46] The cathode uses a low work function material (typically BaO or LaB_6) to extract electrons by thermionic emission. A heater is used to begin the emission process; however, once the plasma inside the cathode has been started, these hollow cathode are self-heating and do not require any additional heat in steady-state mode. The "hollow" design also reduces the sheath voltage at the cathode, thus limiting the amount of voltage required to extract electrons. An electric field (as depicted in Fig. 1.3) is established between the anode and the cathode. Therefore, electrons born in the cathode region are attracted toward the anode. The magnetic circuit of thruster creates a roughly radial magnetic field that peaks in magnitude near the exit of the discharge chamber, where the bulk plasma resides. Electromagnets are used to control the strength and shape of this field. The motion of the electrons towards the anode is impeded by this magnetic field. Due to the $\boldsymbol{E} \times \boldsymbol{B}$ force, the electrons are trapped in an azimuthal motion around the channel of the thruster. In most Hall thrusters, the anode is located at the back of the discharge chamber. The entire discharge chamber is isolated from the remainder of the thruster using ceramic walls. Typically, the anode also serves as the neutral gas injector. Neutral gas injected through the anode is ionized via electron-impact ionization by the electrons trapped in the $\boldsymbol{E} \times \boldsymbol{B}$ drift. The ions are then

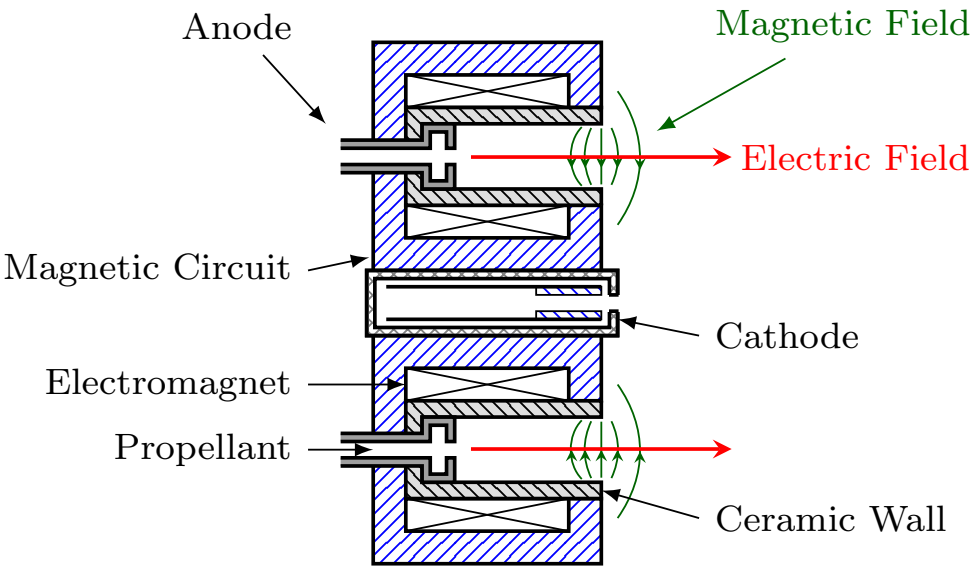

Figure 1.3: Schematic of a stationary plasma thruster type Hall thruster detailing all critical components.

accelerated out of the thruster by the axial electric field and neutralized by electrons from the cathode. Critical to this entire process is that $r_{L,e} \ll L \ll r_{L,i}$, where $r_{L,e}$ is the Larmor radius of electrons, L is the characteristic length scale of the thruster geometry, and $r_{L,i}$ is the Larmor radius of the ions. Under these conditions, the electrons are magnetized, or trapped along magnetic field lines, but ions are not. It also follows that for the electrons to be sufficiently impeded by the magnetic field to reside in the discharge chamber and not simply stream to the anode, the electron Hall parameter, $\Omega_e = \frac{\omega_e}{\nu}$, where ω_e is the cyclotron frequency and ν is the effective collision frequency, must be large ($>> 1$). That is to say, the electrons must gyrate about magnetic field lines many times before collisional processes induce an axial drift towards the anode. Typically, in Hall thrusters, these transport processes include particle collisions, wall collisions, or non-classical mechanisms. [47] An additional requirement is that the residence time of electrons in the discharge chamber is significantly

longer than the ionization timescale such that a significant portion (> 50%) of the incoming neutrals are ionized. [10, 48]

1.4.3 Challenges and Recent Innovations

Since the beginning of Hall thruster research, there has been many innovations that have improved the technology, yet there remain key challenges to overcome. While not exhaustive, here we focus on the improvement in performance and lifetime as key innovations and facility effects and scaling to high power as current challenges.

1.4.3.1 Performance

For many of the early decades of Hall thruster research, the devices were considered to be capable of 1000 to 2000 second of I_{sp}. [49] However, studies for mission concepts indicated performance up to 3000 seconds was highly desirable. [35, 36, 38, 50, 51] Advantages included greater payload delivery and shorter trip times. Thus, considerable efforts were undertaken to improve the specific impulse of these devices in the late 1990s. While many concepts were investigated, such as alternative geometries and ionization methods [52–54], a change in the shape of the magnetic field ultimately led to the development of high-specific impulse, high efficiency Hall thrusters. [2, 55, 56] The new magnetic field configuration, referred to as a "magnetic lens," directed ions away from the walls, increased the average path length and Hall parameter for the electrons, and focused the ion beam on discharge chamber centerline which reduced the divergence of the thrusters. [55] This advancement led to the demonstration of 3400 seconds of specific impulse at 61% efficiency on the NASA-172Mv2 Hall thruster. [2] These new performance metrics expanded the applicability of Hall thrusters and renewed research interest in these devices.

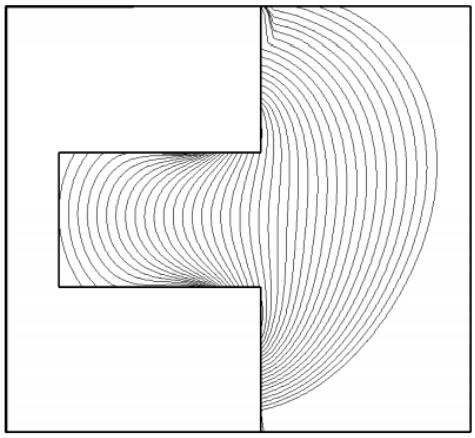

Figure 1.4: The magnetic lens topography of the NASA-173M. Reproduced from Hofer et al [2].

1.4.3.2 Lifetime

Erosion of the discharge chamber walls of a Hall thruster due to ion bombardment has historically been the life-limiting factor that has prevented this technology for being used in long-duration, deep space exploration. [11, 12, 15, 57–60] This erosion has previously limited lifetimes to approximately 10000 hours. Advances in Hall thruster lifetime have in part stemmed from a serendipitous result. During a wear test of the XR-5 Hall thruster by Aerojet Rocketdyne, the thruster eventually entered a "zero-erosion" state. [61] In 2011, NASA's Jet Propulsion Laboratory (JPL) subsequently performed numerical simulations that uncovered the physics behind this state. [18] Afterwards, a retrofit of the H6 Hall thruster experimentally verified this new magnetic field configuration, coined "magnetic shielding," leading to a reduction in discharge chamber erosion of three orders of magnitude. [3,19,20,62] This decrease in erosion came with only a small change in performance. [20] This topology is depicted in Fig. 1.5 along with the more traditional, unshielded configuration. Using this magnetic field structure leads to a relatively flat potential structure along the wall. In turn, this yields ions in the wall region with low kinetic energy. Additionally, it reduced the electron temperature near the wall as well as the sheath potential. In combination, these two properties result in ion impact energies on the discharge chamber walls that are below

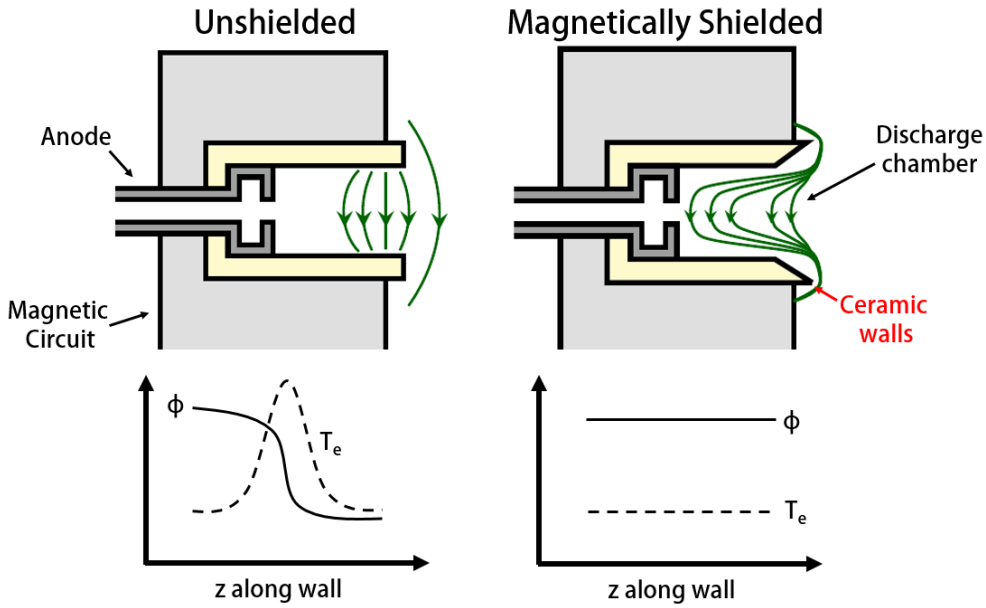

Figure 1.5: Schematic showing the difference between unshielded and magnetically shielded Hall thrusters. Adapted from Mikellides et al. [3]

the sputtering threshold of most wall materials. [19] This advancement in technology has led to Hall thrusters being a viable technology for deep space flight.

1.4.3.3 Facility Effects

One of the active areas of research in the community is "facility effects." These are known changes in thruster operation when comparing ground test results with on-orbit data. This change is thought to be the result of non-vanishing background pressure and grounded facility walls. Examples of known facility effects include changes in thrust and bulk plasma location with varying background pressure. Previous studies have shown that all configurations of Hall thrusters are impacted by the facility, including thrusters with externally or internally mounted cathode and shielded as well as unshielded thrusters. [21, 22, 24, 26, 28, 63] However, there is evidence that thrusters with externally mounted cathodes (the current most common flight configuration) are the most susceptible to these changes. [64] The ultimate implication is that there is a potential risk that thruster behavior could be sub-optimal or even unstable

in orbit. This risk is compounded by the fact that the dependence of thruster operation on facility effects is not well-understood. This makes the prediction of the transition from ground to flight particularly challenging. As shown in Fig. 1.6, the main parameters of the thruster

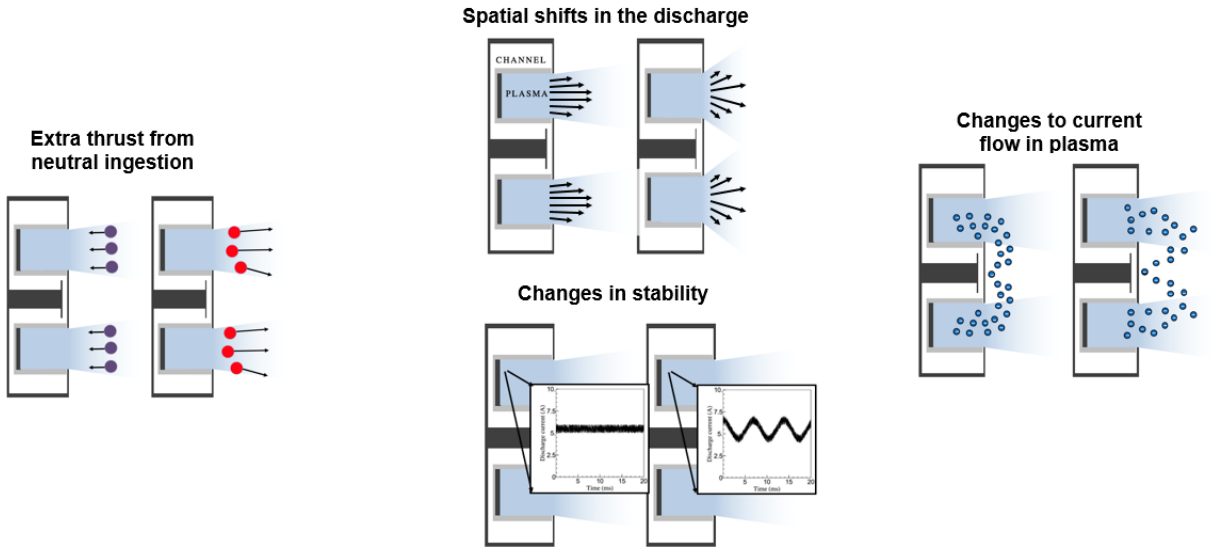

Figure 1.6: A qualitative description of facility effects and their impacts on thruster behavior.

known to be impacted by the facility are the location of the acceleration region, the thrust, the cathode coupling voltage, and the amplitude of oscillations. Accordingly, this impacts the overall efficiency and specific impulse. Understanding the underlying mechanisms and physics behind these effects is a critical need for predicting flight performance based on ground-facility testing.

1.4.3.4 Scaling to High Power

Although state of the art electric propulsion systems flying today are currently limited to operating powers less than 4.5 kW, there are a number of enabling, near and long-term architectures that could be realized if the available power was expanded to 100s of kWs. [65–67] These missions include Mars cargo missions. [68–70] NASA views the development of these higher power electric propulsion systems as critical for its mission and has supported them through the NextSTEP technology development program and the

Advance Electric Propulsion System. [65, 71]

Despite this desire, scaling the technology to high power is not trivial. One option is to cluster many smaller thrusters together. However, the added complexity of power and propellant management quickly raises mass and cost. [72] On the other hand, a single-channel very high power thruster is also impractical. This is because of known scaling laws which dictate the overall channel width, thruster diameter and current density. Thus, a single-channel very high power thruster (> 100 kW) would be massive in both size and mass, challenging or impossible to manufacture, and would likely be prohibitively expensive to build and flight qualify. Therefore, alternative means to scale to high-power, such as nesting discharge channels, are current areas of investigation. A diagram of single versus nested Hall thrusters is shown in Fig. 1.7. These devices concentrically nest multiple discharges together to scale Hall thrusters to high power with maintaining lower specific mass and areas than traditional Hall thrusters at the same power level. A full description of the devices is provided in Chapter 3. Now that we have presented the history and challenges associated with Hall thruster development, we aim to focus primarily on scaling these devices to high power. To this end, we provide a more detailed mission-driven motivation for this research in the next section.

1.5 Case for High Power Electric Propulsion

Before we can discuss the merits of high-power Hall thrusters, we must first discuss the community's desire to pursue high power electric propulsion. In general, we can separate space missions into three categories: Earth orbiting and near-Earth, deep space, and human missions. For each of these categories, requirements may vary with respect to trip time, mass delivered, flexibility, and cost. For Earth orbiting and near-Earth missions, cost and mass delivered usually drive requirements. For deep space missions, mass delivered and

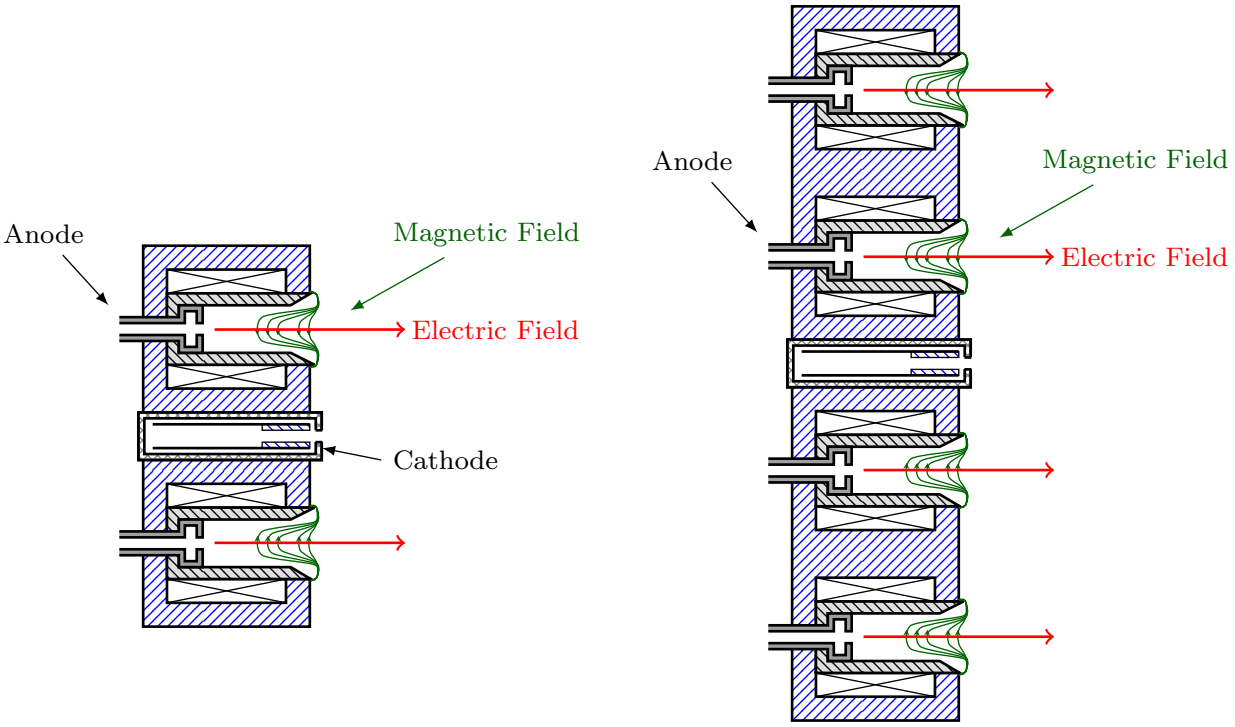

(a) Traditional Hall thruster

(b) Nested Hall thruster

Figure 1.7: Comparison between a single channel (left) and nested channel (right) Hall thruster.

total trip time are most critical. Finally, for human missions, trip time, mass delivered and flexibility drive requirements. While one could make the case for high power electric propulsion for all three of these classes as an enabling technology, here we will focus on where they truly shine: large deep space missions and human/human-support missions. This is because, as compared to chemical propulsion, electric propulsion generally offers much higher delivered payload and can often reduce trip times.

Traditional electric propulsion has been leveraged on missions with power supplies up to 50-kW total system power. [66, 67] These missions include hundreds of Earth-orbiting satellites deep space missions such as Deep Space 1 [73], SMART-1 [74], Hayabusa [75], and BepiColombo [76]; and planned deep space missions such as the Deep Space Gateway [67] and Psyche [77]. While these thrusters suit many different mission architectures well, there

exist a plethora of missions above 50 kW that these lower power (<20 kW) thrusters are not suited for. These high-power missions include Mars and Moon cargo missions [68–70], human missions to Phobos and Deimos [78], and missions to near-Earth asteroids [4], among others. A recent study identified a viable architecture for a solar electric human mission to Mars. [79] In the 2000s, NASA developed a mission concept called Orbital Aggregation and Space Infrastructure System (OASIS) that considered a crewed mission to the Earth-Moon L1 Lagrange point. [70] This mission was enabled by a 584-kW solar electric propulsion system with 50-kW thrusters. High specific impulse thrusters (3300 seconds) allowed the spacecraft to be launched in the space shuttle cargo bay (60000 kg lift capacity) with a payload of 36500 kg. [70] This implies that over half of the spacecraft would have been payload, something unlikely to occur using traditional chemical propulsion. Another example is the Human Exploration Framework Team (HEFT) in 2011 which proposed a 300 kW electric propulsion system with 43 kW thrusters and the capability for multiple destinations. [70] A review of literature finds an abundance of similar human mission architectures that baseline high-power (greater than 100 kW total power) solar electric propulsion.

For large deep space missions, solar electric propulsion is likely not possible due to the decrease of power from the solar array as the spacecraft travels away from the sun. Thus, we turn to nuclear-powered electric propulsion. A prime example of a mission enabled by this technology is the Jupiter Icy Moon Orbiter (JIMO). The mission was part of NASA's Prometheus project with the intention of developing nuclear-powered spacecraft in the 2000s. [80] The goal of the program was to enable high power deep space missions with increased spacecraft longevity and range. Nuclear electric propulsion was seen as enabling to many science goals including the outer planet orbiters. [81] These missions were always multi-hundred kilowatt missions. Not only did high-power electric propulsion systems enable these high Δv missions with great scientific value, they also offer the added benefit of significantly reduced trip times. Based on the above evidence, the case for the

development of high-power (greater than 50 kW) electric propulsion systems is clear.

In order to scale electric propulsion systems above 50 kW, one might think we could simply keep adding more smaller thrusters to the spacecraft to increase the power level. However, work done by Hofer and Randolph [72] showed that there is an optimum number of thrusters for an electric propulsion system. This is due to a trade-off between fault tolerance and the increase in mass and cost necessary to support multiple strings. In this work, they considered both mass and cost for analysis. For the mass model, they included three main terms: the total system power, the number of thruster strings and the number of redundant thrusters (i.e. fault tolerance). The major components for each thruster string included the xenon flow system (tank, regulators and flow controllers), the power processing unit, the thruster system (thruster and gimbal), and cabling and structure fractions. They considered both non-recurring expenses, such as thruster development and qualification, as well as recurring costs, such as string component costs and launch costs. Overall, their results indicated that thrusters capable of 20-100 kW are best suited for missions ranging from 50 kW to 1 MW. They put forth the recommendation to develop two systems: a 20-50 kW thruster for missions up to 500 kW and a 50-100 kW system for missions up to 1 MW. A critical consideration is that current ground facilities are unlikely to be able to test thrusters larger than 100 kW. The development of such a facility to accommodate this would be over $100 million. Therefore, thrusters less than 100 kW are desirable. [72] Finally, they note that Hall thrusters are the strongest candidate for scaling electric propulsion systems to these power levels. In particular, they state that nested Hall thrusters likely become competitive in the 50-100 kW per thruster range. [72]. Thus, the impetus is clear for the development of higher (30-100 kW) power, individual, electric propulsion thrusters.

1.5.1 Advances in Power Technology

The use of high-power electric propulsion in space is quickly coming to fruition. With the advancement of solar cell technology, a 50-kW class electric propulsion string is now feasible. The electric propulsion system being developed for the Deep Space Gateway is a 40-kW Hall thruster system. [65–67] However, above these power levels, we must also consider available power on orbit. While we may be able to make efficient high-power propulsion systems, the entire program is moot should the power not be available. There are two main options for power in space: solar and nuclear. Many of the missions discussed above range from 50 kW to 1 MW+, and the availability of this type of power from solar arrays may be realizable. For instance, the International Space Station receives over 100 kW of solar power. Figure 1.8 shows the historical trends of available solar power in space. [4] There may be a viable option for high power solar arrays. However, we do note that continued development to increase both the efficiency and the power density of solar panels would be enabling for many electric propulsion missions, as the total area of the solar panels must remain reasonable.

For deep space missions in particular, solar power is an inconvenient option. Based on a study from Strange et al [82], a 30 kW array at Earth would produce just 943 W at Jupiter. However, certain thruster configurations, such as nested Hall thrusters, may be suited to exploit this inefficiency. Traditional, single discharge thrusters sacrifice performance significantly when throttling to power levels much lower than their design. In general, Hall thrusters can only maintain >50% efficiency over a narrow power range (a throttling range from minimum to maximum power of 3X). [83]. This means that a 30-kW Hall thruster (at Earth) would have significantly reduced performance below 10 kW. Alternatively, consider a two-channel 30-kW nested Hall thruster with an inner channel of approximately 7.5 kW and an outer channel of approximately 22.5 kW. Since the thruster can run with only the inner channel on, performance is not significantly reduced until 2.5 kW. Thus, NHTs may

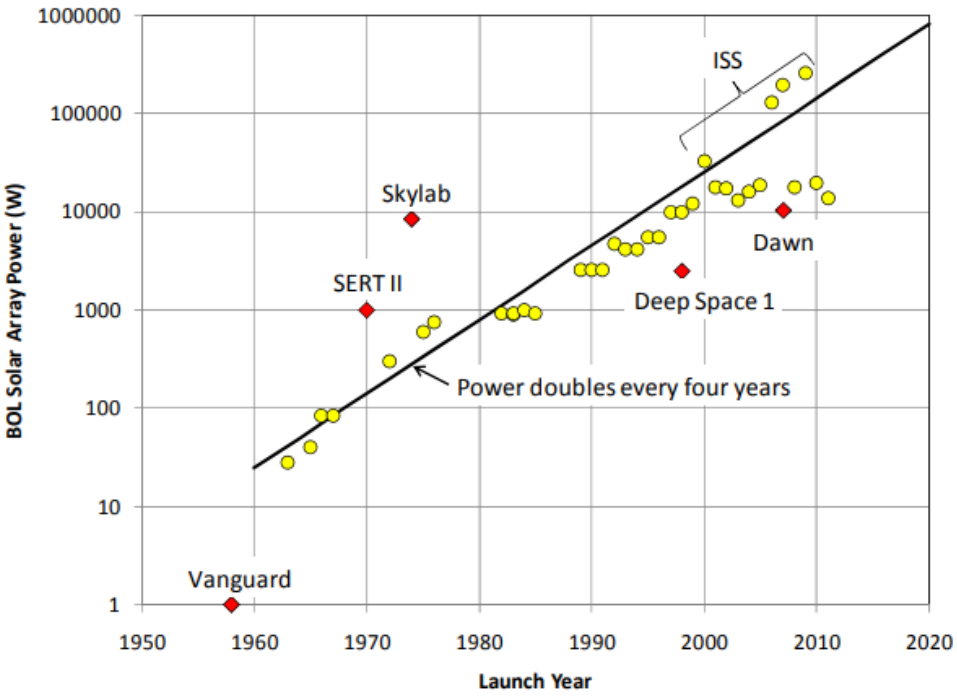

Figure 1.8: History of Available Solar Power in Space. Reproduced from Ref [4].

enable deeper than usual solar missions with a wide throttling range on a single thruster. Regardless, very deep into the solar system, solar panels are not an option, [84] and high power nuclear options must continue to be developed, such as the NASA Kilopower program. [85] Nonetheless, based on current technology available, the on-orbit power is reaching levels that make high power electric propulsion possible.

1.6 Objectives and Contributions

The primary objective of this work is to investigate the impact of neutrals on the operation of high-power magnetically shielded Hall thrusters. In order to enable this investigation, the development of laboratory testbeds for this investigation was necessary. Thus, the main subsections of this project were

1. The development of a single channel magnetically shielded Hall thruster,

2. An investigation of the response of this thruster to neutrals,

3. An investigation of neutral interactions in unshielded nested Hall thrusters,

4. The development of a two channel magnetically shielded nested Hall thruster, and

5. An investigation of the impact of neutrals emanating from other channels in magnetically shielded nested Hall thrusters.

Beyond addressing these objectives, the additional unique contributions of this work to the field of electric propulsion include (but are not limited to):

1. The demonstration of magnetic shielding in nested Hall thrusters. These results justify the viability of nested Hall thrusters for deep space missions.

2. The explanation of improvements in performance of nested Hall thrusters operating in multi-channel mode when compared to single channel mode.

3. The first investigation of novel methods to limit the impact of facility neutrals when transitioning to flight.

1.7 Organization

In order to disseminate the results of these investigations, this work is organized as follows: Chapter 2 provides the theoretical framework for the impact of neutrals on single channel Hall thrusters, while Chapter 3 provides the theoretical framework for the impact of neutral density on nested channel Hall thrusters. Chapter 4 provides a description of the experimental equipment used during these investigations. Specifically, it provides a description of all the thrusters used (the H9, the X2, and the N30) and their cathodes, the facility used (Large Vacuum Test Facility), and all the diagnostics used. It also discusses the development of the H9 and N30 and why they were necessary for this investigation.

Chapter 5 describes the investigation into neutral consequences on single-channel magnetically shielded Hall thrusters. Specifically, it focuses on the movement of the acceleration region in the H9 and the traceable changes in performance. It also discusses the potential impact of neutrals on the lifetime of magnetically shielded Hall thrusters. Chapter 6 details the investigation of neutrals interactions in nested Hall thrusters. Specifically, it looks at the ramifications of neutrals emanating from other parts of the thruster (other channels) on the operation of nested Hall thrusters. This included two separate investigations: one on an unshielded nested Hall thruster focusing on shifts in the acceleration region and one on a shielded nested thruster focusing on potential changes to lifetime based on variations in neutral density. After all the investigations are presented, Chapter 7 provides a discussion of the implications of our results including the underlying cause for the displacement of the acceleration region, and how to mitigate it. Finally, Chapter 8 summarizes all the findings and proposes recommendations for future work in the sub-field.

1.8 Conclusion

In this chapter, we first presented the problem statement that motivates this work. We then discussed the province for electric propulsion and the three main subclasses: electrothermal, electrostatic, and electromagnetic. The entirety of the work herein studies a particular type of electrostatic thruster, the Hall thruster. We gave a brief history of this device which uses a crossed electric and magnetic field to ionize and accelerate a propellant. The recent innovations and current challenges being faced for Hall thrusters were then presented the underlying cause for this displacement, and how to mitigate it. Next, we discussed the need for high power electric propulsion. Finally, we discussed the objectives of this work and the organization of the document herein.

CHAPTER 2

Theoretical Framework for the Impact of Neutral Density of Single-Channel Hall Thrusters

2.1 Introduction

In this chapter, we lay the theoretical framework for our experimental investigations into single-channel magnetically shielded Hall thrusters and how neutral density may impact them. We begin in Section 2.2 where we describe previous work done on neutral density impacts, particularly focusing on facility effects. In Section 2.3, we detail the performance model for Hall thrusters and how neutral density may effect various parameters. Finally, in Section 2.4, we discuss how neutrals may impact magnetic shielding before making concluding remarks.

2.2 Review of Previous Work

Studies have shown a cross-cutting susceptibility to variation in operation due to background pressure changes for Hall thrusters. [21, 22, 24, 26, 28, 63, 86] Changing facility pressure can be thought of as a proxy for changing neutral density. Therefore, these studies are directly related to our consideration of neutral density. Here, we summarize some previous works on

the impact of facility pressure on Hall thrusters.

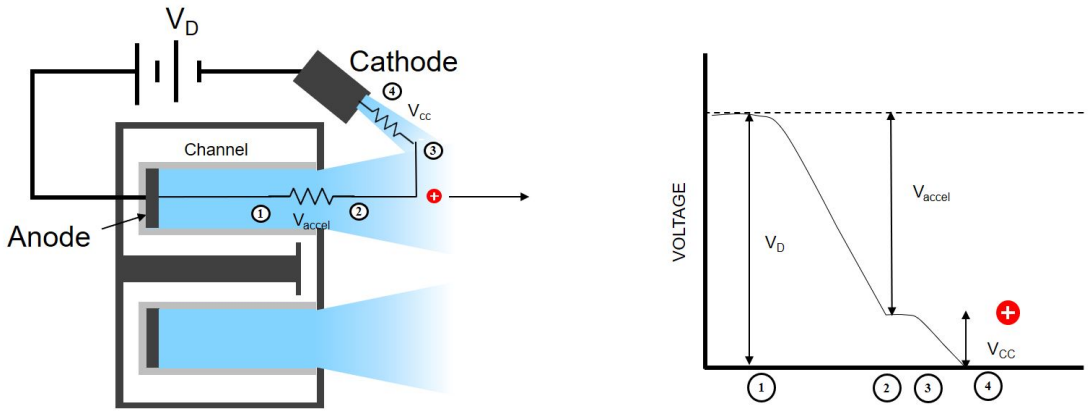

Figure 2.1: Graphical depiction of the cathode coupling voltage in a Hall thruster. This parameter is known to vary with facility pressure.

The major challenge with understanding these effects is that they appear to be a mixture of classical and non-classical physics. Recent studies seem to indicate that neutrals emanating from the background are somehow impacting the internal physics of the thruster. [87, 88] Indeed, there are four main parameters of thruster operation known to be impacted by pressure: the cathode coupling voltage, the thrust, the oscillatory nature, and the location of the acceleration region. The cathode coupling voltage (graphically depicted in Fig. 2.1), V_{cc}, is generally defined as the voltage between the cathode and the main discharge plume of the Hall thruster. This voltage is related to the ease with which electrons are extracted from the cathode and transported to the main thruster beam and anode. Many parameters impact this voltage [21, 64, 89–93]; in particular, increasing the facility pressure tends to decrease the coupling voltage between the cathode and the anode [21]. Additionally, experimental evidence shows that placing a cathode in the center-mounted configuration tends to decrease the thruster's susceptibility to facility effects in comparison with externally-mounted configurations [64].

Next, we look at the impact of facility pressure on thrust, which has been widely characterized. [22, 24, 86, 94, 95] Initial testing by Randolph et al. [22] indicated that the efficiency of the SPT-100 was invariant with facility pressure. However, the lowest pressure they operated the thruster at was 10 μTorr. Additionally, no information about how and where the pressure was measured was provided. Data from Sankovic et al. [96], contrasted this picture, showing varying specific impulse and efficiencies for the same thruster across the same pressure ranges as Randolph. Regardless, these studies motivated the need to better understand the facility impacts when predicting performance on orbit. Initial data from Hofer et al. [24] indicated a linear extrapolation to zero pressure may be appropriate. However, further studies on the SPT-100 by Diamant et al. showed that at pressures lower than 10 μTorr-Xe, the thrust versus facility pressure deviated from this linear trend dropping even more rapidly with pressure. [94] Similar results were seen by Hofer et al. on the H6 Hall thruster when operating with an externally mounted cathode. [20] Regardless, the trend was clear – thrust decreased with decreasing facility pressure. Despite this insight, it is challenging to know how this trend may change below pressure achievable by ground test faculties without on-orbit data. Additionally, changes in cathode position change the sensitivity of the thrusters, adding another variable into the equation. [28]

When it comes to the oscillatory nature of these thrusters, the trends are not as obvious. Randolph et al found that increasing the background pressure above a "critical level" (30-80 μTorr) could lead to very large discharge oscillations. [22] This change in oscillatory strength is graphically depicted in Fig. 2.2. Most studies use 30 μTorr as the upper limit of testing. Hargus et al similarly found that increasing the background pressure from 15 μTorr to 30 μTorr strengthened the oscillations on the BHT-600. [97] They also observed that the fundamental frequency shifted higher, and that the increase in oscillation strength led to a broadening of the ion energy distribution function. However, Raites et al found

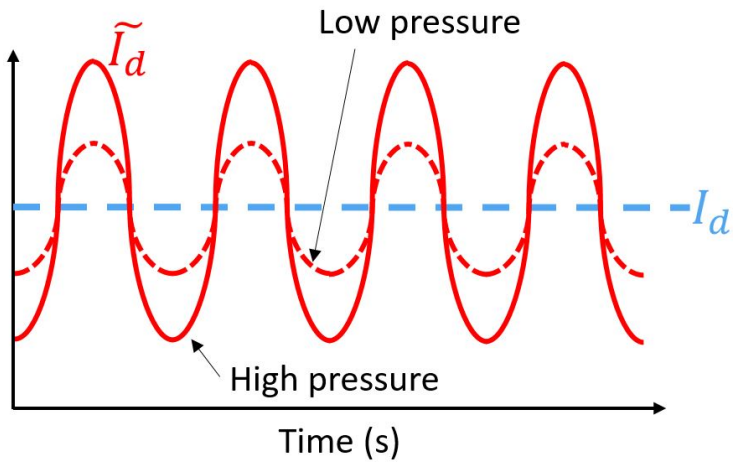

Figure 2.2: Graphical depiction of the change in oscillatory behavior with pressure in a Hall thruster.

that increasing pressure (from 3 μTorr to 50 μTorr) suppressed ionization instabilities in cylindrical Hall thrusters. [98] Additionally, Huang et al found that the HERMeS thruster oscillations were largely invariant with pressure. [21] Furthermore, initial on-orbit data indicates that these thrusters are "quieter" in-space than in ground-testing facilities. [22, 99]

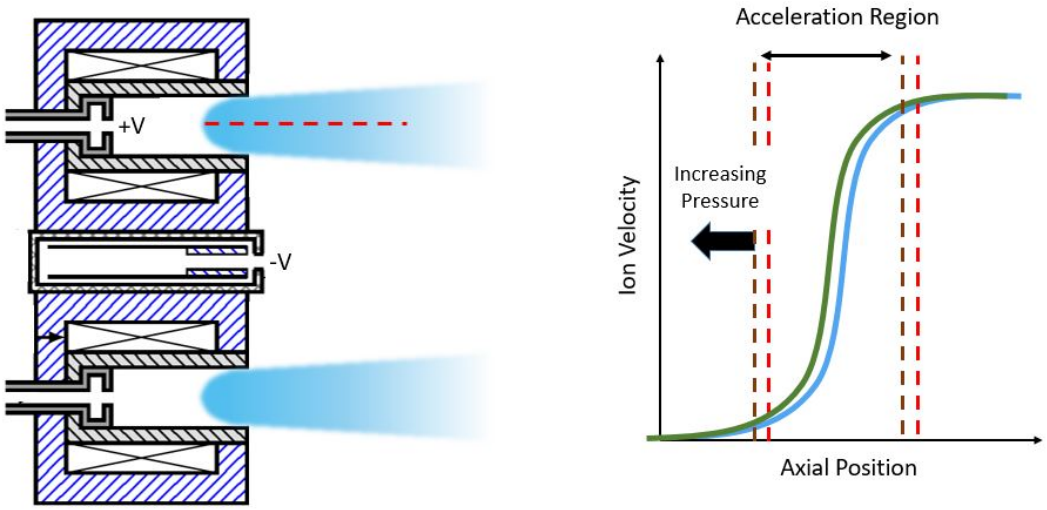

Figure 2.3: Acceleration region depiction along the centerline of a Hall thruster as well as it's typical response to facility pressure.

Finally, one of the most critical, but least understood facility effects, is the response of

the plasma's location in the discharge chamber to facility pressure. In Hall thrusters, the main ion beam is accelerated due to a potential drop between the anode and cathode. This drop occurs over a spatially small area (typically 1-10 mm), and its location is often coincident with the peak magnetic field. Qualitatively, we know that the electron mobility, and thus plasma potential, in the region is dominated by non-classical transport mechanisms. With increasing neutral density, we would expect the electron transport due to collisions to increase. Additionally, non-classical transport mechanisms can change with neutral density. For example, ion acoustic turbulence is known to exist in Hall thruster plumes. [100, 101] The growth rate of this turbulence depends on the local neutral density. Clearly, the processes which drive electron mobility can be impacted by neutral density. When the electron mobility profile changes, the electric field must respond. If the electron mobility increases, the electric field will decrease. Therefore, a change to the electric field structure in Hall thrusters is qualitatively expected with a change in the neutral density.

Indeed, previous studies have shown the location of the acceleration region to be sensitive to facility pressure, as depicted in Fig. 2.3. For example, Nakles et al. found that the acceleration region moves axially upstream [26] with increasing pressure, which is correlated with a decrease in divergence angle. A reduced divergence angle should trace to an improvement in thrust. Similar trends in divergence angle have been noted in a number of pressure studies. [21, 25, 28, 94] More recently, the movement of the acceleration zone has taken on additional importance for magnetically shielded Hall thrusters where shifts in the region are thought to impact anomalous pole erosion of the thruster and, possibly, the electron temperature of the grazing line. [102, 103] Although the fundamental reason why the acceleration responds to pressure is still not understood, there have been a number of correlational insights into this effect. The first is that it appears that the movement in the acceleration zone (and therefore thrust) with facility pressure asymptotes. That is, the improvement in thrust will reach a plateau. As concluded by Hargus et al., the second

insight is that it is the neutral density in the exit plane of thruster and not the actual facility background pressure that is the critical parameter driving the movement. [26,104,105]

Combined, previous works have experimentally described many of the impacts of neutral density on Hall thrusters. However, there remain fundamental open questions about these effects. Continuing to study this is critical to our understanding of Hall thruster physics.

2.3 Performance

In order to better understand how neutrals may impact the performance of Hall thrusters, we first detail the driving parameters of Hall thruster efficiency. Primarily, we are interested in the thrust for a given power and efficiency. Much of the Hall thruster work in the early 2000s was dedicated to understanding and improving Hall thruster performance. [55, 56, 106–110] We know that the thrust produced by a Hall thruster can be defined as

$$F_{th} = \dot{m}_i \bar{u}_{i,e} \tag{2.1}$$

where $\dot{m}_i$ is the mass flow rate of the ions and $\bar{u}_{i,e}$ is the mean exhaust velocity of the ions. Since not all ions have the same exit velocity, we must integrate over the entirety of the velocity distribution to analytically obtain the thrust. Additionally complicating matters is that not all ions exiting the thruster are singly charged. There tends to be an appreciable fraction of doubly- and triply- charged ions meaning that we must determine the mass flow and mean velocity of each species and then sum over each species present. To first order, the mass flow of the ions is proportional to the discharge power and neutral mass flow rate while the exhaust velocity is proportional to the square root of the discharge voltage. There are second order effects, such as background pressure, that are also important to these processes. In practice, because our understanding of the physics impacting these parameters

is incomplete, we rely on experiments, and directly measure the thrust of these devices.

Along with thrust, an effective EP device must also use the electric power delivered to it efficiently. Efficiency here is defined as the amount of input power directly converted to discharge power. We further define total and anode efficiency as

$$\eta_a = \frac{F_{th}^2}{2\dot{m}_a P_d} \tag{2.2}$$

$$\eta = \frac{F_{th}^2}{2\dot{m} P}, \tag{2.3}$$

where η_a is the anode efficiency, $\dot{m}_a$ is the anode mass flow rate, P_d is the discharge power, η is the total efficiency, $\dot{m}$ is the total mass flow rate ($\dot{m}$=$\dot{m}_a + \dot{m}_c$ (cathode mass flow rate)) and P is the total discharge power ($P = P_d + P_{mag}$ (power to the electromagnets)). The physical difference between anode and total efficiency relates to non-plasma generating (system) inefficiencies such as electromagnet power consumption and mass flow to the cathode. These efficiencies are only for the thruster itself and does not include the power processing unit. There are a few main loss mechanisms for Hall thrusters that drive the this efficiency: (1) mass utilization, (2) current utilization, (3) beam divergence, (4) voltage utilization, and (5) charge utilization. [2] Combined these yield the total anode efficiency: $\eta_a = \eta_d \eta_q \eta_b \eta_m \eta_v$, where η_q is the charge utilization efficiency which accounts for the presence of multiply charged ions. [111] Beam divergence (η_d) refers to losses from radial acceleration happening along the axial thrust vector. The mass utilization (η_m) derives from the fact that not all neutrals injected into the discharge chamber are ionized. Typical values for modern Hall thrusters are 85-90%. The current utilization (η_b) stems by virtue of the fact that the entirety of the discharge current is not compromised of ion current, and there is an appreciable fraction composed of electron current streaming back to the anode. This efficiency typically drives the overall of Hall thrusters and current designs have achieved 75-80%. Finally, the voltage utilization (η_v) results from not all discharge voltage being

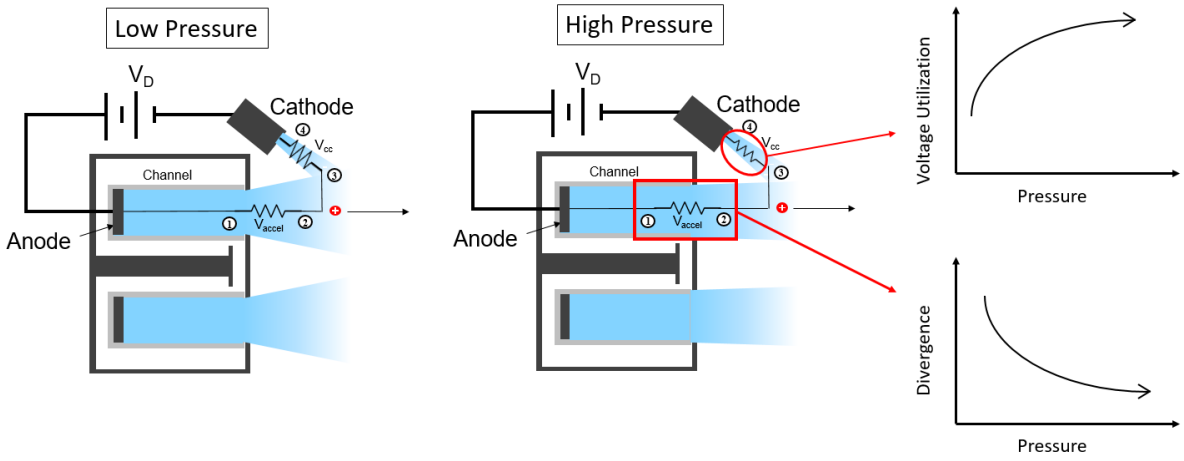

Figure 2.4: Graphical depiction of how the cathode coupling voltage and acceleration region change with pressure.

used for acceleration. Some voltage is required for coupling electrons from the cathode to the main thruster plume and making ions. The anode sheath conditions can also effect that voltage utilization. This value is typically between 85-95%. Throughout this work, we will discuss the parameters above with emphasis on the changes in these due to various neutral gas effects. The method to calculate relevant parameters will be discussed in later chapters.

There are two other loss mechanisms for the thruster: the cathode utilization (η_c) and the power utilization (η_p). These derive from the necessity to supply propellant to the cathode which can not be accelerated by the main thruster beam and any auxiliary power supplied to the thruster (power for electromagnets, cathode keeper, etc). To first order, these two only impact the total efficiency and not the anode efficiency. While both total efficiency and anode efficiency are important parameters, anode efficiency is more commonly used as these other factors change very little between thruster operating conditions. However, because the cathode is a source of neutrals for the thruster, we will discuss changes in cathode utilization.

Armed with the knowledge from Section 2.2, it can be seen that many of these parameters can be influenced by changing neutral density, graphically depicted in Fig. 2.4.

In particular, when the cathode coupling voltage changes, that will impact the voltage utilization ($\eta_v = V_{accel}/V_d$) since the accelerating voltage will change. Additionally, since the cathode coupling voltage can change the current flow in the thruster, the current utilization could change as well. When the location of the acceleration region changes, the beam divergence will be modified. Changes in oscillations are harder to quantify; however, they are thought to play a role in almost all of the efficiencies, in particular the mass and current utilization. The efficiency variations discussed so far are direct, first-order effects. Notwithstanding, there are thought to be more insidious nonlinear impacts all these parameters can have on thruster efficiency and performance with changing neutral density. Regardless, it is easy to see how changes in the neutral environment are tractable to change in thruster performance through measurable quantities such as the cathode coupling voltage and the acceleration region location.

2.4 Magnetic Shielding

The above description details the performance and its susceptibility to facility effects. However, equally important is the total lifetime of the thruster. In order to successfully complete space missions, Hall thrusters must have a sufficiency lifetime. As previously discussed, the main historical failure mechanism for Hall thrusters was discharge channel erosion. In traditional Hall thrusters, magnetic field lines are approximately radial. Due to the finite electron temperature near the channel exit, a component of the electric field is induced along these magnetic field lines towards the wall. Typically, this induced electric field is sufficiently large to accelerate some beams towards the walls. Additionally a large pre-sheath and sheath voltages are seen in the downstream portions of the discharge chamber of traditional Hall thrusters. This result leads to high ion velocities toward the walls. The walls of Hall thrusters are made of an isolator, typically boron nitride. If the ions hit the wall with sufficient force, they will sputter this wall material. Once sufficient

wall material has been sputtered, the magnetic circuit of the thruster will be exposed and isolation between the plasma and the thruster body can no longer be maintained. Ions with sufficient energy to sputter wall material exist at the same locations as peak electron temperature and peak electric field typically. This problem of erosion has been a long-standing issue in the field which remained "unsolved" until 2011.

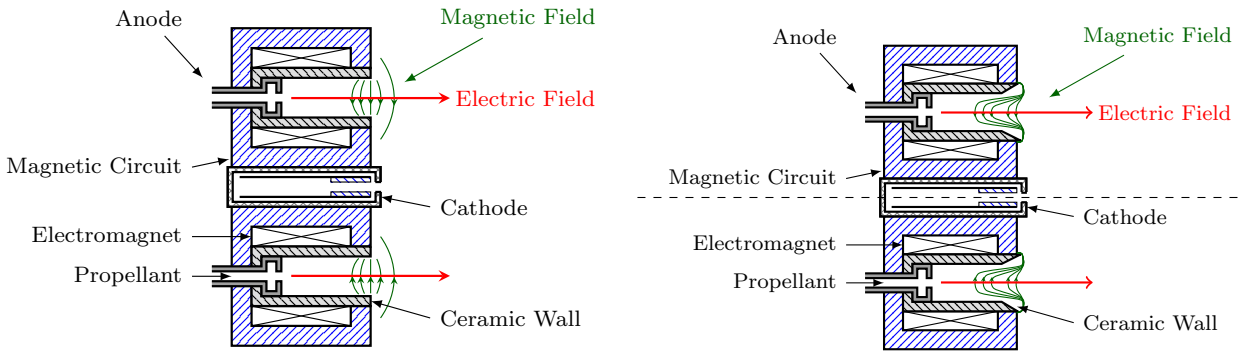

(a) a Unshielded Hall Thruster

(b) a Magnetically Shielded Thruster

Figure 2.5: A schematic of an unshielded Hall thruster versus a shielded Hall thruster.

Between 2007 and 2009, Aerojet Rocketdyne (AR) performed a 10,400 hour life test on a 4.5 kW thruster then called the BPT-4000. [61] After approximately 5,600 hours, the thruster entered a "zero-erosion" state, in which the profilometry measurements of the downstream discharge chamber isolator stopped showing any changes. NASA's JPL subsequently spent the next year analytically and numerically investigating this result until, in early 2011, they published their findings with AR. [18] The results revealed a new magnetic field configuration that shields the walls from most erosion. They called this new configuration "magnetic shielding." They then validated this technology from 2011 to 2014 by designing a thruster that should meet all the requirements for low-erosion and experimentally proving the thruster exhibited the expected behavior. [3, 19, 20, 111–113]

In principle, magnetic shielding works by exploiting two fundamental properties of Hall thrusters: (1) the isothermality of magnetic force lines and (2) the magnetic-force-line equipotentialization at low electron temperatures. Mathematically, the first principle can be expressed as

$$\nabla_{\parallel} T_e \approx 0, \tag{2.4}$$

where T_e is the electron temperature and $\nabla_{\parallel}$ is the gradient parallel to the magnetic field. The second principle stems from the Boltzmann relation:

$$\phi \approx \phi_0 + T_{e0} \log \frac{n_e}{n_{e0}}, \tag{2.5}$$

where ϕ is the plasma potential and n_e is the plasma density. The subscript 0 indicates an integration constant. Equation 2.5 yields a critical component to magnetic shielding in that the induced parallel electric field is,

$$E_{\parallel} = -T_e \nabla_{\parallel} \log n_e. \tag{2.6}$$

The first equation arises from the thermal transport of electrons along magnetic force lines resulting in rapid equilibrium and constant electron temperature along the line. The second equation implies that when electrons have a low temperature (i.e. $T_e < 10$ eV), then there are only small changes in potential along the field line. This relation arises from Ohm's Law in the limit of low electron collisionality. This results in an electric field perpendicular to the magnetic-force-lines which accelerates ions away from the walls as well as a reduction of ion flux to the walls. In principle, this eliminate the ability for high energy ions to hit the wall. However, there exists another parameter to be considered, although its effect is much smaller that those discussed above. Even ions that have low kinetic energy upon reaching the wall will still gain energy as they fall through the sheath potential. In order to consider this effect,

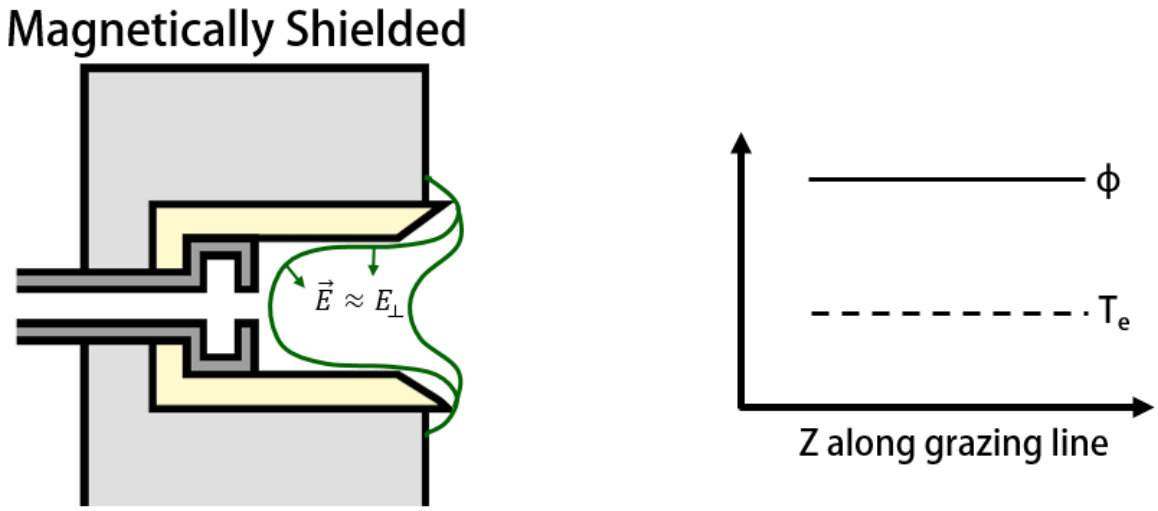

Figure 2.6: Schematic depicting the plasma potential and electron profile along the grazing line leading to no electric field parallel to the magnetic force line and low sheath potential.

we note that the sheath potential for boron nitride, the discharge chamber wall material, is dependent on the electron temperature and the secondary electron emission yield. Here, we follow the same process as Hofer et al. [20] The secondary electron emission yield is given by [114]

$$\gamma_e \approx \sigma_0 + (1 - \sigma_0)\frac{2T_e}{E_1}, \tag{2.7}$$

where σ_0 is the effective yield at zero energy and E_1 is the crossover energy. For boron nitride, the literature [114] gives values of 0.54 and 40 eV respectively. Assuming the sheath is not in the space charge limited regime (i.e. $T_e < 19.3$ eV), we can then calculate the resulting potential based on the one-dimensional equations from Hobbs and Wesson [115] as adapted by Goebel and Katz as [8]

$$\phi_s \approx -\frac{kT_e}{e} \ln\left[\sqrt{\frac{m_{Xe}}{8\pi m_e}}(1 - \gamma_e)\right]. \tag{2.8}$$

Since the wall sheath is proportional to the electron temperature, a very small sheath exists for low electron temperatures which again limits erosion. Altogether, should there be sufficiently cold electrons near the walls, the plasma potential along the wall remains high and the kinetic energy of ions towards the wall is significantly reduced. This results in reduction of the wall erosion. The erosion rate of the discharge channel is directly proportional to ion flux and the sputtering yield. This is also convolved with the incidence angle; however, for the purpose of this analysis we will assume all ions impact the wall perpendicularly. To define a metric for how much erosion occurs, we note that several works have suggested that ions as low as 30 eV can result in sputtering of wall materials. [15,19,116]

In order to achieve this high plasma potential near the walls, magnetic shielding shapes that magnetic field by extending the field lines into the anode region of the discharge chamber where electron temperatures are known to be low (<5 eV). Figure 2.5 shows what this new configuration of magnetic field looks like in order to achieve these requirements. The magnetic field line that reaches deep into anode region is referred to as the "grazing line." As depicted, this line typically "grazes" the wall and is the line that will determine the electron temperature and plasma potential along said wall. Changes to the internal magnetic circuit are made to induce the change in the shape of the magnetic field. The discharge chamber walls are chamfered on magnetically shielded thrusters in order to more easily extend necessary field lines deep into the channel. Validation studies performed on the H6MS thruster showed that this new magnetic field configuration yielded a 2-3 order of magnitude reduction of wall erosion. [20]

There was initially some concern that this new magnetic field configuration would significantly alter the performance of Hall thrusters. NASA JPL was able to study these impacts because the initial validation thruster used, the H6MS, had an unshielded counterpart with similar geometry and design elements. After extensive studies, JPL found that the

H6MS thrust was reduced 4.2% (from 401 mN to 384.2 mN at 6 kW), specific impulse was increased 2.6% (from 1950 s to 2000 s at 6 kW), and total efficiency was reduced 1.7% (from 0.635 to 0.624 at 6 kW) relative to its unshielded counterpart. [111] Thus, the team validated that the performance of these thrusters was not significantly impacted. Since these initial validation studies, magnetic shielding has been extended to high-specific impulse [112, 113], high power [117], low power [118–120], conducting wall [121, 122] and laboratory test-bed thrusters [123]. Finally, magnetic shielding was incorporated into the development of the 12.5 kW Hall Effect Rocket with Magnetic Shielding (HERMeS) thruster, which was a joint development project between NASA Glenn and NASA JPL. [124] Originally slated for the now-canceled ARRM mission [125, 126] this thruster has the potential to enable many missions, including the Deep Space Gateway. [65, 127]

As it enables lifetimes of several 10s of khs, which are needed for deep space missions, magnetic shielding was a large step forward for the application of Hall thrusters. However, similar to traditional Hall thrusters, these devices also are susceptible to facility effects. Given the possible link between stability, acceleration region movement, and facility pressure, there is a possibility that the mechanisms for shielding may also be impacted by facility effects. Due to the prohibitive cost of lifetime testing and lack of first-principles based numerical models, it is challenging to experimentally verify how these changes may be impacting the overall performance and lifetime. The lifetime of these thrusters is intrinsically linked to the electron temperature of the "grazing line." As previously discussed, the grazing line is the magnetic field line that reaches deep into the thruster to bring cold electrons up the walls. Inherently, this line does not intersect with the discharge chamber walls. Figure 2.7 shows a depiction of the grazing line. The depth of the grazing line is likely linked to the location of the acceleration region and overall performance of the thruster. In fact, the small reduction in thrust between an unshielded and a shielded thruster is thought to be a result of the acceleration region being pushed outward. [20]

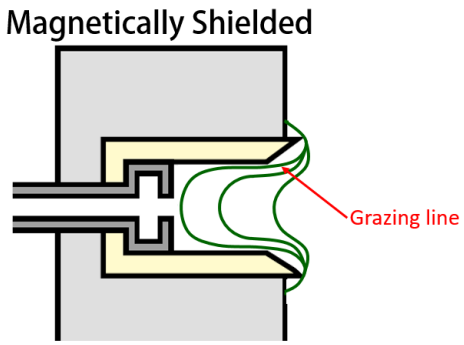

Figure 2.7: Schematic of the magnetic field for a magnetically shielded Hall thruster. Not to scale

However, the erosion rate of the discharge chamber walls is also dependent on the depth of this line as the "deeper" it goes, the colder it will be, thus making magnetic field lines more equipotential and reducing sheath drops – both of which can mitigate erosion. Therefore, it would appear as though we would only want to design the thruster with a sufficiently deep grazing line to achieve necessary lifetimes for a given mission. In turn, this would minimize outward shifting of the acceleration region and preserve thrust. Nonetheless, subtle shifts in the location of the plasma, such as those induced by neutral density changes, could impact the temperature and the reference potential of this grazing line; in turn, this could have ramifications on the lifetime. That is to say that if the acceleration region shifts outwards, the reference potential that defines the wall potential will approach the anode potential and vice versa. These prospective changes are graphically depicted in Fig. 2.8. This is because, when the electron temperature of the grazing line increases, the potential drop across that line also increases. We also see small but important changes to the sheath potential. Combined these effects could raise the impact energy of ions to that above the sputtering threshold. The physical picture would suggest that on-orbit erosion would be lower than ground measurements, because the neutral density on-orbit is significantly lower. We note that this picture depends on the centerline gradient of the electron temperature profile in the near-anode region. Numerical simulations on the H6MS by Mikellides et al show that gradient is very small in this region, and in fact there is a very high gradient over a small

region closer to the exit plane. [3] In this realistic scenario, even if the entire profile shifted upstream, there would only be a very small impact on the temperature of the grazing line. Regardless, an experimental investigation to quantify the change in ion impact velocity with varying neutral density is critical.

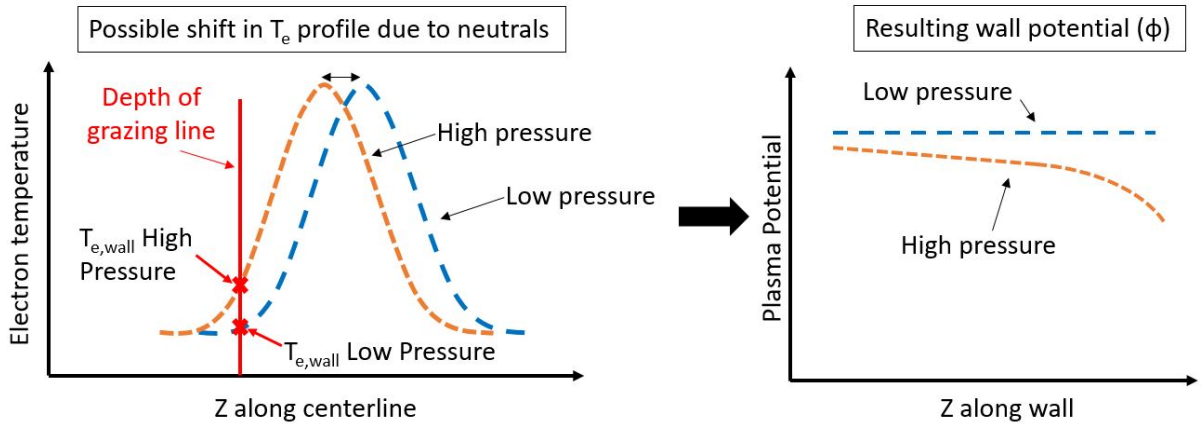

Figure 2.8: Graphical depiction of changes to electron temperature and potential profiles with changing neutral density.

2.5 Conclusions

In this chapter, we outlined the theoretical framework for which our experimental investigations into neutral density impacts on single-channel magnetically shielded Hall thrusters are based. We began in Section 2.2 with a review of previous works. Then, in Section 2.3 we detailed the performance model for Hall thrusters and how neutrals may impact the various driving efficiencies. Finally, in Section 2.4 we presented the theory behind magnetic shielding as well as the potential for neutral density changes to influence the lifetime of the thrusters based on this theory. This frameworks details the importance of neutral density on Hall thruster operation and guides our experimental investigations presented in Chapters 5 through 7. Additionally, it provides the foundation for which our theoretical framework for neutral impacts on nested Hall thrusters (Chapter 3) builds from.

CHAPTER 3

Theoretical Framework for the Impact of Neutral Density of Nested-Channel Hall Thrusters

3.1 Introduction

We start this chapter detailing an approach to scaling Hall thrusters to high power: nested Hall thrusters. While all the neutral density effects discussed in Chapter 2 still apply to nested Hall thrusters, there are some additional, unique impacts due to the presence of another channel. This chapter discusses (in Sections 3.4 and 3.5) ways in which neutrals originating from other channels in the thruster can impact the performance and lifetime before concluding the chapter.

3.2 Nested Hall Thrusters

Since Hall thruster research began in the 1960s, researchers have been suggesting ways to scale the devices to higher power levels. [128] Nested Hall thrusters (NHTs) provide one means of achieving this goal. NHTs have multiple discharge annuli concentrically nested together. Figure 3.1 shows the schematic of a nested Hall thruster with a traditional single-channel Hall thruster for reference. The nesting of multiple channels allows high efficiency

and thrust-to-power ratios at very high powers (>50 kW) with a lower specific mass and expanded throttling range as compared to their single channel counterparts. [129] At the same time, they leverage the nearly five decades of flight heritage and maturity of single channel Hall thrusters. Nested Hall thrusters generally run off a single, centrally-mounted cathode. Each channel of the nested thruster has dedicated electromagnets to produce the magnetic field. One of the unique features of nested Hall thrusters is the use of shared

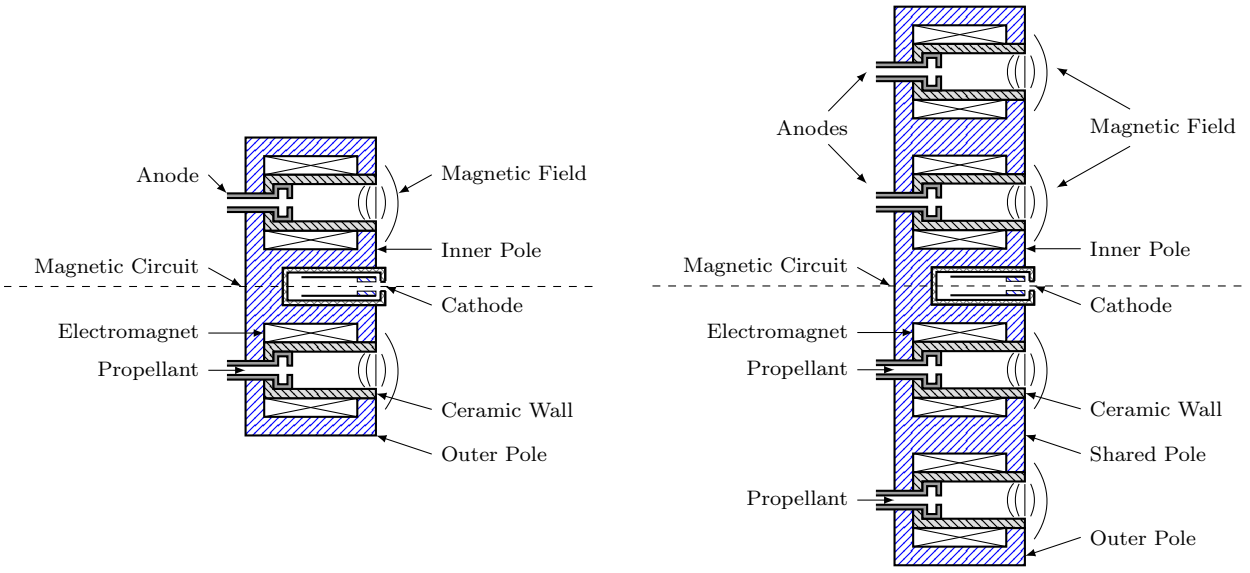

(a) Traditional Hall thruster

(b) Nested Hall thruster

Figure 3.1: Cross sectional view comparing Hall thruster and nested Hall thruster design. The dashed line is the cylindrical axis of symmetry.

magnetic cores, which reduces the total mass of the thruster. Due to these shared poles, the direction of the magnetic field switches from channel to channel. This means that, for instance, if the inner channel magnetic field points radially inward, the outer channel magnetic field must point radially outward. The anodes for each channel generally have the same design and are scaled appropriately. The design principles described above are rules of thumb and are not inherently implicit to their design.

Overall, nested Hall thrusters allow for scaling to high power without increasing the

size of the thruster according to traditional scaling laws. For the same amount of total power, the total enclosed thruster area is typically halved as compared to a traditional Hall thruster. [37] Additionally, because nested Hall thrusters have a variable discharge area, they enable a wider operational envelope. For instance, the X2, a two-channel thruster, confirmed operation between 1000 and 3000 seconds of I_{sp} at 6 kW by switching the firing configuration. [130] This allows the operator to choose their operating mode: high specific impulse or high thrust. Alternatively, nested Hall thrusters enable a high efficiency, high specific impulse mode over a much wider range of operating powers. This is particularly critical for deep space missions where available power changes depending on the spacecraft's distance to the sun. Additionally, some initial work on the X2 indicated that dual channel operation may lead to enhanced performance compared to the sum of single channel operation on nested Hall thrusters. [6, 131]

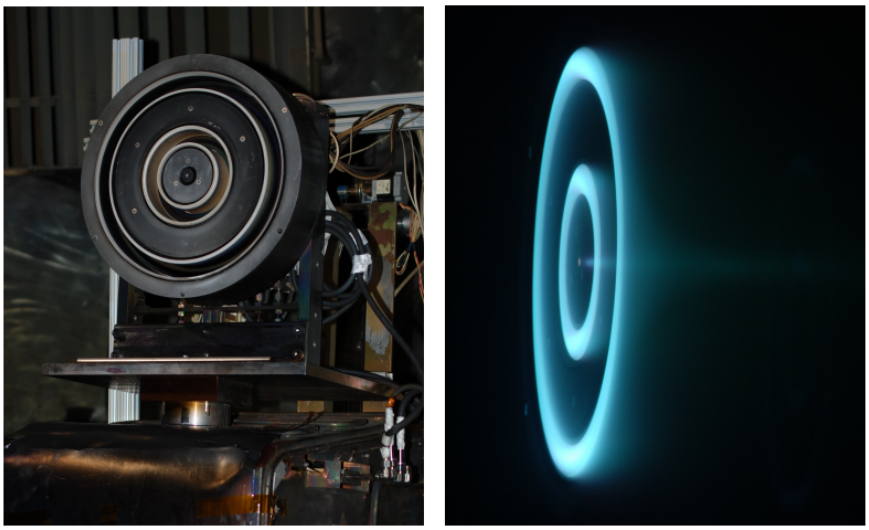

Figure 3.2: (left) A picture of the first nested Hall thruster developed at the University of Michigan, the X2, installed in a vacuum chamber and (right) a picture of the X2 firing in dual-channel mode.

The concept of NHTs has been explored since as early as 1986. [132] However, the modern era of NHTs began in 2004 when both the Busek Company and NASA Glenn Research

Center began investigating the concept. [37, 133] In 2011, the Busek Company showed notional designs and development progress for two nested Hall thrusters. [134] Along a similar time frame, the University of Michigan, in conjunction with the Air Force Office of Scientific Research, NASA Glenn Research Center, and NASA Jet Propulsion Laboratory, began their own development efforts for nested Hall thrusters. The first developed in this series was the X2, a 10-kW class two-channel nested Hall thruster. [1, 130, 135–137] This thruster, capable of discharge powers up to 10 kW, was developed as a proof-of-concept for nesting multiple channels together and was developed as a collaboration between the University of Michigan and the Air Force Office of Scientific Research. [130] Pictures of the thruster are seen in Figure 3.2. One feature of nested Hall thrusters is their ability to run in multiple configurations, allowing for a wide power range. That is to say, a two channel thruster can run just the inner channel, just the outer channel or both channels combined. The X2 demonstrated the ability to run in all possible channel configurations, validating the technology. It also demonstrated the ability to run off a single centrally-mounted cathode.

Upon validation of the nested configuration, work began on the development of a higher power nested Hall thruster. This thruster, the X3, was a joint development project between the University of Michigan, the Air Force Research Laboratory, JPL, and NASA's Glenn Research Center. [138–145] The X3 is a three-channel NHT designed for power levels up to 200 kW while only being approximately 80 cm in diameter. The scaling of each channel is more similar to the H6 family than the X2. Because it has three channels, there are seven possible firing configurations of the thruster. This thruster incorporated the magnetic lens topography [146] on NHTs and continued the validation of NHTs for high-power electric propulsion. Testing of this thruster is ongoing with the X3 being selected as part of NASA's NextSTEP program, which is NASA's program for the development of technology it deems critical for future crewed missions to Mars. [71, 147] Three different propulsion systems were selected for the program, with the X3 being part of the XR-100 system led by Aerojet

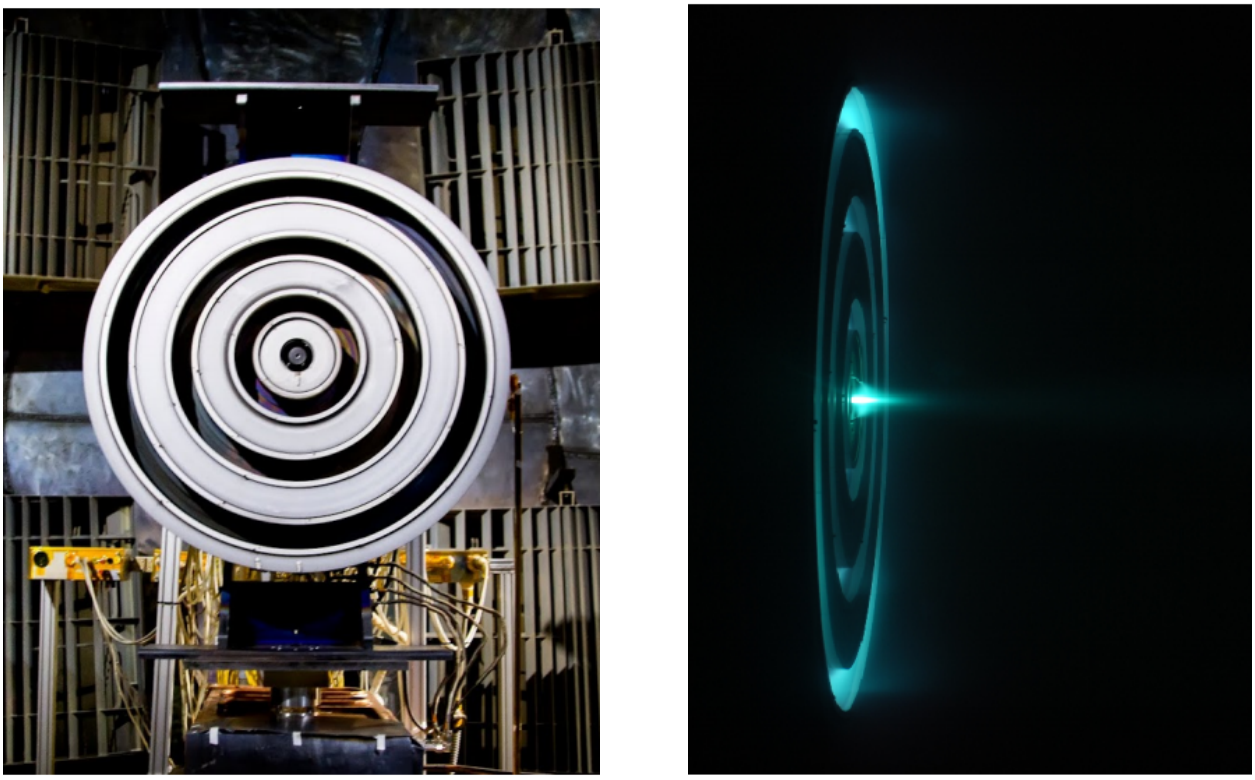

(a) (b)

Figure 3.3: A picture of the X3 Hall thruster installed in the facility (a) and firing in three-channel operation (b).

Rocketdyne in partnership with University of Michigan, NASA Jet Propulsion Laboratory, and NASA Glenn Research Center. [71, 148] A picture of the X3 installed in a vacuum chamber and a picture of the thruster firing at 30-kW in three channel configuration is seen in Figure 3.3. [143] During the NextSTEP program, the X3 Hall thruster demonstrated the highest power (102 kW), highest discharge current (247 A), and highest thrust (5.4 N) ever produced by a Hall thruster. It also achieved thermal steady state at 72 kW. [145, 149] These results helped demonstrate and validate the technology is capable of the type of missions discussed earlier.

3.3 Efficiency Model for Nested Hall Thrusters

We can extend the performance model presented in Section 2.3 for nested Hall thrusters. As a starting point, we make a "first-attempt" assumption that nested operation is simply the addition of each channel operating alone:

$$F_{multi} = \sum_{i=1}^{N} F_i, \tag{3.1}$$

where F_i is the thrust for an individual channel and N is the number of channels. Here, we will focus on two-channel thrusters. We can re-write equation 3.1 as

$$F_{dual} = F_{inner} + F_{outer}. \tag{3.2}$$

Extending this summation to other relevant parameters such as efficiency and specific impulse (I_{sp}), we expect

$$\eta_{dual} = \frac{F_{dual}^2}{2(\dot{m}_{inner} + \dot{m}_{outer})(P_{inner} + P_{outer})} \tag{3.3}$$

$$I_{sp,dual} = \frac{F_{dual}}{g_0\,(\dot{m}_{inner} + \dot{m}_{outer})}. \tag{3.4}$$

By combining equation 3.2 with Eqn. 3.4, we get

$$I_{sp,dual} = \frac{F_{inner} + F_{outer}}{g_0\,(\dot{m}_{inner} + \dot{m}_{outer})} \tag{3.5}$$

$$I_{sp,dual} = \frac{F_{inner}}{g_0\,(\dot{m}_{inner} + \dot{m}_{outer})} + \frac{F_{outer}}{g_0\,(\dot{m}_{inner} + \dot{m}_{outer})} \tag{3.6}$$

$$\tag{3.7}$$

Knowing that $I_{sp,inner} = F_{inner}/(g_0 \dot{m}_{inner})$, we further simplify the first term of this equation to

$$\frac{F_{inner}}{g_0 \left(\dot{m}_{inner} + \dot{m}_{outer}\right)} = \frac{F_{inner}}{g_0 \left(\dot{m}_{inner} + \dot{m}_{outer}\right)} \left(\frac{\dot{m}_{inner}}{\dot{m}_{inner}}\right) \tag{3.8}$$

$$\frac{F_{inner}}{g_0 \left(\dot{m}_{inner} + \dot{m}_{outer}\right)} = I_{sp,inner} \left(\frac{\dot{m}_{inner}}{\dot{m}_{inner} + \dot{m}_{outer}}\right) \tag{3.9}$$

Following the same process for the outer channel, we find that the specific impulse in dual channel mode is

$$I_{sp,dual} = \chi_{inner} I_{sp,inner} + \chi_{outer} I_{sp,outer} \tag{3.10}$$

where,

$$\chi_{inner} = \frac{\dot{m}_{inner}}{\dot{m}_{inner} + \dot{m}_{outer}} \qquad \chi_{outer} = \frac{\dot{m}_{outer}}{\dot{m}_{inner} + \dot{m}_{outer}} \tag{3.11}$$

Thus, the specific impulse is simply the mass weighted combination of single-channel values. Based on this, we should be able to predict dual channel performance simply based on single channel performance of each individual channel. However, the above descriptions do not account for neutral impacts on the performance. Thus, in Section 3.4, we modify the above equations to account for changes due to the higher neutral density. In particular, we focus on modifying Eqn. 3.2, which can then be used to calculate the other performance parameters.

3.4 Neutral Impacts on Performance

Beyond the neutral impact discussed in Chapter 2, nested Hall thrusters have the potential to source neutrals from any adjacent operating channels. Results have suggested that dual channel operation is not simply the addition of single channel operation, even when background pressure is accounted for. [1] Here, we present the theory leading to this improved performance. [6] We postulate that the local pressure profile of a NHT is the dominant

mechanism by which anomalous thrust is produced. The increased neutral density near the thruster will lead to two mechanisms of improved performance: (1) neutral ingestion resulting in a higher beam current and (2) acceleration region movement resulting in a lower divergence angle. The assumptions of this model are that all neutrals impacting the thruster are emanating from the adjacent channel, there are no changes in thruster parameters due to oscillations, and that changes in the acceleration region will only lead to changes in divergence. Neutral ingestion is a well-documented phenomenon in Hall thrusters. [26, 27] Randolph [22, 150] showed that the ingested mass flow rate due to background neutrals for Hall thrusters should be

$$\dot{m}_{ing} = \Gamma m_{Xe} A_{exit}, \tag{3.12}$$

where m_{Xe} is the mass of the xenon atom, A_{exit} is the channel (of interest) exit area, and Γ is the flux of background particles found to be [150]

$$\Gamma = \frac{1}{4} n_b \sqrt{8kT_b/\pi m_{Xe}}. \tag{3.13}$$

Here, n_b is the number density of background neutrals, k is Boltzmanns constant, and T_b is the temperature of the background neutrals. Assuming that this model can be extended to neutral ingestion from a proximal source, the thrust addition due to neutral ingestion should be

$$F_{ingestion} = \dot{m}_{ing} u_e \alpha_i \tag{3.14}$$

where u_e is the exit velocity of the ionized ingested particles and α_i is the ionization fraction of the ingested particles. Additionally, we already know that with increasing background pressure, experimental measurements have shown that the acceleration region of a Hall thruster will shift upstream. [97, 151] If a shift in the acceleration region is measured at

constant background pressure in a nested configuration, then the change in local pressure is likely affecting the divergence of the ion beam. The thrust divergence efficiency for a single channel is given by [8]

$$\eta_t = \frac{\int_{r_1}^{r_2} 2\pi r j(r) \cos(\theta) dr}{I_b}, \tag{3.15}$$

where $j(r)$ is the current density distribution, r_1 and r_2 are the radial locations of the 90% bounds for current density, θ is the half-angle divergence, and I_b is the total beam current calculated as

$$I_b = \int_0^{2\pi} \int_{r_1}^{r_2} j(r,z) r dr d\phi \tag{3.16}$$

where ϕ is the azimuthal angle around the thruster about thruster centerline. It is easy to see that if there were no divergence (i.e. θ is zero degrees), the Eqn. 3.15 reduces to $I_b/I_b = 1$. Thus, in the event that there is no divergence, there is no thrust loss due to divergence and the acceleration is purely axial. Given a finite divergence, we can calculate the theoretical thrust without divergence losses as

$$F_{zero,div} = \frac{F_{actual}}{\eta_t} \tag{3.17}$$

where F_{actual} is the measured thrust. $F_{zero,div}$ is the maximum possible thrust for a given condition if the acceleration is axial and all other efficiencies are held constant. Therefore, the "thrust lost to divergence" for a given condition is the difference between the maximum possible and the actual value:

$$F_{lost} = F_{zero,div} - F_{actual} \tag{3.18}$$

$$F_{lost} = \left[\frac{F_{actual}}{\eta_t}\right] - F_{actual} = F_{actual}\left[\frac{1}{\eta_t} - 1\right] \tag{3.19}$$

Alternatively, we can re-write Eqn 3.19 as,

$$F_{lost} = F_{zero,div}\,(1 - \eta_t) \tag{3.20}$$

To compute the total thrust divergence efficiency of a two-channel thruster, the efficiencies are multiplied together [8]

$$\eta_t^{total} = \eta_t^{inner}\eta_t^{outer}. \tag{3.21}$$

When nested Hall thrusters are operated in multi-channel operation, the thrust lost to divergence decreases as compared to single channel operation. This corresponds to a measured increase in thrust. We can calculate this increase as the difference in thrust losses between single-channel and dual channel mode. The increased thrust (from both channels) in dual channel mode as compared to the summation of single channels modes due to divergence, F_{div} is,

$$F_{div} = F_{lost,single-channel} - F_{lost,dual-channel} \tag{3.22}$$

$$F_{div} = (1 - \eta_1)F_1 - (1 - \eta_2)F_2 \tag{3.23}$$

where η_2 is the divergence efficiency in dual channel, η_1 is the divergence efficiency in single channel mode as defined by Eqn. 3.21, F_2 is the calculated thrust before divergence losses in dual channel mode, and F_1 is the summation of the calculated thrusts before divergence losses for the inner and outer channels. Combining all this, we can update Eqn. 3.2 for the expected thrust of the device in dual-channel operation as

$$F_{dual} = F_{inner} + F_{outer} + F_{ingestion} + F_{div}, \tag{3.24}$$

where F_{inner} is the measured thrust for the inner channel and F_{outer} is the measured thrust for the outer channel. While much of the above analysis is done for a two-channel thruster, it can be extended to NHT with an arbitrary number of channels easily (e.g.$F_{multi} = \sum_{i=1}^{N} F_i + F_{ingestion} + F_{div}$). Overall, we see that neutral density emanating from other channels theoretically can improve the performance of nested Hall thrusters by providing additional neutrals to be ingested as well as reducing the divergence angle. In our experimental investigations, we aim to use this model to see if we can explain differences in single and multi channel mode operation.

3.5 Lifetime

While there is no known fundamental difference between single-channel and nested Hall thruster neutral impacts on lifetime, it is critical to talk qualitatively about changes and expectations. Here, we focus specifically on magnetically shielded thrusters. For single channel thrusters, the emphasis was on potential changes that could be induced from neutrals emanating from the background. These changes are challenging to predict and could impact lifetime on orbit. However, for nested Hall thrusters, the complexity of the problem increases. For example, consider the inner channel of a two-channel thruster. Our theory for performance changes suggests that when the outer channel flow is turned on, the acceleration region of the inner channel will move inward. When this happens, the temperature of the grazing line could also change leading to higher erosion. Thus, the lifetime of each channel (or the overall thruster) could depend on the amount of time in each firing configuration. Quantitatively, if the pressure in the chamber were to rise 10 μTorr, we would expect an increase in neutral density of about 3×10^{17} m^{-3}. However, the neutral density due to channel neutrals is typically above 10^{18} m^{-3}. So, for nested Hall thrusters, there is actually a much larger increase in neutral density due to the presence of adjacent channels as compared to simply changing the facility pressure. Thus, there is a potentially larger change

in the grazing line electron temperature. Assessing potential changes in lifetime on the firing configuration for magnetically shielded nested Hall thrusters is thereby an important aspect of this work.

3.6 Conclusions

In this chapter, we began by discussing nested Hall thrusters, a potential path for expanding the power levels achievable by Hall thrusters. We then focused on extending the theoretical framework presented in Chapter 2 to encompass the unique situation of neutrals sources from adjacent channels in NHTs. Combined, these two Chapters inform the experimental investigations we pursue in the remainder of this work. Moving forward, we will first discuss the experimental equipment used for these studies and then show the results. Finally, we will discuss these results with particular emphasis on comparing them to the theoretical framework laid out here.

CHAPTER 4

Experimental Equipment

4.1 Introduction

In this chapter, we describe the experimental equipment used throughout these investigations. To begin, we describe the thrusters used: the H9, the X2, and the N30. Since the H9 and N30 were developed as part of these works, we describe design principles and goals. Finally, we discuss the cathodes used for each of these thrusters. After discussing the thrusters, we describe the facility used for this investigation - the Large Vacuum Test Facility at the University of Michigan. The Owen's Chamber at NASA's Jet Propulsion Laboratory was used for the acceptance testing of the H9 Hall thruster. This facility will be discussed in Appendix A Finally, we describe the diagnostics used including the thrust stand, plasma probes, and laser-based diagnostics.

4.2 Thrusters

The main goal of this work is to assess the neutral impacts on performance and lifetime of high power magnetically shielded Hall thrusters. To enable this research, we used three Hall thrusters. The first, the H9, is a single channel magnetically shielded Hall thruster, which is described in section 4.2.1. This thruster allowed us to study the impact of background neutrals on state-of-the-art thrusters. We also studied two nested Hall thrusters: the X2 and the N30. The X2, described in section 4.2.2, is a two-channel unshielded thruster. Studies on

this thruster focused on the changes in performance due to neutrals from adjacent channels. Finally, in section 4.2.3, we detail the N30, a two-channel magnetically shielded Hall thruster, on which the lifetime studies were performed.

4.2.1 The H9

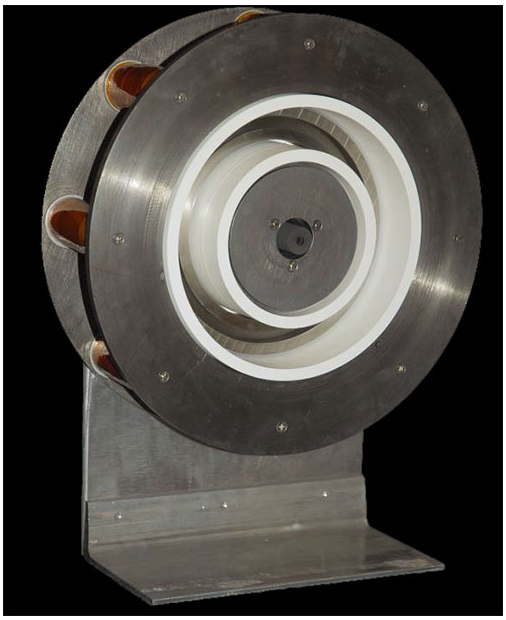

Figure 4.1: A photo of the H6 after manufacturing. Taken from Reid. [5]

The H9 Hall thruster is a 9-kW magnetically shielded Hall thruster that was developed by NASA JPL in collaboration with the University of Michigan and AFRL. [123] The development, initial validation, and testing were described by Hofer et al. [123] and Cusson et al. [152] respectively. The acceptance testing resutls are also shown in Appendix A. Its design leverages its predecessor, the H6. The H6 is a 6-kW Hall thruster designed in 2006 with the purpose of creating a uniform testbed for Hall thruster physics and development research in the United States. [153] This thruster was also a joint development project between the AFRL, JPL, and the University of Michigan, with three thrusters fabricated in total. Many features that were included in the H6 design were carried through to other thrusters in this series, including a plasma lens magnetic field topography, [2, 56, 146] a centrally-mounted LaB_6 cathode, [46, 64, 154–156] and a high uniformity gas distributor and anode. [157] All of these features combined culminated in the demonstration of new milestones in performance including 401 mN of thrust, 1950s of total specific impulse and 64% total efficiency at the nominal 6-kW condition. When the discharge voltage was raise to 800 V, total efficiencies of 70% were achievable. The development of this thruster led to numerous journal and conference proceedings as well as

doctoral dissertations. As a laboratory testbed, it also has facilitated new understanding of thruster operation at high specific impulse and helped guide the development of magnetic shielding.

In 2011, JPL retrofitted their H6 to incorporate magnetic shielding, designated the H6MS, discussed earlier. Following the success of the H6MS, as well as numerous research studies, a collaborative effort to design a new testbed for Hall thruster research in the United States began in 2016. [123] This new thruster, the H9, shared many critical components with the H6MS, including the discharge chamber geometry and anode design. Thus, research performed on the thruster could still be compared to the H6 variants. However, because this thruster was designed from conception to be magnetically shielded, it was not limited by the same constraints that the retrofit of the H6 was. The thruster features a magnetic lens topography with magnetic shielding to increase thruster lifetime. The electron source is provided by a centrally mounted lanthanum hexaboride hollow cathode that is identical in design to those built for the H6 Hall thruster [155]. The thruster has a nominal throttling curve from 4.5 to 9 kW and voltage range from 300 to 800 V, but can operate outside of this range. Each thruster features replaceable boron nitride rings for the discharge chamber, graphite pole covers, and a stand that also acts as a radiator. While the H9 thruster body is capable of operating in multiple electrical configurations, the default we employed for our testing was the cathode-tied configuration, i.e. the cathode common is electrically connected to the thruster body [125, 158, 159]. At the comparable 300 V, 6 kW condition, this thruster produced 384 mN of thrust and 1974 seconds of total specific impulse all at 61.6% total efficiency. [152] These numbers are within 1.5% of its counterpart, the H6MS, all while achieving a higher degree of shielding.

For the studies performed in this work, the H9 was operated at 300 V and 15 A, for a total discharge power of 4.5 kW. The applied magnetic field strength was kept constant. The

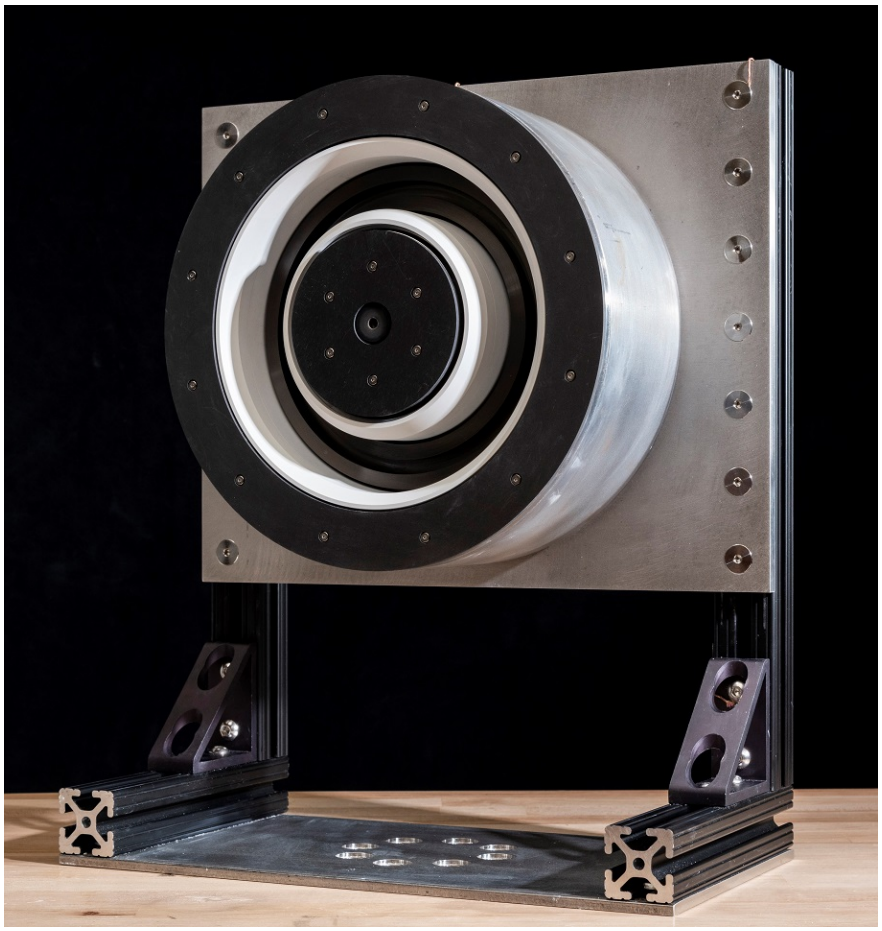

Figure 4.2: A photo of the H9 Hall thruster.

cathode flow fraction was varied between 5 and 15%, depending on the test point. The cathode flow fraction is the percent of the anode flow that is diverted to the cathode, i.e. $\dot{m}_c = CFF \cdot \dot{m}_a$. It is typical for Hall thrusters to run with a CFF ranging from 6-9% with 7% being the most common.

4.2.2 The X2

As mentioned in Chapter 3, the X2 is a 10-kW, two-channel nested Hall thruster. Initially developed as a proof-of-concept for nesting channels concentrically, the thruster features two discharge channels of similar anode design and magnetic field topographies. The thruster uses a magnetic lens topography, similar to other state-of-the-art Hall thrusters. Due to shared magnetic components, the magnetic field on the inner channel points radially inward while the outer channel magnetic field points radially outward. The channels share a single centrally mounted LaB_6 hollow cathode. A picture of the thruster firing and installed in the testing facility can be seen in Fig. 4.3.

For these studies, the X2 was operated at 150 V and 4.5 kW of total discharge power. The discharge power of the inner and outer channels was 1.25 kW and 3.25 kW, respectively. The mass flow was 21.8 mg/s for the outer channel and 8.7 mg/s for the inner channel. The cathode flow fraction was kept at a constant 10% of the anode flow rate for all activated channels. This implies that the cathode flow rate was the same for all cases in which the same channels had plasma discharges. Throughout the experiments, the thruster body was electrically connected to facility ground. The applied magnetic field strength for each operating condition was identical.

4.2.3 The N30

Throughout the testing of X2 and X3 testing, certain limitations of these thruster emerged. First and foremost, since their development took place before the advancement of mag-

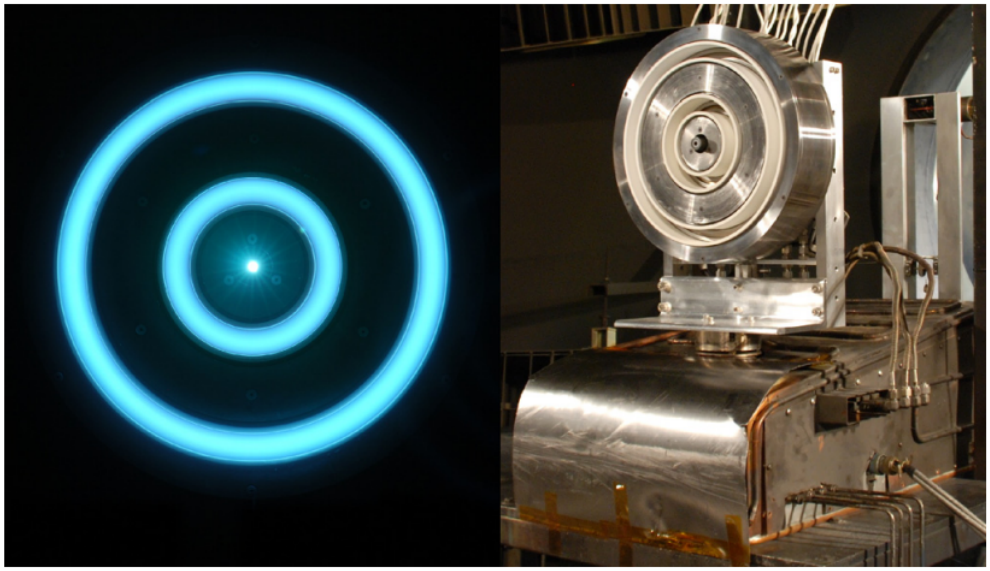

Figure 4.3: A picture of the X2 Hall thruster firing in dual channel mode and installed in the LVTF. Taken from Cusson et al. [6].

netic shielding, neither have incorporated this lifetime extending technology. Since most high-power missions under consideration are in deep space, the demonstration of this magnetic field configuration on NHTs is critical. The NextSTEP program, for example, ultimately has the goal of demonstrating >10000 hours of operation. While an official lifetime has not been stated, simulations indicate the X3 boron nitride will have eroded 10 mm by 10000 hours. [59, 160] Moreover, the HERMeS thruster was developed with a 50 kh requirement, which is more in line with many deep space missions. [125] Additionally, throughout testing, we uncovered many ways in which the channels interact with each other such as each channels neutrals impacting other channels ingestion and acceleration region location, magnetic field interactions, and oscillation behavior changes depending on firing configuration. [6, 131, 145, 161, 162] However, since no channel on either thruster has a single channel counterpart, it is difficult to deconvolve the exact implications of nesting channels together. Understanding these implications is critical to NHT development towards flight. As such, in 2017, the University of Michigan, in collaboration with JPL and supported by the NASA Space Technology Research Fellowship, began development of a third nested Hall

thruster, the N30. A picture of the thruster and cathode after manufacturing can be seen in Fig. 4.4.

The main objective of the N30 was to continue the development of nested Hall

Figure 4.4: A picture of the N30 after manufacturing before initial plasma.

thrusters towards their path to flight as well as provide a testbed for thruster physics and developments in technology. With these high level goals in mind, the specific objectives of the device were to

- Implement a magnetic circuit that provides magnetic shielding up to 800 V in any firing configuration,
- Provide a high-power (25-50 kW), high specific impulse (up to 3000 s) laboratory nested Hall thruster capable of being tested at facilities in the United States at relevant pressures (less than 20μTorr),

- Provide a mechanical design that is simple and flexible such that it can accommodate various diagnostics and potential hardware changes,
- Have the inner channel have an identical geometry and a similar magnetic field shape to a well benchmarked single channel thruster in order to study channel interactions and the differences between single channel and nested Hall thrusters,
- Provide a testbed for NHT lifetime studies; specifically, be able to investigate if magnetic shielding on nested Hall thrusters achieves the same reduction in channel erosion as well as investigate pole erosion of shared poles.

The design requirements for the N30 are derived from the purpose and objectives listed above. One of the main goals of the N30 is for the inner channel to be as similar to the H9 design as possible such that results between the two thrusters are easily comparable. [123] With this in mind, there are many similarities between the N30 inner channel and the H9. These include identical discharge chamber geometries (mid-channel diameter, channel width, and channel length), an identical anode/gas distributor design, and an internal (to the discharge chamber) magnetic field shape that is nearly identical. Due to differences in the surrounding magnetic material environment, it is impossible for these fields to be identical in the far field (outside of the discharge chamber).

As with the H9, a segmented discharge channel with replaceable rings near the exit region was implemented for both channels to enable future research into material selection. Additionally, there were several requirements for the outer channel and the thruster as a whole. Some thruster-wide requirements include graphite pole covers to mitigate pole erosion [163], a magnetic circuit that provides dual-channel magnetic shielding as well as the ability to operate in single channel and dual channel modes, a consideration for the thermal environment of the thruster to enable high-power dual channel operation, and a single, high-current LaB_6 hollow cathode. The cathode design was further restricted to ensure that

it could be used on both the H9 and the NHT in order to eliminate cathode changes as a difference in operation. Finally, there were two main requirements for the outer channel: (1) proper scaling to ensure high-specific impulse (same as the inner channel) operation and (2) a anode/gas distributor design that was similar to the inner channel. A full description of the thruster and the acceptance testing is provided in Appendix B.

Overall, the N30 is a two-channel thruster with a nominal power range of 4.5-33 kW. For the studies herein, the N30 was operated in single-channel mode with only the inner channel firing. It was operated at 300 V and 15 A, for a total power of 4.5 kW. The outer channel did not operate, however, gas was injected into the outer channel anode at a mass flow rate that corresponds to a 40 A discharge current (equivalent to the 15 A current for the inner channel).

4.2.4 Cathodes

The cathode supplies electrons for both the discharge and neutralization of the plume. Throughout these investigations, we used three different cathodes. All three used lanthanum hexaboride inserts. Two of these cathodes were 20-A class cathodes, originally developed for the H6 Hall thruster. [155] One used a sheathed heater and the other a filament heater. [164] These two cathodes were used for the H9 and X2 experiments. The sheathed heater design was used as the internal cathode for both experiments. The filament heater design was used as an external cathode during the H9 experiments. It was mounted at the twelve o'clock position and angled towards the discharge. A picture of one cathode is seen in Fig. 4.5. For all nested Hall thruster investigations, the cathode was centrally-mounted. The original cathode used for the H9 testing has been operated up to 60 A during development. [154,155] However, at its highest nominal operating condition, the N30 requires 71.8 amperes of current. Thus, a new cathode was required for this thruster. In order to achieve higher current, the LaB_6 insert size was increased to emit currents up to 100 A. However, the overall form

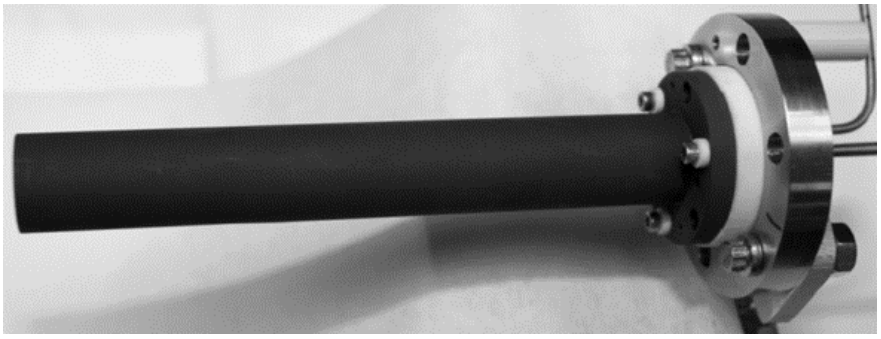

Figure 4.5: One of the 20-A class cathodes used during these investigations. This cathode has the traditional sheath heater and was used for the X2 and some H9 experiments.

factor of the cathode did not change. This was critical to enable this device to be used with both the H9 and N30 thrusters. Additionally, there are design features on the cathode that ensure the exit plane of the keeper is at the same axial location on both thrusters. During initial testing, the cathode was operated up in diode mode to 60 A. This device is now the nominal electron source for both thruster the H9 and the N30. The design can be seen in Fig. 4.6. This cathode was used for some of the H9 testing and all of the N30 testing.

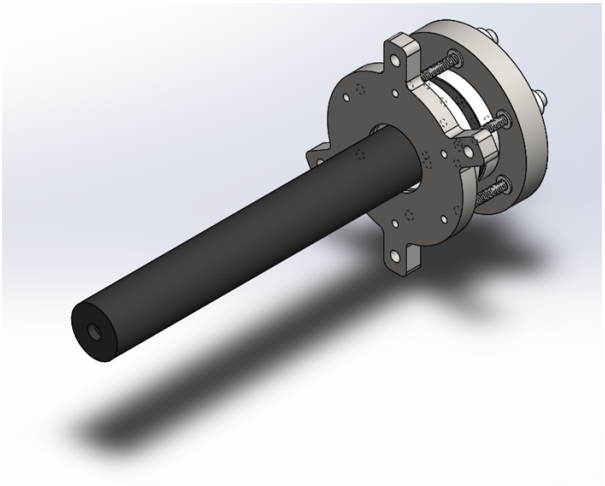

(a)

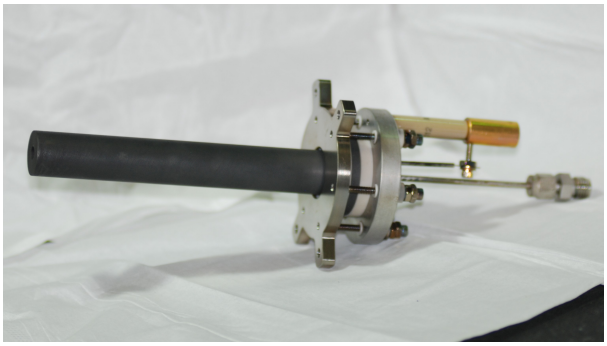

(b)

Figure 4.6: Solid model of the new 60-A cathode (a) and a picture of the cathode after manufacturing (b).

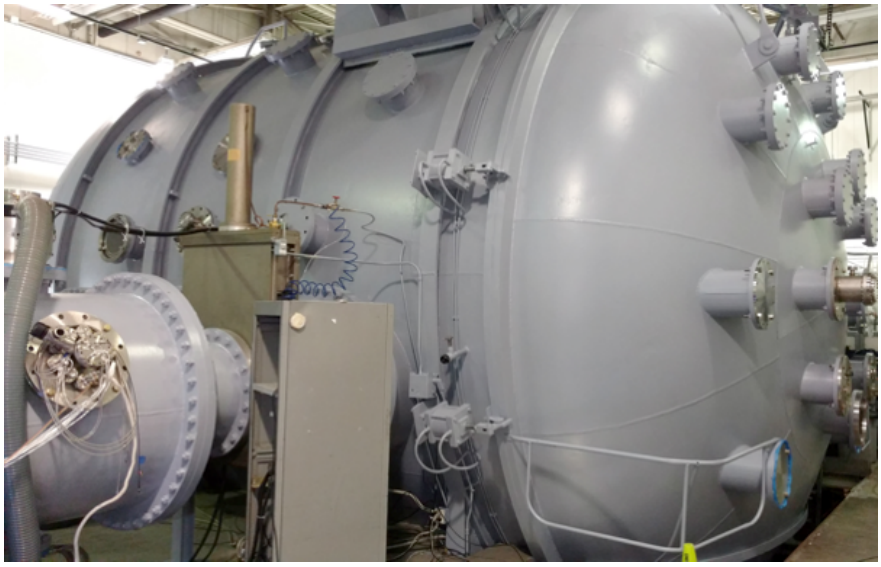

Figure 4.7: The Large Vacuum Test Facility at the University of Michigan.

4.3 Facility

4.3.1 The Large Vacuum Test Facility

All testing occurred in the Large Vacuum Test Facility (LVTF) at the University of Michigan. The facility is six meters in diameter and nine meters long and uses four mechanical pumps to achieve rough vacuum. During this work, the chamber went through upgrades. The first experiment, on the X2, occurred when the chamber had seven LN_2-baffled TM-1200 CVI cryopumps and a pumping speed of approximately 240,000 L-Xe/s to achieve a base pressure of 0.1 μTorr-N_2. We used a Varian Series UHV-564 ion gauge to measure pressure at the chamber wall approximately one meter downstream of the thruster. The chamber pressure was 6.8 μTorr-Xe during operation. In 2016, Dankanich et al. published a standards paper for pressure measurements in electric propulsion testing. [165] Based on these recommendations, for the remainder of testing, pressure was monitored with a Series 370 Stabil Ion gauge located approximately one meter radially away from the thruster in line with the thruster exit plane, as seen in Fig. 4.8. The gauge had a grounded copper mesh surrounding the entrance to prevent ambient plasma from entering. Wall pressure was

also monitored with a Series 370 Stabil Ion gauge. Between 2017 and 2018, the LVTF was upgraded to have thirteen LN_2-baffled TM-1200 CVI cryopumps and six copper cryogenic "thumpers" in order to achieve high vacuum with a pumping speed above 500,000 L-Xe/s. Base pressures were below 0.1 μTorr-Xe and typical operational pressures varied from 1 to 25 μTorr-Xe during H9 and N30 testing.

The facility supplies aerospace-grade xenon to the thrusters via a mass flow manifold with five commercially available flow controllers. For these experiments, four different flow controllers were used with maximum throughput of 50, 400, 800, and 3000 sccm respectively. The 50 sccm controller was dedicated to the cathode. The 400 sccm controller was used for the H9 anode, the inner channel of the X2, and the inner channel of the N30. The 800 sccm controller was used for the outer channels of the N30 and the X2. At points, there were multiple cathodes installed in the chamber. However, we never ran both cathodes at the same time. The layout of the flow manifold allowed for the 50 sccm controller to be diverted to a second inlet flow line. Thus, both cathodes were able to be controlled with the same controller. For all experiments, there was a desire to be able to carefully control the background pressure of the facility and artificially raise it to study the impact of neutrals. This was done with the last flow controller. The inlet to the facility was placed facing away from the thrusters to ensure neutrals were not preferentially being directed toward the thruster located approximately two meters radially away and one meter downstream from the thruster.

Power for all experiments was provided by commercially available laboratory discharge supplies. Three supplies were used; each is capable of 60, 100, and 150-kW of discharge power respectively. While nested Hall thrusters can be run off a single power supply, we used an independent commercially-available power supply for each channel. If a channel was not being operated, i.e. during single channel operation, that channels power supply

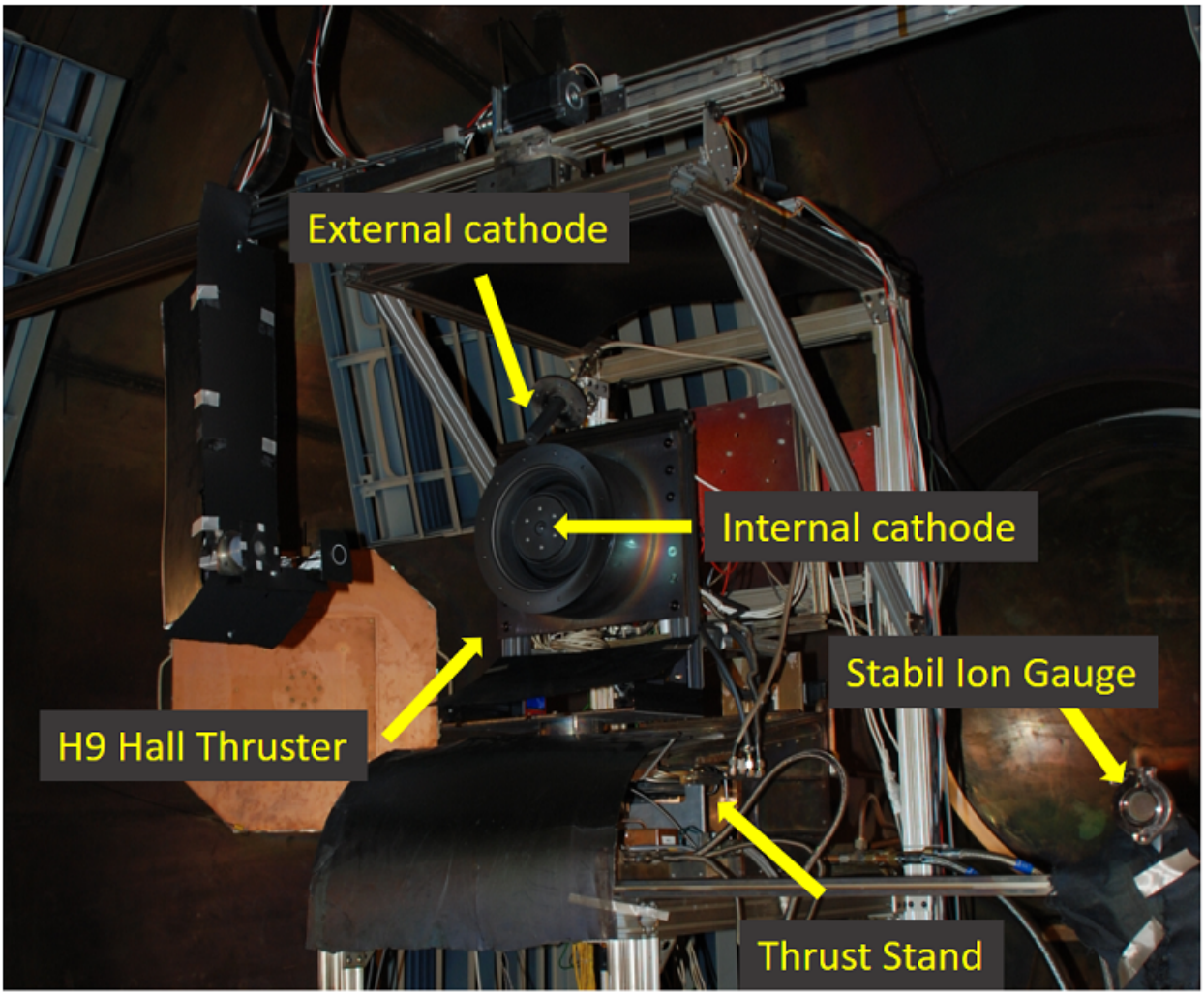

Figure 4.8: Example of the internal setup in LVTF. Here, the H9 Hall thruster is seen mounted on the thrust stand. The 60-A cathode is internally mounted and one of the 20-A cathodes is being used as an external cathode. The location of the pressure gauge is seen in the foreground.

was not activated. The negative side of the power supplies (cathode return) were shorted together at the power feedthrough into the chamber. Six commercially available power supplies were used to power the cathode heater, keeper, and electromagnets.

Standard telemetry (DC values) was recorded using LVTF's data acquisition system which is LabView based, optically isolated, and logs data once per second. These values include currents and voltages for the electromagnets, heater, keeper, discharge, and body, as well as the facility pressure, anode and cathode flow rates, and cryo and thruster temperatures. Additionally, high-speed thruster oscillations were measured using Tektronix AC coupled clamp-on current probes and Tektronix high-speed differential voltage probes. We then recorded the anode current oscillations, cathode current oscillation, discharge voltage oscillations, and cathode-ground voltage oscillations using a four-channel 500 MHz, 5 MSa/s per channel Agilent oscilloscope.

4.4 Diagnostics

To characterize the thrusters, we used a multitude of diagnostics including: a thrust stand, neutral pressure probe, plasma probes (Faraday probes and Langmuir probes), and laser-induced fluorescence. Below, we will detail each of these techniques and discuss in general, the setup for these experiments.

4.4.1 Thrust Stand

We measured the thrust produced by all three thrusters using an inverted pendulum thrust stand. [166, 167] A picture of the H9 on the thrust stand is shown in Figure 4.8. The thrust stand was water cooled to maintain a constant temperature during testing. During H9 and X2 testing, flexures were used to support the mass of the system. There are 8 flexures positioned evenly between the four corners. These flexures are designed to

easily accommodate thrusters up to 75 kg. Additionally, a spring was used to provide the restoring force. The displacement was measured using an optical sensor. Current to the electromagnets was controlled with a proportional, integral, and derivative (PID) controller using the displacement as an input signal. Specifically, we used a Stanford Research Systems SIM960 PID controller. We operated the thrust stand in null mode with active inclination control. During the initial testing, there were issues with the inclination control algorithm such that the motor that controls the inclination was continuously running. Not only did this increase the noise of the system, but it also impacted the thrust signal. In order to overcome this, a new algorithm for thrust stand control was implemented. This algorithm increased the dead-band width of allowable inclinations such that the motor was only on periodically. Additionally, one minute prior to turning the thruster off, the inclination control was turned off such that a true change in signal could be recorded. Changes in inclination between the thruster on and the thruster off during measurement were calibrated out a posteriori by performing an inclination versus signal calibration.

The thrusters were run through an outgassing and warm up procedure before any measurements were taken. During outgassing (anytime the thruster had been exposed to atmosphere), the thruster was run at the highest power condition and DC and AC discharge current levels were monitored. No data was taken until there was no change in the DC or AC current components for ten minutes or two hours had passed, whichever was longer. For warm up, the thruster was run at full power for at least one hour each day prior to taking data. Additionally, power to the electromagnets was left on continuously during testing such that the thruster remained "pre-heated" at all times. Calibrations were performed by dropping a series of known mass weights; inclination was controlled during calibration. The uncertainty of the thrust data was taken as the standard deviation of the thrust signal which was typically 1%-2% of the value.

In order to accommodate the higher-than-average mass of the N30, a number of changes were made to the thrust stand. The "nominal" thrust stand condition is that of the H9 and the X2. Most notably, the spring used as a restoring force was changed to a stiffer spring and the flexures were changed to torsional bearings that can support the increased mass. Both of these changes had previously been implemented for testing the X3. [145] Nonetheless, in order to ensure that the thrust stand was still reporting reliable thrust values, we validated this new configuration by testing the H9 on the stand. To get reasonable response, we also added "dummy" mass to the stand to simulate the higher mass of the NHT. We tested the H9 at two of its nominal conditions (300 V, 15 A and 600 V, 15 A). The results showed the thrust measured was well within uncertainty compared to the nominal configuration. The measured uncertainty for the thrust stand was 3%.

4.4.2 Pressure Mapping

During X2 experiments, the local pressure profile for each operating condition was measured using a Varian Stabil Series 370 ionization gauge using cold flow (e.g. no plamsa) testing of the X2. The ionization gauge was placed 0.35 d_{OC} downstream of the thruster exit plane with its entrance perpendicular to the direction in the flow. Figure 4.9 illustrates the test setup. The thruster was placed on motion stages such that a radial sweep of the pressure profile could be measured. The mass flow rate during this measurement was the same as during thruster operation. The local pressure profile was used to determine the neutral density near the thruster exit plane. Additionally, this number density profile was confirmed via numerical simulation. More information about this numerical simulation can be found in Dragnea. [168]

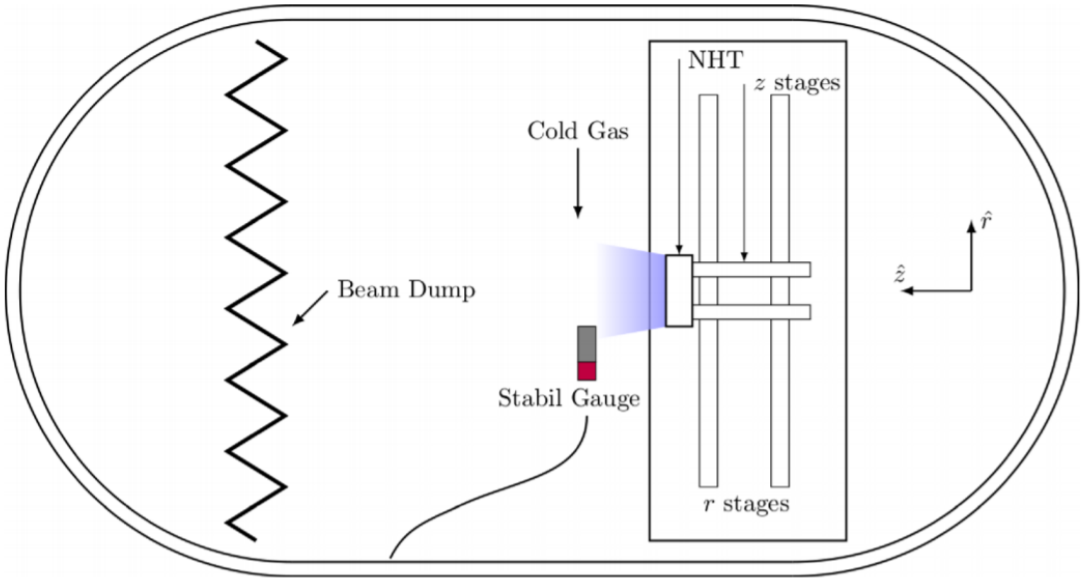

Figure 4.9: Schematic for the test setup of cold flow testing. The thruster was on motion stages and the Stabil-Ion Gauge was pointed perpendicular to the flow downstream of the exit plane.

4.4.3 Probes

4.4.3.1 Faraday Probes

A near-field Faraday probe was used to measure beam current as a function of radial and axial location for the X2. The design of the Faraday probe features a tungsten planar disk of 3.2 mm diameter. There is also an outer guard ring in order to reduce edge effects, as described by Rovey. [169] A picture of the probe can be seen in Figure 4.10. The probe was biased to -40 V during operation to ensure ion saturation. Per standard practice, the guard ring was also biased to -40 V. The probe was placed on two-dimensional motion stages. Several radial scans were taken at axial locations ranging from 0.07 d_{OC} to 0.17 d_{OC} downstream of the thruster. During each sweep, the probe was continuously moving and the position profile was recorded versus time. Current was measured using a Keithley 6485 picoammeter sampling at 60 Hz.

Figure 4.10: Near-field Faraday probe featuring a tungsten collector plate and guard ring.

Using the measured current density profile, the divergence angle of the ion beam was then calculated as

$$\theta(z) = \arctan\left(\frac{r_2 - r_{max}}{z}\right) \tag{4.1}$$

where $\theta(z)$ is the divergence angle at an axial location z, r_{max} is the radial location of the maximum current density, and r_2 is the radial location of the cutoff point. The selection of the cutoff point is discussed below. Due to the nature of nested Hall thrusters, it is necessary to take near-field Faraday probe measurements to distinguish the channels from each other prior to plume merging. To avoid the effects of plume merging, the radial cutoff limit r_2 was set to the 1/e dropoff point of the maximum at each axial location as described by Reid. [170] Equation 4.1 was used to calculate the divergence angle until the downstream location in which plume merging made it impossible to differentiate the cathode plume, the inner channel plume, and the outer channel plume from each other.

4.4.4 Langmuir Probe

During H9 experiments, we aimed to characterize the coupling voltage of the thruster for various neutral density cases. The coupling voltage (defined as the difference between the cathode voltage and the plasma potential in the downstream thruster plume) must be measured. As part of typical thruster telemetry, the cathode to ground voltage is measured. However, the plasma potential must also be measured as this could also be changing. By combining these two measurements, the total coupling voltage can easily be calculated as,

$$V_{cc} = V_p - V_{cg} \tag{4.2}$$

where V_{cc} is the cathode coupling voltage, V_{cg} is the cathode to ground voltage, and V_p is the plasma to ground voltage (plasma potential). A Langmuir probe was used to deduce the thruster plasma potential. Langmuir probes have been widely used to measure plasma potential in electric propulsion devices[23]. The probe was swept from 0 to 20 V in 0.1 V increments and the corresponding current was recorded. The probe was positioned approximately 40 cm downstream of the thruster channel exit plane.

The plasma potential can be found by the location of the "knee" in the current-voltage trace. To find this "knee", the current was first smoothed using a Savitzky-Golay filter. Next, the smoothed data was placed through a numerical derivative algorithm. The maximum of the derivative was used to estimate the plasma potential. As example of this process is shown in Fig. 4.11. The uncertainty was taken as the voltage step size, the half-width of the smoothing length, and systematic uncertainty of the knee combined.

4.4.5 Laser-Induced Fluorescence

The last diagnostic used was laser-induced fluorescence. This technique was used to characterize all three thrusters. In order to assess the centerline and near-wall ion velocity

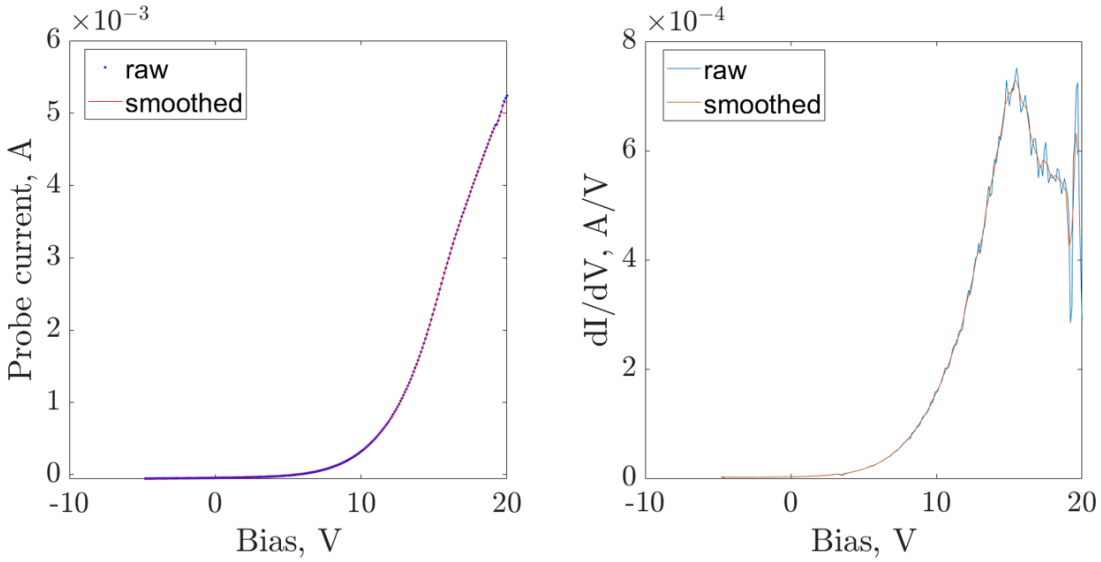

Figure 4.11: Left: An example Langmuir probe trace showing both the raw and smoothed data. Right: The corresponding numerical derivative of this data. The plasma potential was taken as the voltage corresponding to the peak derivative of the smoothed data.

vectors, we employed a standard, non-resonant, multi-plexed laser-induced fluorescence (LIF) scheme. [104, 171, 172] We targeted the $5d^4_{7/2} \rightarrow 6p^3_{5/2}$ metastable transition of xenon ions using a tunable diode laser and a taper amplifier with an output linewidth of less than 200 kHz. We generated measurements of the ion velocity distribution function (IVDF) by injecting this laser into the thruster plasma, sweeping it over a range of wavelengths (834.9 to 835.02 nm), and monitoring the intensity of the fluoresced signal induced by the laser from a fixed point in the plasma with collection optics. A schematic of the system is shown in Fig.4.12.

In practice, the beam was sampled with a photodiode to measure the intensity and then sent through a chopper to mechanically modulate the signal before being collimated and sent into the chamber. Inside the chamber, there were two or three optical elements: the injection optics and the collection optics. The intersection of these elements represents the localized interrogation volume, which was 1 mm^3. Both the injection and collection optics were stationary throughout the experiment. The collection optics, which were placed 60° off

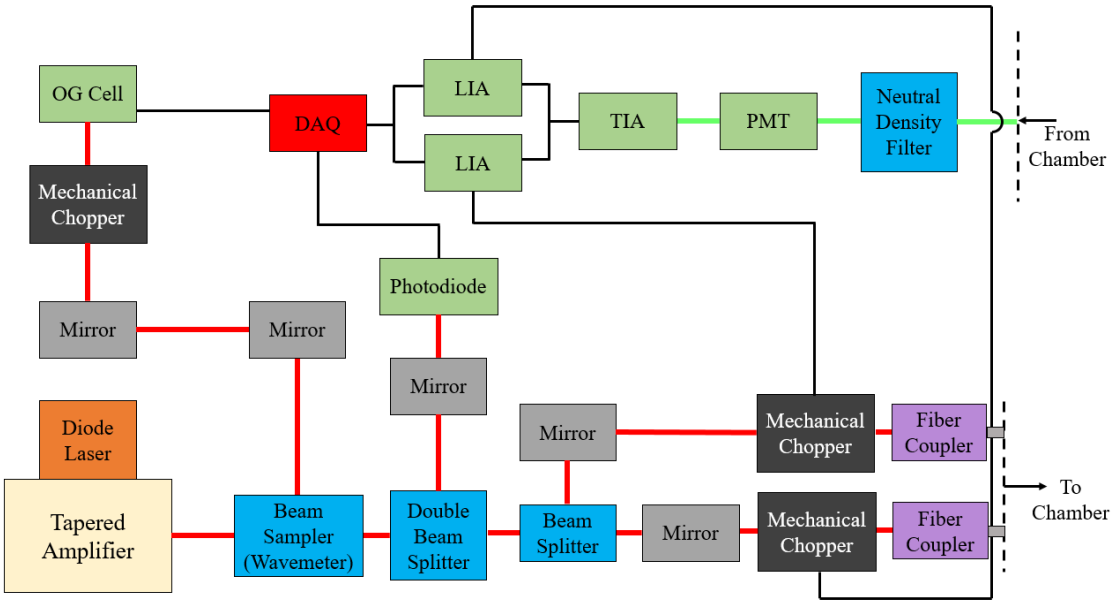

Figure 4.12: Schematic of the laser table detailing both the injection and collection setups. Some of the laser paths have been simplified for clarity (e.g. not all mirrors are shown).

axis to protect them from the plasma plume and allow unlimited access into the thruster, were used to collect the light fluoresced by the ions excited by the laser. This light was then sent out of the chamber and into a monochromator tuned to 541.91 nm. For later experiments, the monochromator was replaced with a line filter with a ±4 nm width. A photomultiplier tube converted the optical signal to an electrical current, and a transimpedance amplifier transduced the signal that was measured by a lock-in amplifier. By measuring the intensity of this as a function of the wavelength and employing a Doppler conversion, we were able to generate spatially resolved measurements of the the IVDF in the thruster plume.

The IVDF measurements are subject to sources of shifts and broadening such as Zeeman splitting and hyperfine structure. However, most of these effects are generally small compared to the Doppler broadening of interest. Additionally, these effects are symmetric about the stationary transition wavelength in the frame of the ion and should not impact taking the first moment to infer average ion velocity Therefore, no corrections for these

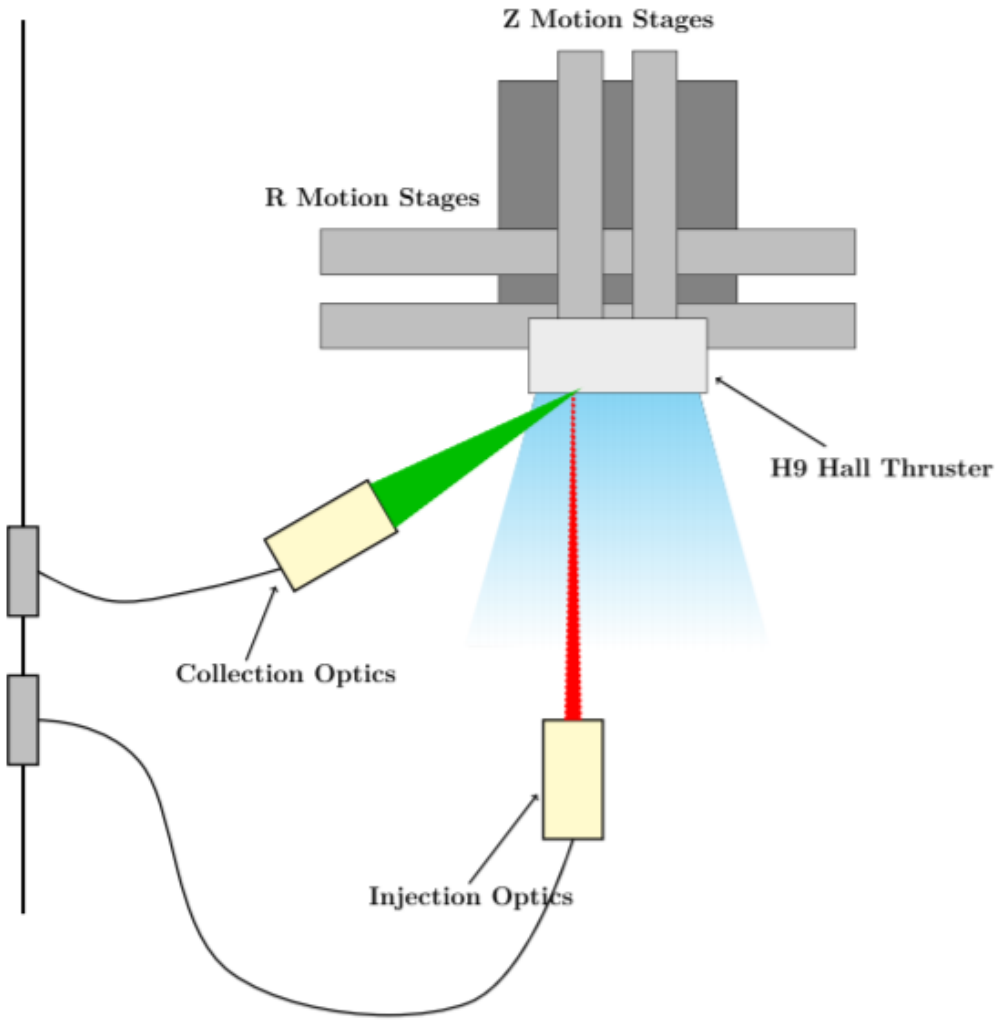

Figure 4.13: Internal setup for measurements of the centerline axial ion velocity distributions.

effects were made. [171, 173]

Figure 4.13 shows the internal setup used to probe the centerline of all three thrusters. During testing, the thrusters were placed on r-z motion stages to vary the interrogation point. In addition to centerline measurements, we also measured the near-wall IVDFs of the H9 and the N30. We did this on the "chamfer" of the discharge chamber. The chamfer is a feature of magnetically shielded Hall thrusters where the end of the wall is chamfered out at an angle to make it easier for magnetic field design. Because the thruster was on motion

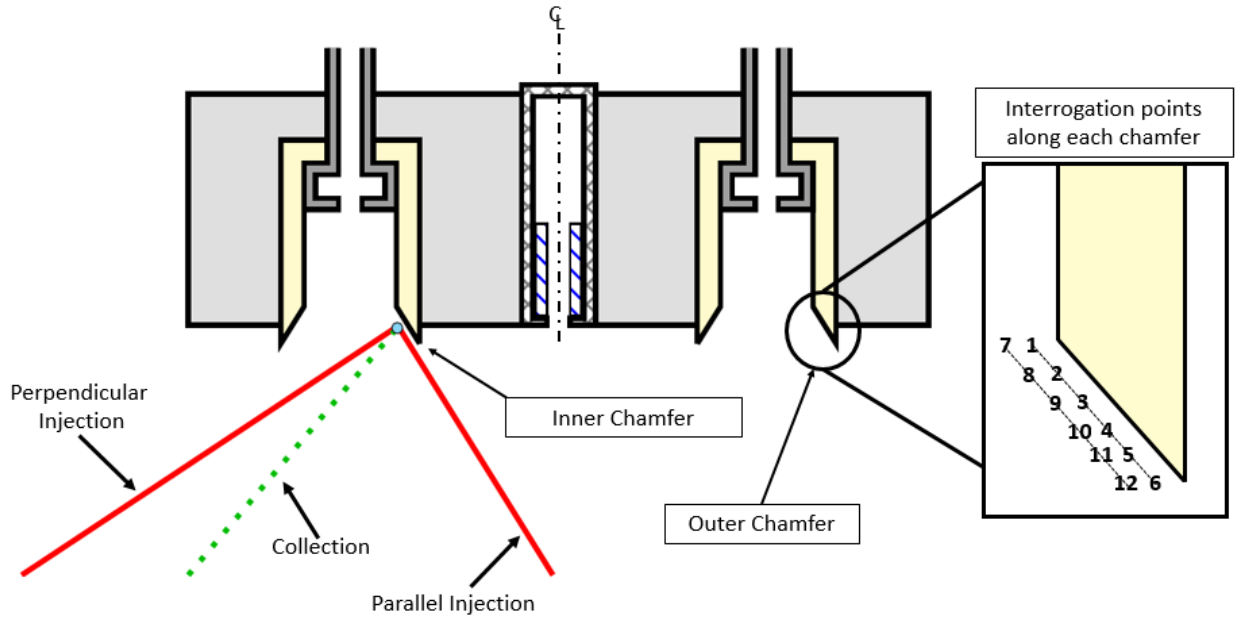

Figure 4.14: A schematic of the chamfer LIF setup for the H9 and the N30.

stages, we were able to measure both the three and nine o'clock positions to get the inner and outer chamfer. On the chamfer, we measured both the parallel and the perpendicular components of the IVDF. To enable this, the laser beam was split and sent through two different mechanical choppers with different chopping frequencies. A picture detailing the interrogation points is shown in Fig. 4.14.

Ion velocity distribution functions were measured at six equally space points along the chamfer at two different axial distances away. In order to analyze the recorded data, we start by integral-normalizing the intensity to get the ion velocity distribution function (IVDF). For all the data, we fit a sum of Gaussians in order to reduce numerical noise in our calculations. An example of this fitting technique is seen in Figure 4.15. Additionally, for some traces, particularly on the inner chamfer, signal from the main ion beam was detected due to the orientation of the collection and injection optics. This only appeared in the perpendicular traces. In order to analyze this data, the Gaussians attributed to the main beam were subtracted from the fit. We then take the first moment of the distribution

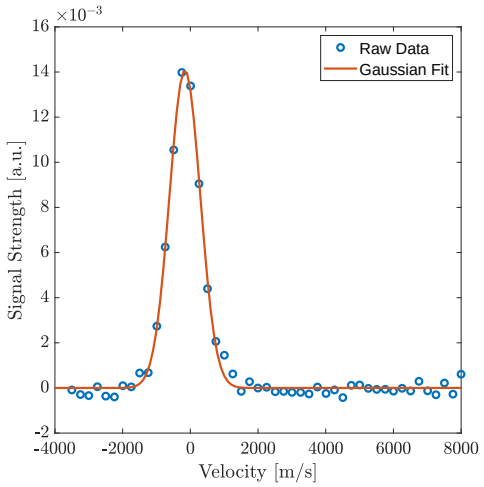

Figure 4.15: An example of a single Gaussian fit for the LIF data collected on centerline for the H9 Hall thruster.

to calculate the mean as,

$$u_{mean} = \int_{u_1}^{u_2} u f(u) du \tag{4.3}$$

where u_1 and u_2 are the upper and lower bounds of velocity space. For the centerline data, we then plot this mean velocity versus position to construct the "acceleration region." We can then fit a spline to the acceleration region and numerically take the derivative to get the electric field. Finally, we assign the "location" of the acceleration as the position of peak electric field. This process is graphically depicted in Fig. 4.16. Finally, the uncertainty in this position is taken as the uncertainty in the interrogation location. For the chamfer data, we take the mean velocity in each direction to create a two-dimensional vector plot of ion trajectories.

4.5 Conclusion

In this Chapter, we detailed all the experimental equipment used to investigate the theoretical framework presented in Chapters 2 and 3. First, we discussed the three thrusters begin used: the H9, the X2 and the N30. We then detailed the LVTF chamber and support

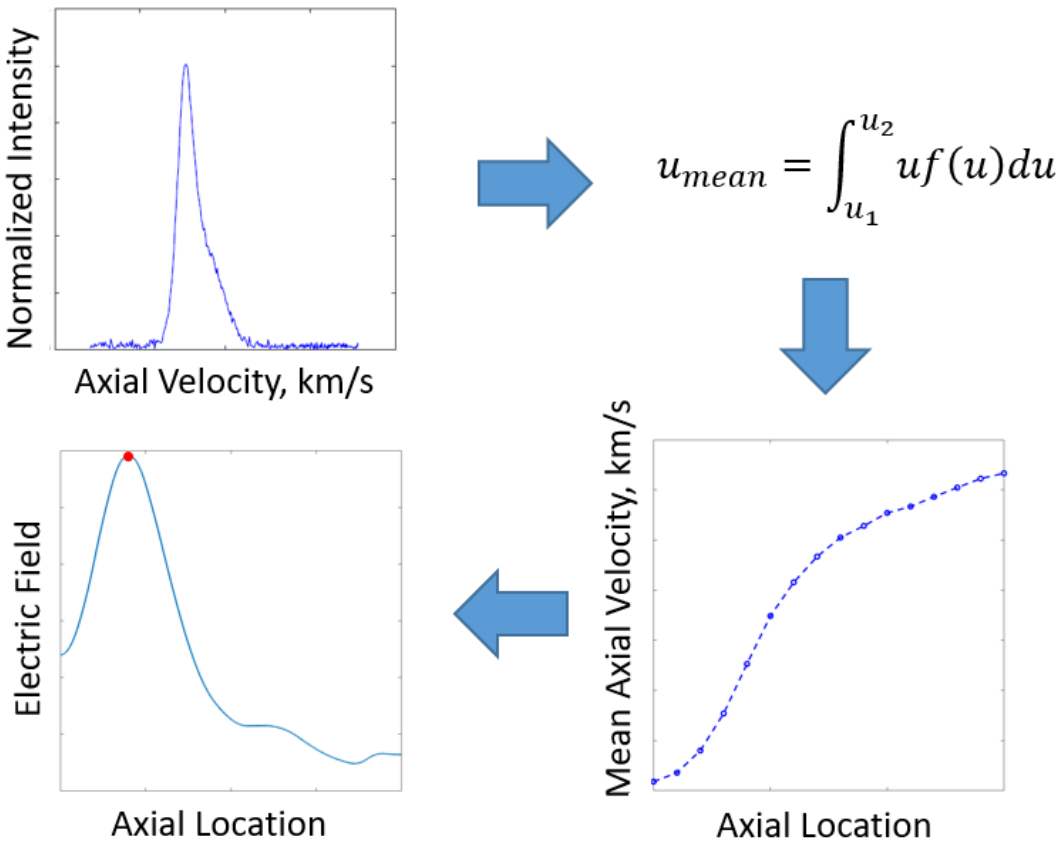

Figure 4.16: Graphical depiction of the process used to "locate" the acceleration region. First, the mean velocity of each trace is taken. Then, the mean velocity versus position is plotted and a spline is fitted to this trace. Finally, the numerical derivative of this spline is taken and the location of the acceleration region is taken as the peak in this derivative.

equipment used to fire the thrusters, including how we modulated the pressure in the chamber. Finally, we discussed the diagnostics used to characterize the thrusters including the thrust stand, Faraday probes to measure ion current density, ion gauges to measure pressure, Langmuir probes to measure plasma potential, and LIF to measure ion velocities. Combined, these diagnostics are used to investigate the different neutral impacts on high-power Hall thrusters.

CHAPTER 5

Impact of Neutrals on the Operation of Magnetically Shielded Hall Thrusters

5.1 Introduction

The goal of this chapter is to present the experimental results from our investigation into the consequences of enhance neutral density in the exit plane of single-channel magnetically shielded Hall thrusters as a result of non-vanishing background pressure in vacuum test facilities.. To accomplish this, we begin by discussing our test matrix. Then, in Section 5.3, we detail the results from the performance measurements on the H9 Hall thruster. Section 5.4 shows the results of the study on neutral impacts to near-wall ion trajectories. Finally, we making concluding remarks on the results with emphasis on points to be presented in the discussion chapter.

5.2 Test Matrix

In Chapter 2, we discussed that neutrals may impact magnetically shielded Hall thrusters in two main ways: performance effects and magnetic shielding changes. In particular, we discussed how changes in the cathode coupling and acceleration region are directly traceable to those in performance. Thus, in order to quantify the variation in these two parameters with the neutral environment, we measure the cathode coupling voltage (using a Langmuir

probe), the acceleration region location (using laser induced fluorescence), and the thrust (using a thrust stand) while varying the local neutral density.

In order to manipulate the local neutral density we use two mechanisms: (1) artificially increasing the background pressure of the facility and (2) changing the cathode flow fraction of the thruster at a constant power. The cathode flow fraction (CFF) is the percent of the anode flow that is sent through the cathode ($\dot{m}_c = CFF \cdot \dot{m}_a$). It can be used as a proxy for changing the local neutral density as increases in this parameter should not significantly impact the facility pressure. This is because changing the cathode flow fraction only results in a very small increase in the total mass flow into the facility. Most thrusters run on an empirically-derived cathode flow fraction of 7-10%. [8] Here, we varied the cathode flow fraction from 5 to 15% for both an external and internal cathode. We augmented the test matrix to include external cathode because many flying thrusters use external cathodes. Additionally, it provided a third location for injection to better understand if the source of the neutrals was critical. For the pressure study, we varied the facility pressure from 4 to 30 μTorr-Xe. Finally, we also simultaneously injected excess neutrals through the background and cathode. This allowed us to determine if the source of the neutrals was critical to the changes.

For the study on the impacts of neutrals on the magnetic shielding of single-channel thrusters, we measured the two-dimensional ion velocity distribution functions at 4.6 and 15.8 μTorr-Xe, along the chamfer of both the inner and outer walls. We performed these measurements in sixteen locations, detailed in Chapter 4.

5.3 Performance Impacts

We start by presenting the results from the study on performance impacts. First, we focus on the acceleration region measurements for both the internal and external cathode, followed by the cathode coupling measurements, and finally, the thrust measurements. Figure 5.1 shows

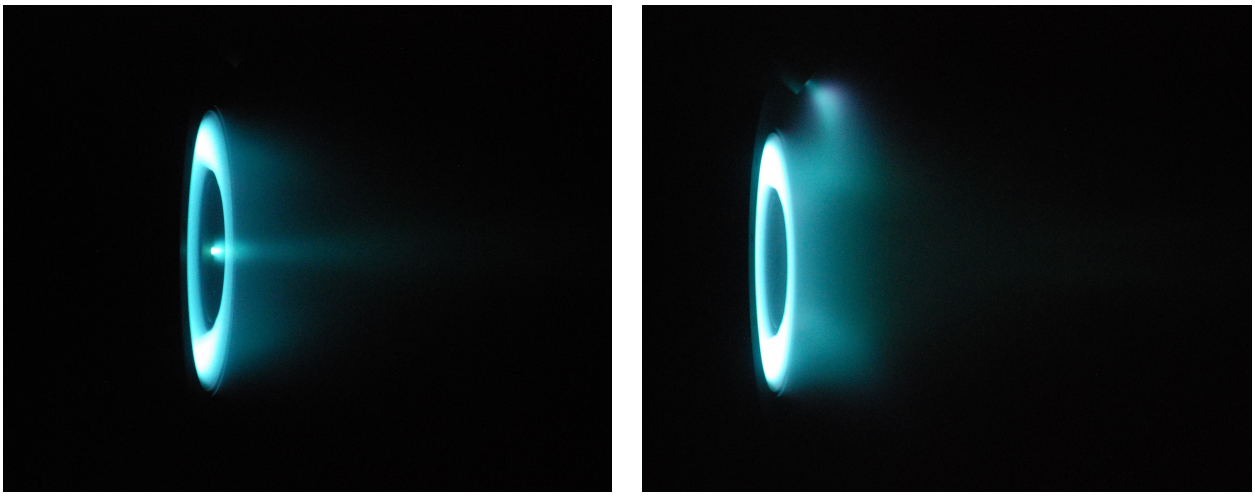

(a) (b)

Figure 5.1: The H9 Hall thruster firing at 4.5 kW during this investigation using the internally mounted cathode (a) and the externally mounted cathode (b).

the thruster operating with both the internally mounted and externally mounted cathode. The plume structure is visibly changed between the two different modes. This is an expected results and has been seen by others. [28, 64]

5.3.1 Acceleration Region

Figure 5.2 shows the average velocity profile of the acceleration region (calculated using Eqn. 4.3). As expected, the acceleration region shifts inward as the facility pressure increases for both cathodes. This result has been documented on other Hall thrusters [97, 105] and magnetically shielded thrusters with internally mounted cathodes. [173] When operating on the external cathode, the position of the acceleration region appears to be more susceptible to a change in neutral density than for the internal cathode. Interestingly, it appears that

the exit velocity of the ions increases with facility pressure when operating on the external cathode. This suggests that the accelerating voltage may be changing with facility pressure and possibly increasing the thruster efficiency. This result is indicative of changes in the cathode coupling voltage, which is known to be impacted by the presence of additional neutrals. However, it is difficult to know whether this is simply due to the extent of the measurement, i.e. the ions may have continued to be accelerated beyond our farthest point of interrogation. Regardless, these data show that high-power magnetically shielded Hall thrusters behave similarly to unshielded thrusters with changing neutral density. This has been documented by others. [28] However, here we attempt to extend these results to neutrals in general and not specifically facility neutrals. Critical to this, we see that there is a plateauing effect, i.e. saturates beyond a critical neutral density and the acceleration region no longer shifts inwards. If the thruster exhibits the same behavior for all neutral sources, this would suggest that we can saturate the effect with one source and the thruster would be impervious to other sources of neutrals. This hypothesis will become critical to understanding the mechanism of these effects.

Figure 5.3 shows the evolution of the ion velocity as a function of position for varying cathode flow fraction. Figure 5.3(a) shows this development for the internally mounted cathode while Fig. 5.3(b) shows the measurement for the externally mounted cathode. In general, our results demonstrate that the acceleration region shifts inward with increasing cathode flow fraction. These measurements indicate that changes in the neutral density as sourced by the cathode can also impact the location of the acceleration region of magnetically shielded Hall thrusters. This is consistent with our previous measurements, which to our knowledge are the first documented shift in the acceleration region location with varying cathode flow fractions. [27] Also, as expected, the externally mounted cathode appears to have larger shifts than the internally mounted cathode. Unlike previous results, there does not appear to be a plateauing of the shift with varying cathode flow fraction for

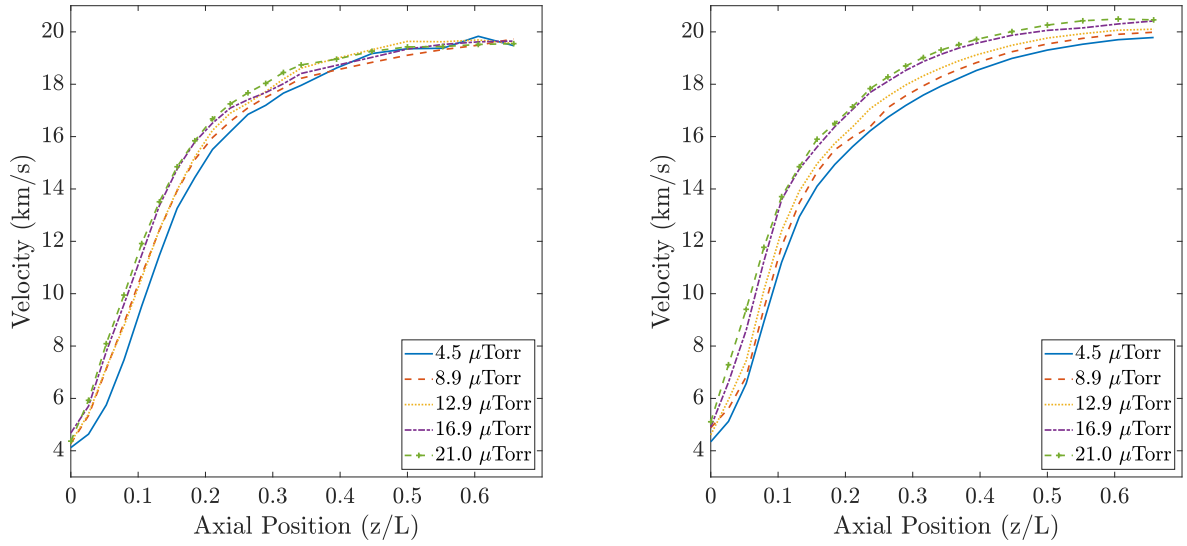

Figure 5.2: Acceleration region measurements (of the mean velocity) versus pressure for both the internally mounted (a) and externally mounted (b) cathode.

the externally mounted cathode. This is likely because Hall thrusters operating with an external cathode are more susceptible to these neutral effects, as seen by Hofer et al. [64] However, for the internal cathode, we do see that the same plateauing effect occurs for cathode flow fraction as did for the pressure study. This outcome indicates that changing the cathode flow fraction induces similar modifications in thruster behavior as varying the background pressure. This result provides further evidence that the source of neutrals is not critical. The thruster responds to neutrals regardless of the source.

Finally, we characterize the acceleration region at high cathode flow fraction and high pressure as an attempt to saturate this shift with cathode neutrals and determine if the facility neutral sensitivity is eliminated. Thus, if the plateau onsets at lower changes in facility neutrals with elevated cathode flow fraction, then the effect of the neutrals on the acceleration region has been "saturated." Figure 5.4 shows the results of this study. We see that for the internal cathode, there is essentially no shift in the acceleration region

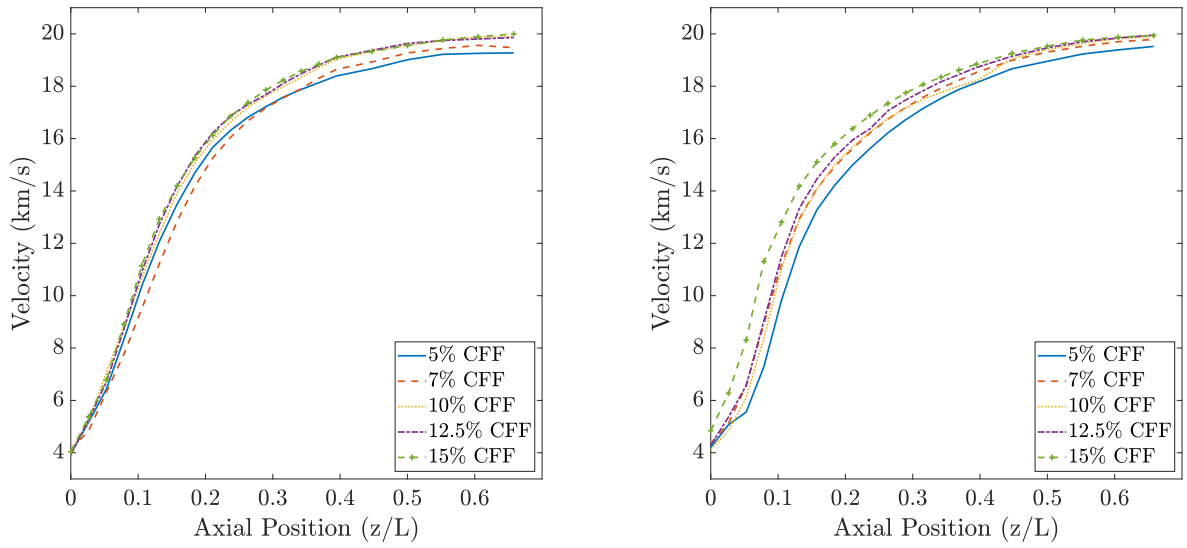

Figure 5.3: Acceleration region measurements versus cathode flow fraction for both the internally mounted (a) and externally mounted (b) cathode.

versus background pressure when the cathode flow fraction is increased. This indicates that the facility neutrals likely impact the thruster through the same mechanism as cathode neutrals. Additionally, it shows that the process is not linear and can be quenched. The results for the external cathode still show the region shifting; this is not unexpected as the thruster operating with an external cathode is more susceptible to facility neutral and the "saturation" density was not reachable even at the highest cathode flow fraction for the external cathode. A significantly higher cathode flow fraction would be needed to see the same behavior. In Chapter 7, we will "locate" the acceleration region which gives an estimate of how high the cathode flow fraction would need to be to saturate this effect.

As an aside, one of the current risks for transitioning Hall thrusters from ground testing to flight are these so-called facility effects in which the behavior changes with varying pressure. Above, we showed that it is the neutrals that the thruster is responding to and it does not care where these neutrals come from. Thus, this provides a potential "risk

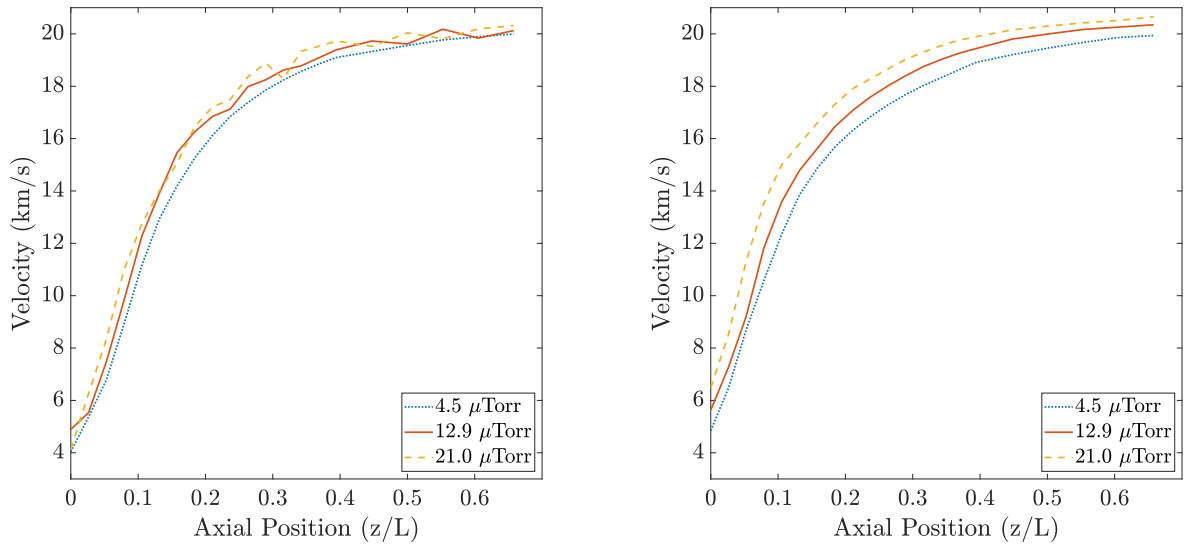

Figure 5.4: Mean ion velocity as a function of position for the external (a) and internal (b) cathode versus background pressure when the cathodes are operating at 15% CFF.

mitigation" strategy to flight operators. This application will be discussed further Chapter 7.

5.3.2 Cathode Coupling

Here, we present the results from the Langmuir probe measurements of cathode coupling voltage. For this study, we aim to characterize the coupling voltage versus both cathode flow fraction and facility pressure as both are ways to change the neutral environment. Additionally, differences between the results may help identify the mechanism behind neutral impacts.

The cathode coupling voltage for each condition is seen in Figure 5.5. The uncertainty for all conditions is 0.5 V, except for the second pressure condition, where it is 2 V. We remind the reader that this is total cathode coupling voltage, where $V_{cc} = V_p - V_{cg}$. As expected, with an increasing cathode flow fraction, the total coupling voltage decreases. As we discuss

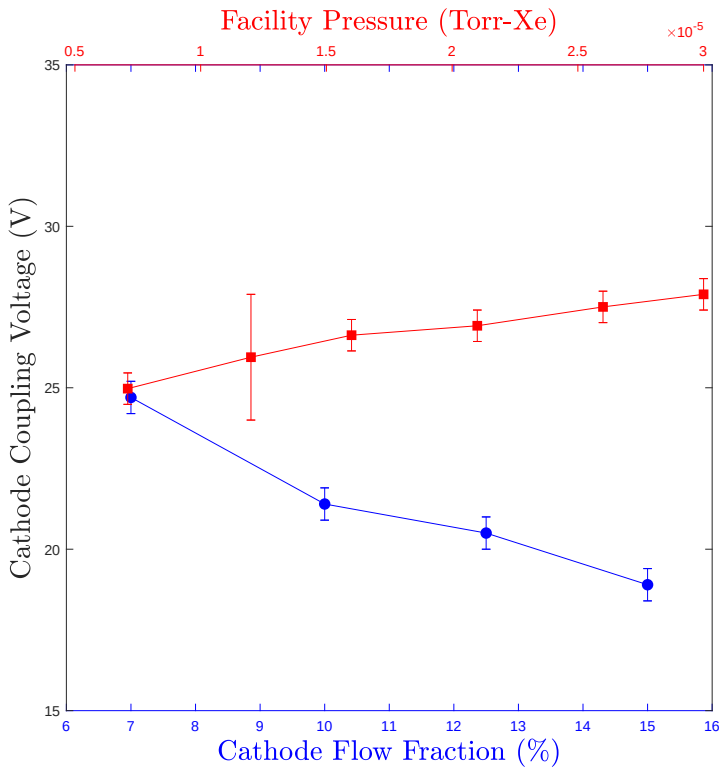

Figure 5.5: Cathode coupling voltage versus both cathode flow fraction and background pressure as measured from the Langmuir probe.

in Ref. [88] and Spektor discusses in Ref [174], changing the neutral profile near the cathode can increase the electron mobility in the cathode plume, thereby making it easier to couple to the plume and requiring less voltage. Despite the fact that the neutral density is increasing, increasing background pressure shows the opposite trend as increasing the cathode flow fraction. The coupling voltage for these cases goes from 24.7 V at the lowest pressure to 27.7 V at the highest pressure. One plausible explanation for this is that the thruster ran in constant power mode. This means that as the background pressure increases the flow rate to the thruster is decreased to compensate for neutral ingestion. As the anode flow decreased, so did the cathode flow to maintain a constant cathode flow fraction. The results here also support the notion that decreasing the cathode flow increases the coupling voltage. Therefore, close to the cathode, with increasing pressure, the neutral density would actually decrease slightly. This could explain the trend seen in Figure 5.5. Alternatively, results from the H6MS showed that the cathode-to-ground voltage (a proxy for cathode coupling) increased with pressure on the same order of magnitude. [28] We discuss this result more in Chapter 7.

5.3.3 Performance

Finally, we aim to characterize the overall change on performance versus pressure and cathode flow fraction. This helps connect changes seen in the acceleration region and cathode coupling to measurable changes in thrust. It also captures whether another process that changes with neutral density impacts the performance. Figure 5.6 shows the thrust with varying cathode flow fraction. As expected, the thrust for the externally mounted cathode is lower than the thrust measured with the internally mounted cathode. Previously, this was seen by Hofer et al. on both unshielded and magnetically shielded Hall thrusters. [28, 64, 93] We find that from the lowest to the highest cathode flow fraction (5% to 15%) the thrust increases for the internally mounted cathode by 4.5% and for the externally mounted cathode by 5.3%. This is more evidence that changes in the cathode

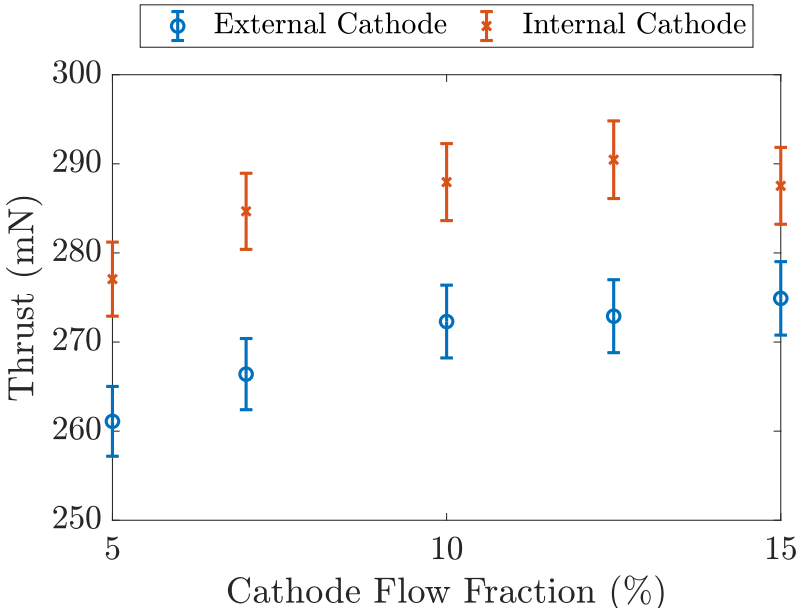

Figure 5.6: Thrust versus cathode flow fraction for both the internally and externally mounted cathodes.

flow rate has a similar impact on the acceleration region as facility neutrals. Additionally, these results confirm that the upstream displacement of the acceleration region with varying cathode flow fraction does indeed result in observable improvements in thrust. Despite this increase, the total efficiency remains static due to the increased mass flow to the cathode. While the anode efficiency increases with increasing flow fraction, from an overall thruster perspective, there is no measurable change.

Figures 5.7(a) and 5.7(b) show the data for three different cathode flow fractions (7%, 10% and 15%) with varying background pressures. The red shaded area is representative of the uncertainty for the 10% cathode flow fraction condition. As expected, the thrust is largely invariant with background pressure for the internally mounted cathode; there is no change with cathode flow fraction within the uncertainty of our measurement. With the externally mounted cathode, the thrust increases with pressure. This trend has also been seen by others. [94] At the nominal 7% flow fraction condition, when the pressure was decreased from 21 μTorr-Xe to 5 μTorr-Xe, the thrust decreased 7.1% for the externally mounted cathode. For the same reduction in pressure, when the cathode flow fraction was

increased to 15%, the thrust only decreased 4.4%. This is a notable finding as it suggests that increasing the cathode flow fraction makes the thruster less susceptible to neutral changes. Again, this is more evidence that the thruster is responding to neutrals, regardless of source. Coupled with the results in Fig. 5.3 for the acceleration zone, this suggests that similar effects can be achieved provided neutrals are ingested (regardless of where these extra neutrals originate).

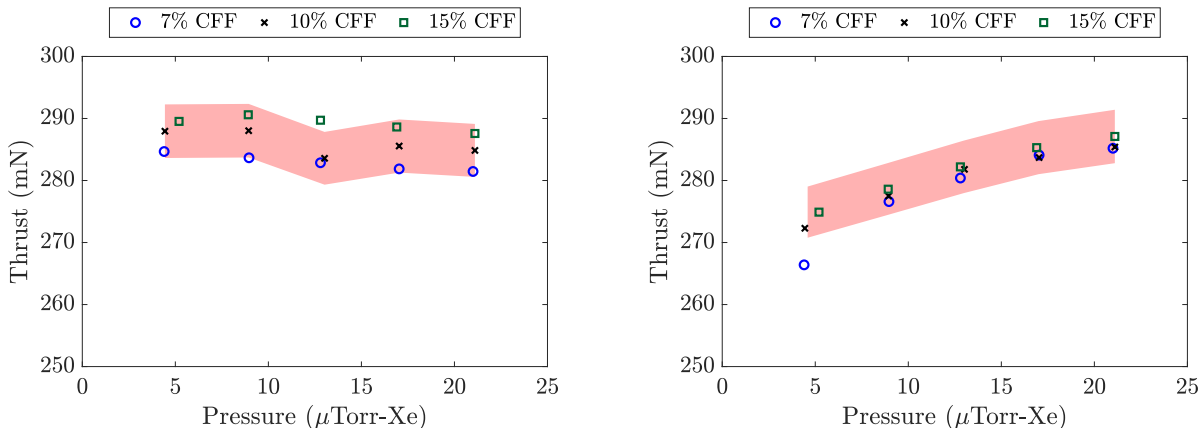

Figure 5.7: Thrust versus pressure at three different cathode flow fractions for the internally mounted (a) and externally mounted cathode (b). The red shading is representative of the uncertainty at the 10% CFF condition.

5.4 Magnetic Shielding Impacts

In addition to the influence of neutrals on the performance of high-power magnetically shielded Hall thrusters, we also aim to investigate whether neutrals impact the level of shielding, and consequently, the overall lifetime of these thrusters. One of the challenges that has emerged from this previous work, however, is how to establish whether the "shielding" effect has been achieved. Indeed, while the least ambiguous proof would be a demonstration of extended lifetime, the projected life of shielded thrusters can be greater than 10,000

hours. This makes direct testing prohibitively expensive and time-consuming. As a faster alternative, several criteria have been proposed (informed by theory [3, 18, 19]) that serve as indirect signs of "effective" shielding. These include (1) low electron temperature and high plasma potential along the entirety of the wall (e.g. as measured by Hofer et al. [20]), (2) low ion kinetic energy at the walls before the sheath (e.g. as measured by Grimaud [119], Chaplin [173] and Huang [175]), and (3) qualitative visual indications such as low luminosity of the plasma near the walls and carbon build up due to back-sputtering in test facilities (e.g. as shown by Hofer et al. [20] and later by Cusson et al. [152]). Criteria 1 and 2 offer measurable criteria for which slight changes in the amount of shielding can be quantified. Here, we choose criterion 2. The technique (chamfer LIF) was described in Chapter 4.

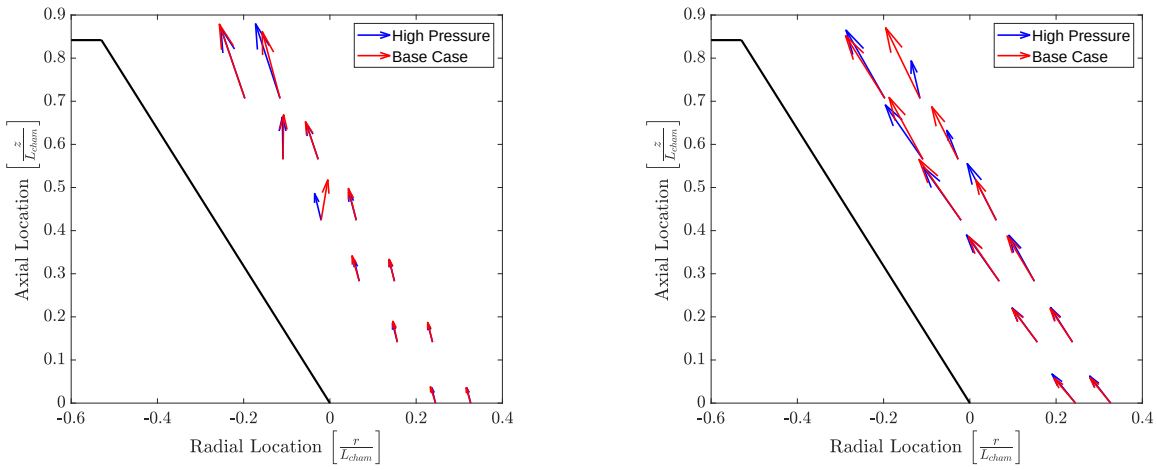

(a) (b)

Figure 5.8: Ion velocity vectors for both the base pressure case and the high pressure case along the inner (a) and outer (b) wall of the H9 Hall thruster.

Figure 5.8 shows the vector plots (of the mean velocity) along both walls for each case of the H9. Overall, we see the profiles are qualitatively similar for both chamfers. Both chamfers show vectors that are expected, with the majority of the motion out of the channel and very little motion towards the wall. The outer wall of the H9 does show

that in some locations, the vector has "turned" towards the wall at high pressure as compared to low pressure. This is expected with a shift in the centerline profile. Regardless, the largest mean velocity towards the wall is 160 m/s. This corresponds to a very low directed energy and even with an electron temperature of 10 eV, the sheath would still be sufficiently small (31 V) to eliminate erosion. However, we must also look at the width of the distribution, as an increase in the high velocity tail may contribute to enhanced erosion.

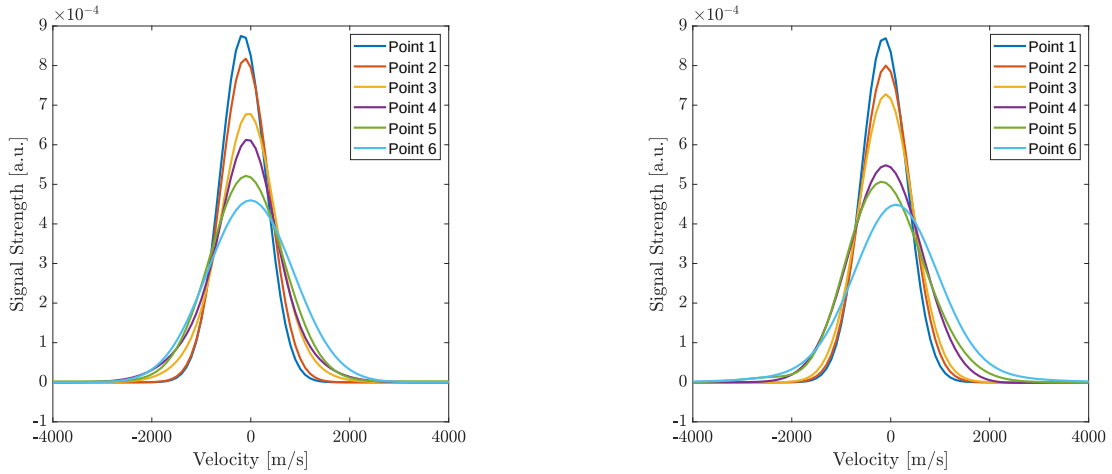

Figure 5.9: Perpendicular VDFs along the outer channel wall at the base case (a) and at high pressure (b). Here, the thruster is operating at 300 V and 15 A.

Figure 5.9 shows the perpendicular velocity distribution functions (VDF) along the wall of the outer chamfer for the base pressure case of the H9, for points shown in Fig. 4.13 All points are a constant distance from the wall. We see that although Point 6 has one of the most positive average velocities, it also has the longest "tail" in the negative (toward the wall) velocity space. This was also true for the high pressure case. Thus, in order to perform a sheath analysis, we look at Point 6 for both cases. The negative velocity portion of the VDF for each case is converted to an ion energy distribution function (IEDF)

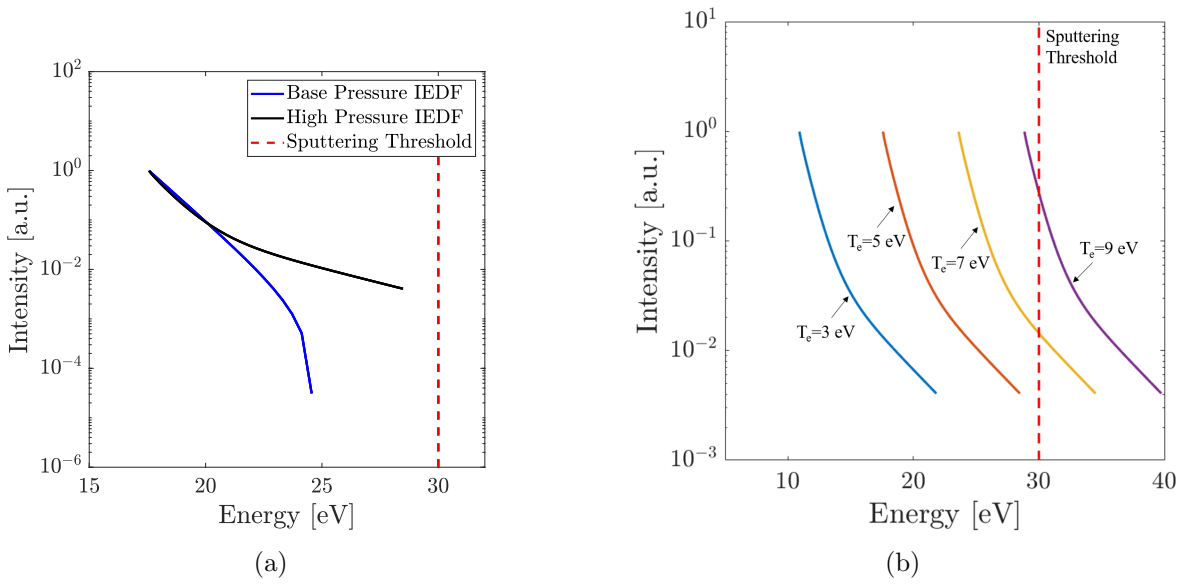

Figure 5.10: (Left) Sheath analysis for Point 6 for the H9 for both the base case as well as high background pressure assuming an electron temperature of 5 eV. (Right) Parametric analysis of the sheath for varying electron temperature for the case with high pressure.

which is then accelerated through a sheath corresponding to an electron temperature of 5 eV (using Eqn. 2.8). This temperature was chosen based on results from the H6MS and HERMeS studies. [20, 176] While the H6MS saw temperatures up to 7.5 eV, the HERMeS results showed a maximum less than 5 eV. Considering the heritage with both thruster and the H9 as well as changes implemented between the H6MS and H9 designs, we believe the measurements from the HERMeS thruster provide a better proxy. The results of this analysis are seen in Fig. 5.10. The majority of the ions remain below the sputtering threshold regardless of pressure. Considering the upper bounds of our measurement, the maximum fraction of ions that could be above the sputtering threshold is 0.4%. Regardless, due to the lack of knowledge of the exact electron temperature, we provide, in Fig. 5.10(b), a parametric analysis of the outer chamber at high pressure with varying electron temperature. The results show that at 7 eV only 4.0% of ions are above the sputtering threshold. It is not until 9 eV that the majority of the ions are above this threshold. Given the realistic electron temperatures are below 5 eV, these results indicate that the pressure

dependence on the erosion rate is very small. This is likely because, despite shifts in the acceleration region, the electron temperature profile in the near-anode region is very flat, resulting in negligible change in erosion with shifts in this profile.

5.5 Conclusions

In this Chapter, we presented the experimental results from our investigation into the impact of neutrals on the performance and shielding of single-channel magnetically shielded Hall thrusters. Section 5.3 showed that regardless of the neutral source, the acceleration region moved inward. However, the response was not linear. It also indicated that neutrals impact the cathode coupling voltage and performance of these thrusters. Section 5.4 also showed that neutrals can influence the near-wall ion behavior which has implications on overall lifetime. A complete discussion of these results, including further analysis of the mechanism behind these effects and ramifications, is provided in Chapter 7.

CHAPTER 6

Impact of Thruster Neutrals from Adjacent Channels on a Magnetically Shielded Nested Hall Thruster

6.1 Introduction

Chapter 5 presented the results from neutral impacts on the performance and lifetime of single-channel magnetically shielded Hall thrusters. Specifically, we focused on neutrals emanating from both the facility background and the cathode. Here, we aim to characterize the impact of neutrals from adjacent channels on nested Hall thrusters. In particular, our goal is to determine whether the theoretical framework presented in Chapter 3 for improved performance accurately represents experimental observations, as well as determine whether neutrals from adjacent channels change the erosion rate of these thrusters. We begin by detailing the test matrix used to complete this study. Then, in Section 6.3 we present results from an experimental campaign on the X2 investigating performance changes. Next, Section 6.4 shows near-wall ion trajectories for the N30 with varying neutral density to assess lifetime changes. Finally, we make concluding remarks for the chapter.

6.2 Test Matrix

In order to complete the studies on nested Hall thruster neutral interactions, we performed two separate experimental campaigns. The techniques and thrusters used were described in Chapter 4. The first investigation examines performance changes in dual channel mode due to changes in neutral density that result from the nested design. [6] For these studies, we operated the X2 Hall thruster in 5 different configurations, detailed in Fig. 6.1. To match

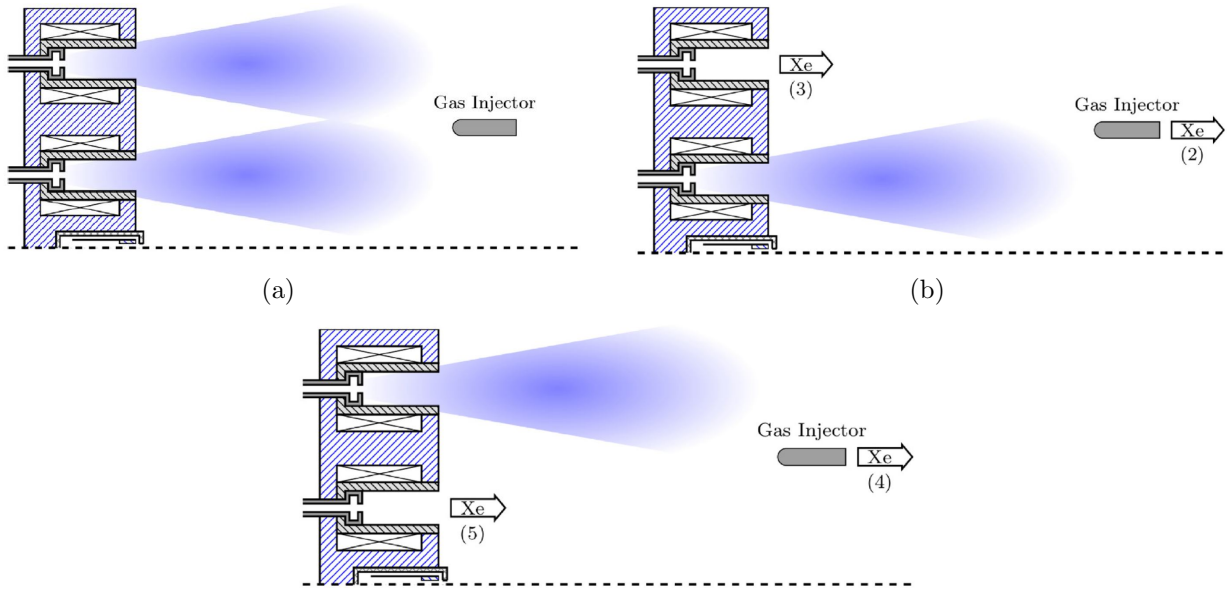

Figure 6.1: Schematic detailing all five operating conditions for the X2 experimental campaign.

the facility background pressure of the multi-channel mode while operating in single-channel mode, xenon gas was injected via a downstream gas injector. To match the background pressure and approximately match the local neutral density profile, gas was injected via the inactive channel (so there was same total gas flow into the chamber as dual channel mode). During these test points, the same flow as dual channel mode was sent to each anode. The five resulting operating conditions are: (1) dual channel operation, (2) inner channel operation with downstream injection (same background pressure as dual channel), (3) inner channel operation with outer channel injection, (4) outer channel operation with

downstream injection, and (5) outer channel operation with inner channel injection. Thus, if the summation conditions (3) and (5) match the dual channel thrust, we will be able to state that the increased performance is due a change in the local neutral density. At each point, we performed the following measurements: thrust stand, near-field Faraday probing (to calculate divergence angle), and LIF. Whenever there was cold gas flowing through the thruster (conditions (3) and (5)), the thrust values were corrected for the thrust from this effect. In addition to this, we mapped the near-field neutral density (as detailed in Chapter 4) to estimate the increased local neutral density in dual channel mode.

The goal of the second experimental campaign was to determine neutral influence on nested thruster erosion. For this campaign, we used the N30 Hall thruster. This was critical as the N30 Hall thruster is magnetically shielded, unlike the X2. In order to quantify these impacts, we operated the inner channel of the N30 alone, as well as the inner channel running with the outer channel nominal propellant flow rate. For all these tests, the thruster was operated at constant power. At each condition, we measured the centerline ion velocity profile to assess whether the bulk plasma shifted inward with higher neutral density in a similar manner to the H9. We then measured the two-dimensional IVDFs near the inner channel chamfers (both inner and outer) to characterize the ion trajectories towards the wall.

6.3 Performance Impacts

We start by discussing the first experimental campaign on the X2 aimed at investigating performance changes between single-channel and dual channel mode. To accomplish this, we begin this section by showing the local neutral profiles for each condition. These measurements show that there are differences in the local neutral profile between the operational modes and we should expect changes in thruster behavior due these changes. We then

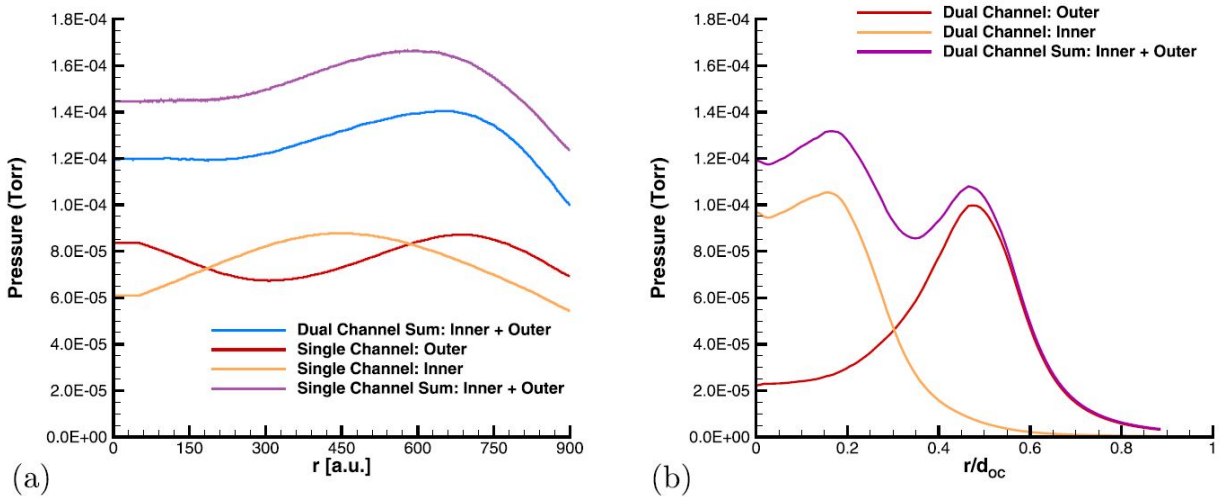

Figure 6.2: Neutral profiles for all conditions of the X2 testing from (a) experiments and (b) simulations. Reproduced from Cusson et al. [6].

present the thrust, divergence angle, and acceleration region measurements.

6.3.1 Local Neutral Profile

Results from Fig. 6.2a from radially sweeping a Stabil-Ion Gauge in front of the X2 thruster. This mapping was performed after the hot fire testing, thus the exact same flow rates used during plasma measurements were used for this cold flow mapping. The results indicate that with a base pressure of 0.5 μTorr-Xe, the maximum pressure in dual-channel mode at axial location z=0.35 d_{OC} from the exit plane is 140 μ Torr-Xe, while the maximum pressure with downstream injection is 87 μTorr-Xe for both the inner and outer channels. The pressure profile for dual-channel mode qualitatively matches the sum of the single-channel modes because the same flow is being injected into the chamber in the same locations. The magnitude of the total flow into the chamber when summing the two profiles is higher than dual-channel mode because of two effects that are included twice: the cathode flow and the background pressure. The cathode flow is added twice because the center-mounted cathode is shared between the two channels. The background pressure is added twice, because in both single-channel cases we are matching the same background pressure by additional

neutral injection; however, this effect is smaller by an order of magnitude than that of the cathode flow. Since this measurement does not account for ionization, these results cannot definitively confirm the validity of this technique. However, they suggest that pressure from single-channel modes can be approximately summed to compare to dual channel values. These data show that neutral density near the thruster is much higher in dual-channel mode than in any of the two single-channel modes even when the background pressure is the same.

Assuming that the xenon neutrals are at 300K (no plasma present to heat the neutrals), the density of the inner channel neutrals diffusing to the outer channel centerline is calculated to be 5.7×10^{17} m^3, while the density of the outer channel neutrals diffusing to the inner channel centerline is 1.2×10^{18} m^3. The typical ionization fraction in Hall thrusters is approximately 15%; [56] therefore, the neutral density near the channel would only be 85% of the calculated density. Note here that the ionization fraction is the ratio of the ion particle density to the total particle density. Despite this low ionization fraction of 15%, Hall thrusters still exhibit a mass utilization of around 95%. This disparity is due to the large disparity between the ion and neutral velocities. More details on the simulation can be found in Reference [168]. The simulations confirmed that neutrals from adjacent channels can diffuse to the channel of interest. Thus, these neutrals have the potential to induced changes in thruster behavior such as acceleration region location and total thrust. These values will be used in Chapter 7 to predict dual-channel thrust based on the theory outlined in Chapter 3.

6.3.2 Performance

The thrust for each test point is shown in Table 6.1. During the experiment, the thrust data had a one hertz low amplitude oscillation superimposed on the data due to PID tuning. This oscillation was filtered out during data post-processing. The table includes the test

Table 6.1: Thrust results at all test points and injection location for reference.

Test point	Channels operating	Thrust [mN]	Power [kW]	Injection location
1	Dual Channel	357.0 ± 4.5	4.46 ± 0.08	N/A
2	Inner Channel	92.7 ± 2.7	1.26 ± 0.05	Downstream
3	Inner Channel	94.5 ± 3.0	1.27 ± 0.05	Outer Channel
4	Outer Channel	248.1 ± 3.3	3.26 ± 0.08	Downstream
5	Outer Channel	264.8 ± 3.6	3.24 ± 0.07	Inner Channel
2 + 4	Summation downstream	340.8 ± 4.3	4.52 ± 0.09	Downstream
3 + 5	Summation channel injection	358.9 ± 4.7	4.51 ± 0.09	Channels

condition, the resulting channels operating, thrust, power, and the location of gas injection (if applicable). The table also includes the summation of inner and outer channels with downstream injection and channel injection for comparison to dual channel results. The results show that the thrust in dual channel mode (357.8 mN) is 17 mN higher than the thrust resulting from the summation of single-channel operation (340.8 mN) when operating at the same background pressure. This 17 mN corresponds to a 5% increase in thrust. However, when the pressure is matched via channel injection, this discrepancy is eliminated within the uncertainty of the measurement (total thrust is 358.9 mN). This suggests that the presence of more neutrals in the vicinity of the thruster is resulting in higher thrust. In order to compare the three cases, we can predict dual channel operation for both single-channel combinations using Equations 3.3 - 3.11. The results of this calculation are shown in Table 6.2. A similar trend is observed in the effective efficiency and specific impulse as with the thrust. The results show that when the pressure is controlled via downstream injection, the efficiency and specific impulse of the thruster is lower than in dual channel mode; however, when the local neutral density is matched with channel injection, the performance is nearly identical to dual channel mode. This indicates that the increased neutral density near the thruster is causing the increase in performance. However, it does not reveal the mechanism

Table 6.2: Effective anode efficiency, specific impulse, and total thrust for single-channel modes versus dual channel mode.

Test point	(Effective) η_a	(Effective) $I_{sp,a}$ (s)	Thrust (mN)	Note
1 (Dual Channel)	0.47 ± 0.01	1196 ± 14	357 ± 4.5	Measured
2 + 4 (Downstream)	0.42 ± 0.02	1141 ± 33	340.8 ± 4.3	Calculated
3 + 5 (Channel)	0.47 ± 0.03	1204 ± 36	358.9 ± 4.7	Calculated

by which this occurs. Thus, we must look at the divergence angle and neutral ingestion to determine this mechanism.

6.3.3 Divergence Angle

An example of the Faraday probe data is shown in Fig. 6.3. The calculated divergence angle as a function of axial location is shown in Fig. 6.4. These measurements indicate that the divergence angle in dual channel mode is consistently lower than single-channel mode when facility pressure is matched. Furthermore, when the local neutral density profile is approximately matched through channel injection, the ion beam diverges less than during downstream injection. During channel injection, the ion beam divergence of the outer channel matches, within uncertainty, the divergence of the outer channel in dual channel mode. This suggests that matching local pressure better predicts dual channel divergence. For the inner channel, the very-near-field dual channel and channel injection divergence angles do not match. In dual channel operation, the cathode plasma is significantly denser due to the increased current and flow rate required for operation. This in turn could reduce the cathode to inner channel plasma density gradient resulting in a lower divergence in the near-field, as suggested by Hofer. [64] However, they still evolve to the same value below that of the downstream injection divergence angle.

Using Eqn. 3.16, the beam currents are calculated and shown in Table III. From Table II,

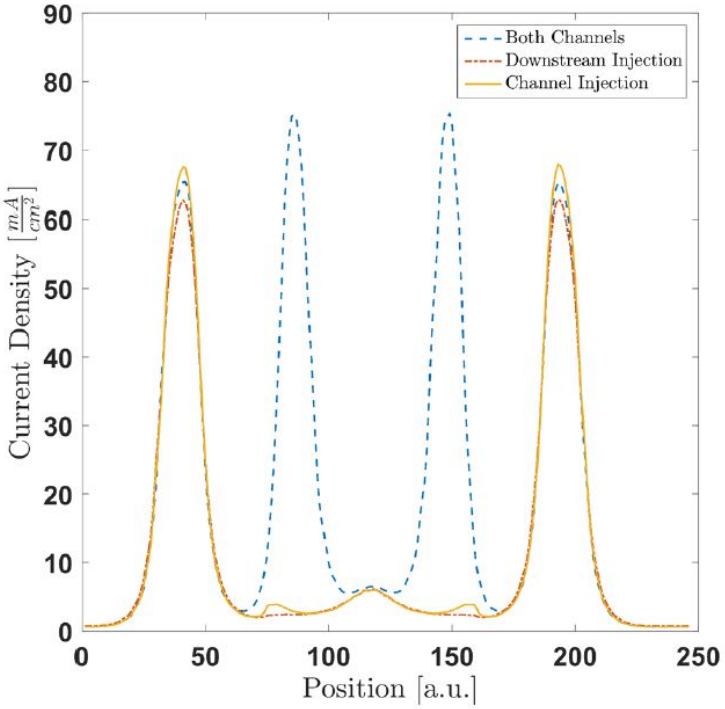

Figure 6.3: Example current density trace showing the outer channel for all three cases (dual, downstream injection, and inner channel injection). Reproduced from Cusson et al. [6]

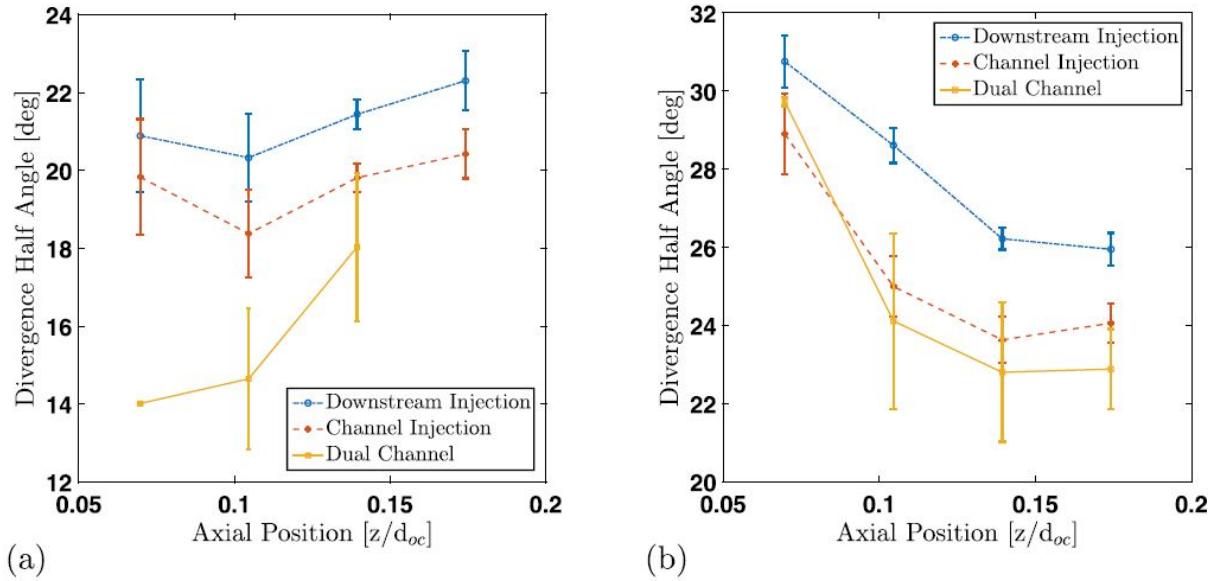

Figure 6.4: Divergence angle as a function of downstream position. (a) Inner channel divergence angle as a function of downstream position. (b) Outer channel divergence angle as a function of downstream position. Reproduced from Cusson et al. [6] Uncertainty is calculated as the standard deviation of multiple measurements.

Table 6.3: Beam current values for high power operation.

Test point	Test condition	Beam Current (A)
2	Inner channel w/downstream injection	7.63±0.08
3	Inner channel w/channel injection	7.74±0.04
4	Outer channel w/downstream injection	20.24±0.10
5	Outer channel w/channel injection	20.77±0.01
1	Dual channel	28.35±0.31
3+5	Channel injection summation	28.51±0.05
2+4	Downstream injection summation	27.87±0.13

Table 6.4: Divergence efficiency for the single-channel modes versus the dual channel mode.

Test condition	Divergence efficiency
1 (Dual channel)	0.872±0.001
2+4 (Downstream injection)	0.840±0.001
3+5 (Channel injection)	0.864±0.004

the thrust in dual channel mode is 17mN greater than the sum of the single channels with downstream injection. Using the beam current and Eqn. 3.15, the divergence efficiency is calculated and can be seen in Table 6.4. In Chapter 7, we will use the calculated beam current and divergence efficiencies to attempt to explain the thrust in dual channel mode based on single-channel operation while accounting for neutral impacts. The final piece of information we need to enable this calculation is the exit velocity, which we obtain from LIF measurements.

6.3.4 Laser-Induced Fluorescence

Figure 6.5 shows the mean ion beam velocity as a function of position for both the inner channel and outer channel. A distinct shift and compression of the acceleration region is observed when the local pressure is matched using channel injection. Lastly, the exit

velocities at 12 mm downstream of the exit plane for the dual channel and channel injection conditions are greater than during downstream gas injection. For the outer channel, the exit velocity for dual channel mode is 12.5 km/s, for single-channel with no inner flow is 11.7 km/s, and for single-channel with inner channel gas flowing is 12.4 km/s. For the inner channel, these values are 12.3 km/s, 11.7 km/s, and 12.1 km/s respectively. It appears that the neutral density from the adjacent channel is not only shifting the acceleration region inwards, but also increasing the voltage utilization, yielding higher exit velocities. In other words, due to a lower divergence, less of the voltage is being used from radial acceleration and it is more concentrated on axial acceleration (the critical direction for thrust production).

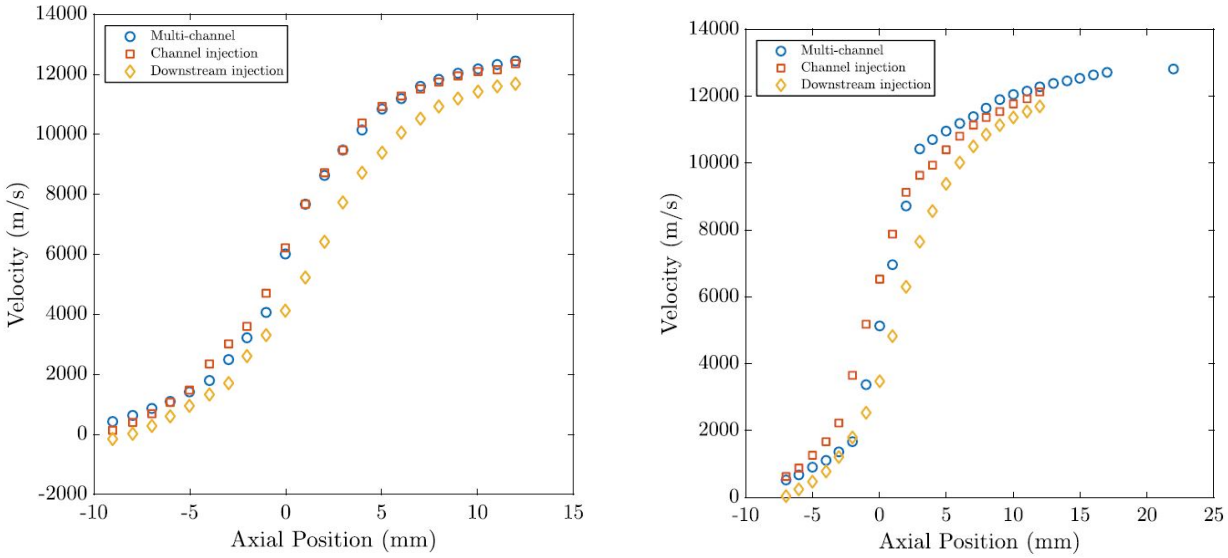

Figure 6.5: Comparison of ion beam velocity curves for each condition along the outer channel (a) and inner channel (b). Position 0 is the exit plane of the X2. Reproduced from Cusson et al. [6].

6.4 Lifetime Impacts

Having previously established that channel injection is a valid technique for examining the impact of neutrals from adjacent channels, our second experimental investigation aims to

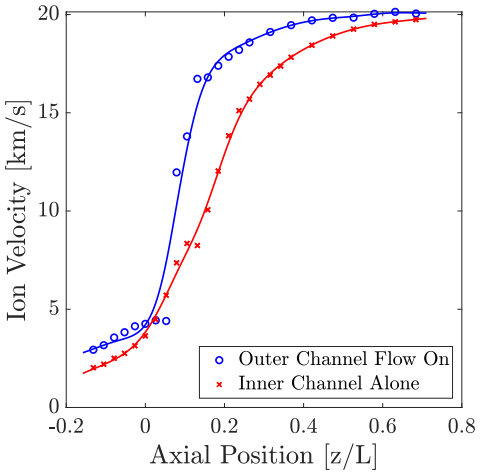

Figure 6.6: Mean ion velocity along the centerline of the inner channel of the N30 both alone and with the outer flow on.

analyze the near wall ion velocity vectors on the inner channel alone and with outer flow. Based on our results from the X2 showing the acceleration region shifting and compressing inwards with the addition of the outer channel flow, we might expect a change in temperature of the grazing line for magnetically shielded NHTs. As a reminder, we use the N30 Hall thruster for this investigation. First, we will present the centerline profile to indicate that the profile is changing and shifting, and then move on to chamfer results.

Figure 6.6 shows the data, as well as fitted splines, for each condition of the N30 study. Similar to results seen on the H9 (shown in Section 5.3), the plasma shifts axially inward when the outer channel flow is turned on. The magnitude of this shift is larger than the shift for the H9 with pressure. This is expected, as the neutral density emanating from the outer channel is much larger than increases in neutral density due to background pressure changes. Notably, it appears that in addition to a shift, the acceleration region also compresses (changes shape) with the introduction of neutrals from the outer channel. Studies on the X2 (presented in Section 6.3.4) showed similar results for the inner channel. For the N30, the oscillation strength increased significantly from 69.8% to 101.8% peak-to-peak of the mean current

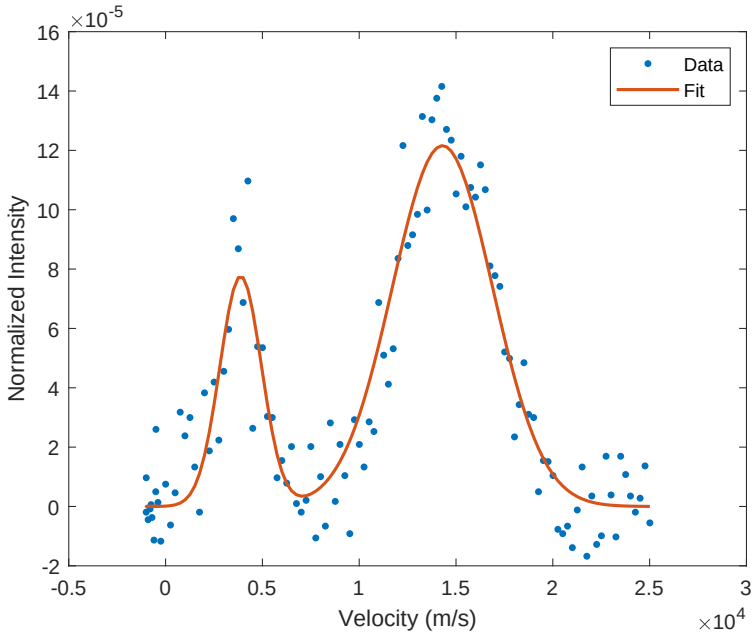

Figure 6.7: Example IVDF trace midway through the acceleration region showing evidence of a bimodal distribution.

with the introduction of outer channel flow. Oscillations are known to widen measured velocity distributions or form bimodal distributions which could lead to this change in the acceleration region shape. [26,177] Figure 6.7 shows an example of the IVDF midway through the acceleration region showing an example of a bimodal distribution observed when the outer flow was turned on.

As such, when the oscillations are large, the measured profile does not reflect the instantaneous shape but rather the time averaged shaped. Finally, due to the increase in oscillation strength, the signal-to-noise ratio decreased significantly. This could be a contributing factor to the data shown in Fig. 6.6.

Next, we look at the chamfers for the N30 inner channel. The two-dimensional vector plots for both the inner and outer chamfers are seen in Fig. 6.8. Unfortunately, due to signal-to-noise issues during the outer flow measurements, we were unable to resolve

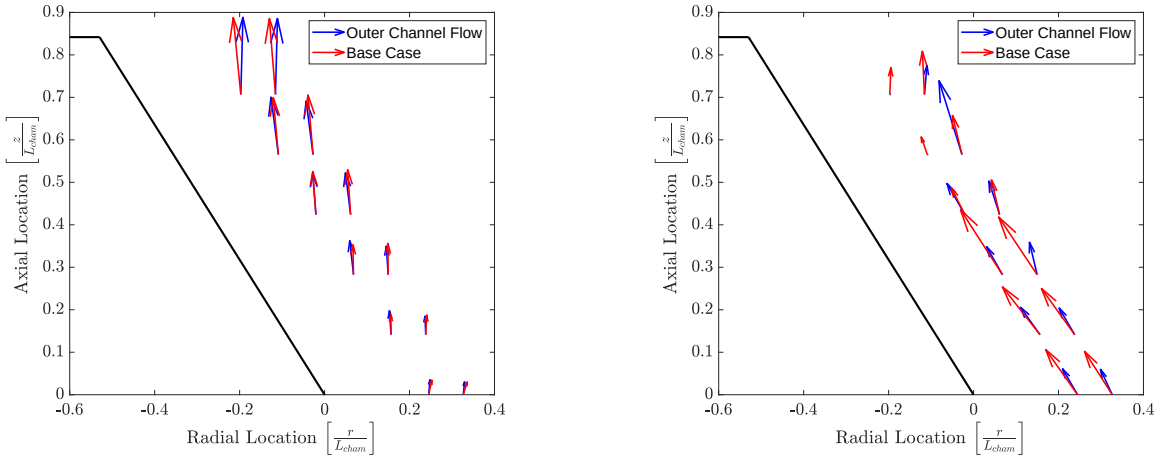

Figure 6.8: Ion velocity vectors for both the base pressure case and the high pressure case along the inner (a) and outer (b) wall of the NHT-60.

points 5 and 6 for the outer chamfer (a schematic of the experiment is shown in Chapter 4). Overall, we see that there does not appear to be any major changes in the velocity vector in the near field of the wall. The outer wall does seem to show that the average parallel velocity is lower when flowing through the outer channel than when just firing the inner channel. This suggests that despite bulk motion of the centerline plasma, there does not appear to be major changes that would yield erosion causing ions in the near-wall region.

Next, we look at the actual VDFs and the corresponding sheath analysis using Eqn. 2.8 and the same procedure followed in Chapter 5. Due to the missing data at point 6, and based on the results shown in Fig. 6.9, we chose to analyze point 1 for the N30 for the outer wall. Fig. 6.9 shows that point 1 on the outer wall appears to have the widest VDF in negative velocity space for the N30. The results of the sheath analysis are seen in Figure 6.10. Surprisingly, there does not appear to be a significant difference between the two traces. This could be indicative that due to changes in the plasma behavior (for instance, oscillations), another process is affecting the near wall ion trajectories. Combined, these measurements indicate that the lifetime of the thruster does not appear to depend on the

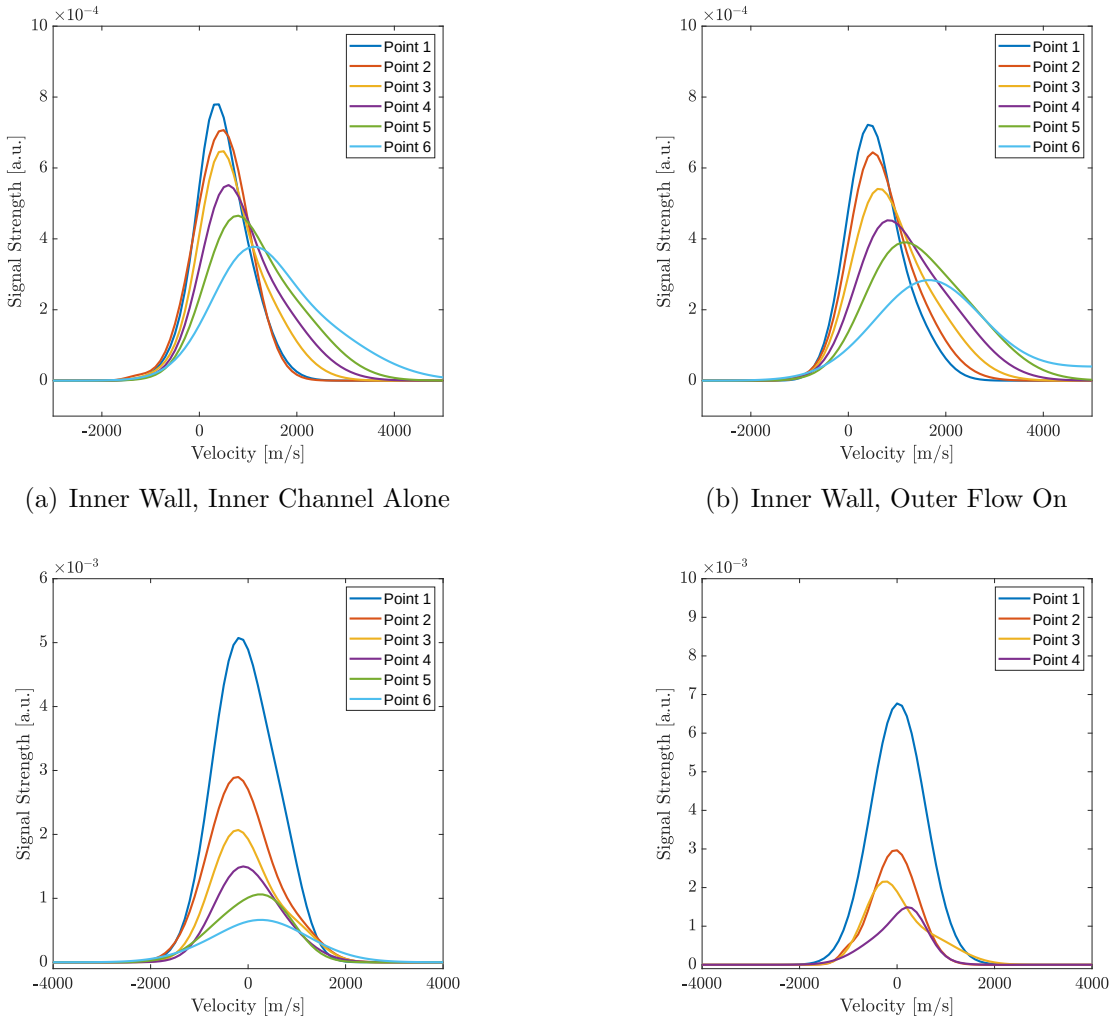

(a) Inner Wall, Inner Channel Alone

(b) Inner Wall, Outer Flow On

(c) Outer Wall, Inner Channel Alone

(d) Outer Wall, Outer Flow On

Figure 6.9: Perpendicular VDFs along the inner channel wall for both the inner channel alone (a) and the inner channel with outer flow on (b) as well as alone the outer wall for the inner channel alone (c) and the inner channel with outer flow on (d).

near-field neutral profile. However, it is important to determine the sensitivity of this analysis to the wall electron temperature as we did not assess this here. Figure 6.10(b) shows a parameter analysis for varying electron temperature of the sheath analysis on the outer wall case with outer channel flow. While this will be discussed more in Chapter 7, based on wall temperature measurements of the H6MS and the HERMeS Hall thrusters, a

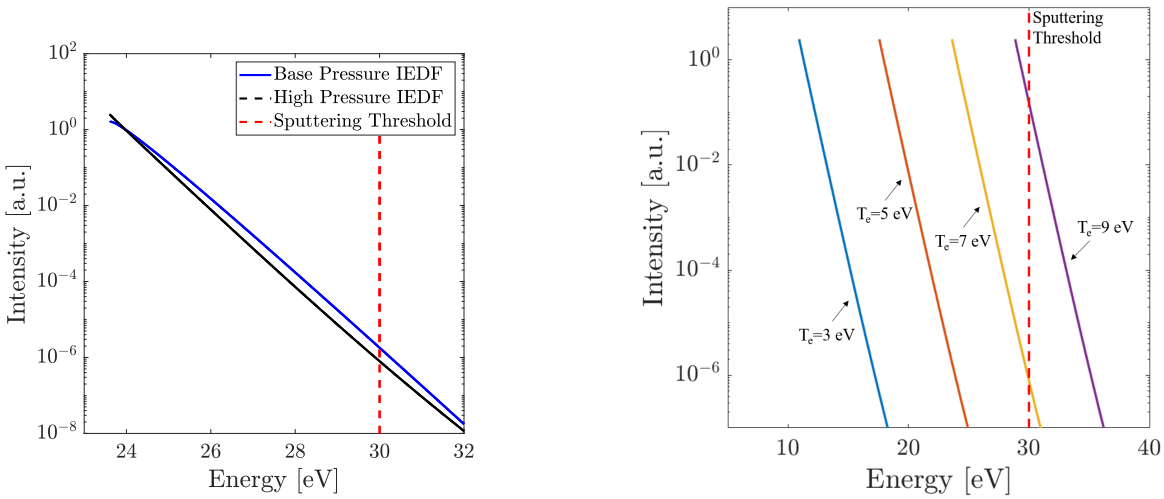

Figure 6.10: (Left) Sheath analysis for Point 1 for the N30 for both the base case as well as with outer channel flow on assuming an electron temperature of 7 eV. (Right) Parametric analysis of the sheath for varying electron temperature for the case of the inner channel with outer flow on.

realistic peak electron temperature is less than 5 eV. Thus, the entirety of the IEDF likely remains below the sputtering threshold for all cases examined here.

6.5 Conclusions

In this chapter, we presented the experimental results from our investigation of neutral impacts on the performance and lifetime of nested Hall thrusters. First, we showed that the thrust, divergence, beam current, and ion exit velocity changed for the X2 between single-channel and dual channel mode. However, when the neutral flow from the other channel was on, many of these parameters returned to the dual channel value. Combined, the dual-channel and single-channel with adjacent channel flow measurements indicate that the changes between single-channel and dual channel operation are driven by the local neutral density. Next, we investigated the impact of outer channel neutrals on the inner channel lifetime of the N30. Results showed that there does not appear to be a large change in the near-wall behavior with these changing conditions. These results, and their implications on

our understanding of nested Hall thruster performance, will be discussed in Chapter 7.

CHAPTER 7

Discussion

7.1 Introduction

In this chapter, we discuss the results shown in Chapters 5 and 6 and their implications. In particular, we start by examining the results from the H9. We assess performance and lifetime changes with neutral density from the background and cathode. We focus on analyzing these results "blind" to the source of the neutrals and simply based on the resulting increase in neutral density near the face of the thruster. This illuminates potential ways to better predict the performance of these thrusters based on local neutral density. Next, we move on to evaluating the results from our nested Hall thruster studies. Namely, we predict the thrust in multi-channel operation based on single-channel results and changes in neutral density. Finally, we briefly discuss the lifetime studies and why there were no major changes in near-wall ion behavior for the N30.

7.2 Single-Channel Hall Thrusters

Overall, our results presented in Chapter 5 for the H9 showed that magnetically-shielded Hall thrusters are susceptible to changes in operation due to neutrals emanating from the background and the cathode. Here, we present an explanation for the behavior and its potential implications. We begin with the acceleration region, performance, and cathode coupling behavior before moving on to a discussion of the implications on thruster lifetime.

Chapter 5 showed that the acceleration region shifted inward with increasing neutrals from both the background and the cathode. We propose a hypothesis that may explain this set of data: the thruster is agnostic to neutral source and is simply responding to the increase in neutral density. In order to quantify this hypothesis, we aim to correlate the location of the acceleration region with the change in neutral density. First, we model the changes in neutral density due to background pressure using the ideal gas law. We assume that the neutrals are thermalized to room temperature and calculate the neutral density using the measured pressure. We then subtract off the base condition in order to get the change in neutral density. The base condition is operation with 7% cathode flow fraction and the lowest background pressure. We assume that this change is uniform throughout the vacuum chamber. We follow a similar procedure for changing cathode flow fraction; however, instead of assuming a uniform change throughout the facility, we assume hemi-spherical diffusive expansion from the cathode. We take the value on channel centerline and subtract the base case to estimate the change in neutral density from this effect. Finally, we plot the change in neutral density on channel centerline versus acceleration region location (calculation of location detailed in Chapter 4).

The results of this calculation are shown in Figure 7.1 for all of the different sources of neutral density. For modest changes in neutral density (up to about 4×10^{17} m^{-3}), we see an approximately linear inward trend versus changing neutral density. Once a sufficiently high change in neutral density is achieved, the trend begins to asymptote. This suggests that a similar change in neutral density yields a predictable shift in the acceleration region location. This is an encouraging and profound result as it suggests that it is not the source of neutrals but the mere presence that is correlated with this movement. Taken in this light, this correlation can help explain why our mitigation study with cathode flow fraction was unable to make the externally fed system impervious to facility effects. Even by increasing

the external cathode flow fraction to 15% for the external cathode, we are not able to reach a sufficient neutral density to saturate the effect. Thus, we would need to increase this density even further for the external cathode to not cause shifts in the acceleration region. These data, in combination with the thrust measurements shown in Chapter 5 indicate that the thruster is indeed source agnostic and the critical parameter is the change in neutral density at the thruster exit. Thus, increasing the neutral density via the cathode makes the thruster less susceptible to facility neutrals, as the "saturation" density has either already been achieved or is proximal. Therefore, the near-field must simply be "saturated" with sufficient neutrals to enable constant thruster performance. This is a critical piece in illuminating a reason why the acceleration region moves. Recently, Mikellides et al [178] suggested that thrust enhancement due to background pressure increases is correlated with charge-exchange collisions between beam ions and background atoms. This supports the conclusion that neutral density at the exit plane is the driving parameter. The study also noted that acceleration region movements and cathode coupling were critical. [178] We elaborate on the importance of cathode coupling below.

It is important to note that Nakles and Hargus previously showed increasing background pressure led to shifts in the acceleration region for an externally mounted cathode. [26] They also suggested that this could lead to changes in performance. However, their study was limited in scope to pressures between 10 and 30 μTorr-Xe. Thruster behavior is known to continue to change below these pressure levels. [94] Additionally, the study did not directly measure any performance data in conjunction with the acceleration region measurements. Regardless, our results here are consistent with theirs, showing that there is an upstream shift in the acceleration region with increasing background pressure. As previously demonstrated by Hofer et al., we also show that the external cathode is more susceptible to these effects than the internal cathode. [28, 64] Most critically, for both cathode positions, we show that the acceleration region of the thruster moves axially

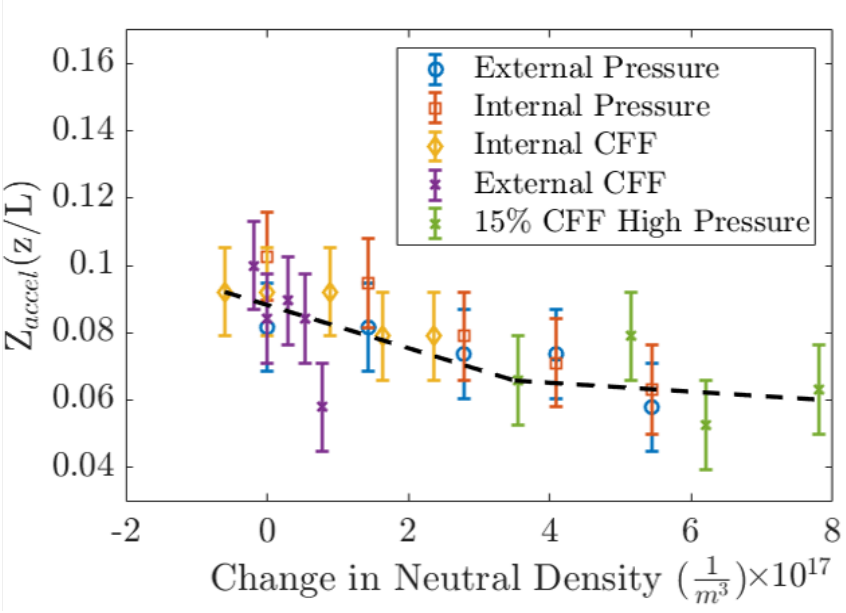

Figure 7.1: Acceleration region location versus change in neutral density on channel centerline for the H9. "External/Internal Pressure" indicates the conditions in which the pressure was varied at 7% cathode flow fraction. Similarly, "External/Internal CFF" indicate the conditions during which the cathode flow fraction was varied. "15% CFF High Pressure" indicates the four conditions during which either cathode was operated at 15% cathode flow fraction and elevated background pressure. The black dashed line represents general trends.

and correlates these measurements with performance, the key parameter for many flight operators. Additionally, we show that by increasing the neutral flow in the cathode region, we are able to reduce the susceptibility of the thruster to facility effects. This is important for a few reasons: (1) it confirms that the internal and external cathodes have similar behavior with regards to acceleration region shifts versus neutral density changes, (2) these shifts lead to a measurable change in thrust, and (3) the critical parameter is neutrals in the exit plane and the source of said neutrals is not important. While the results showed that we could not completely saturate the near field for the external cathode, we believe that this is because the same magnitude of neutral density changes were not achievable with this cathode. If more neutrals were injected in this region (e.g. even higher than 15% cathode flow fraction), the results suggest that we would be able to saturate this effect and thus make the thruster impervious to facility neutrals. Because the internal cathode

delivers neutrals more efficiently, the shifts in the acceleration region are small, and the effect saturates faster thus allowing more constant performance for these cathodes.

In Chapter 6, we noted that transitioning from ground to flight was a risk for operators. However, because we have showed that the thruster only needs an increased neutral density at the exit plane, and that these neutrals can be sourced anywhere, there exists a potential solution. On-orbit thrusters could mitigate outward shifts in the acceleration region and lower performance due to the lack of background neutrals by increasing the cathode flow fraction. However, increasing the cathode flow fraction is known to reduce the cathode lifetime due to increased pressures in the insert region. [8] Since the results show that this region is not critical to the effect, a solution to this problem is to inject the additional neutrals via the cathode-keeper gap, similar to what high-current cathodes do to prevent high-energy ions. [179, 180] With this technique, an increased neutral density could be achieved at the thruster exit plane without sacrificing cathode lifetime.

We would be remiss to not also discuss the changes in cathode coupling voltage. Our results showed no obvious trend linking acceleration region location to coupling voltage. In fact, we observed opposite trends for the coupling voltage with different sources of neutrals. As briefly discussed in Chapter 5, we believe this is because when running in constant power mode, as the facility pressure increases, the cathode flow must slightly decrease. As the near field plume is dominated in neutral density by the cathode neutrals, lower neutral density would lead to higher coupling voltages. This is likely because as the neutral density decreases, electron-neutral collisions, as well as other processes for transport that depend on neutral density (such as ion acoustic turbulence), decrease. Thus, the mobility of electrons to travel from the cathode to the thruster plume decreases, driving up the plamsa potential and coupling voltage.

Indeed the recent studies from Mikellides et al [178] and Lopez-Ortega et al [181] suggest that as the neutral density is increased in the cathode plume, there is enhanced centerline ion acceleration due to a decrease in the near-plume potential resulting in higher thrust. They suggest, and detail corroborating simulations, that as the neutral density decreases in the cathode plume, the plasma potential in the near cathode region also decreases. This decrease in near-plume potential allows electrons to travel along magnetic field to the thruster plume more easily. Additionally, particularly for external cathode, azimuthal asymmetries are very important in this process. This again leads to the conclusion that external cathode would be more susceptible to these effects. Finally, because this drop in potential is logarithmic with plasma density (Boltzmann's relation), we would expect the response of this effect to be non-linear. Regardless, the changes in cathode coupling voltage are small compared to overall acceleration voltages. Indeed, comparing these voltage changes to the acceleration voltage drop due to a 300 V bias, we see that these changes are less than 2% (within the uncertainty of most measurements). Therefore, we do not believe that the change in cathode coupling voltage is a dominant contributor to the improved performance.

Overall, we see that neutrals have the ability to impact the acceleration region location of Hall thrusters, which then leads to changes in thrust. Now, we consider the lifetime of these thruster and how these changes in acceleration region may impact this. In Chapter 5, we showed the results of changing the local neutral density on the shielding of magnetically shielded Hall thrusters. In general, we find that the impacts are small and likely do not strongly influence the lifetime of the thruster. The study on the H9 tells us that higher pressures could lead to slightly higher erosion rates if the electron temperature were sufficiently high near the wall. However, based on expected temperatures (informed by other thrusters), we do not believe this electron temperature to be sufficiently high, and we do not believe there is an appreciable change to the erosion. Further, shifts in the

centerline profile would actually correlate to a longer lifetime in space than on the ground as pressure decreases between the two locations. If the plasma is moved downstream, like we would expect in flight, the grazing magnetic field line may be sampling even colder plasma and have a potential even closer to that of the anode. This typically leads to higher divergence, which could alter the trajectories beyond the measurements we presented here. This is important for other thruster parameters, such as performance and pole erosion, as well as spacecraft interactions. The ion trajectories are not changing substantially, and an electron temperature significantly greater than the expected value (>7 eV) would be required to accelerate a larger portion of the ions to above the sputtering threshold. We did not attempt to characterize this temperature during this study; however, based on our results, we do not believe this temperature is changing significantly. Because the ion trajectories, as well as the magnitude of the mean velocity in each direction, does not change substantially between condition, we argue that this implies there are no substantial changes to the electron temperature of the grazing line. Still, a dedicated study to measure changes in this temperature versus pressure is warranted.

Earlier, we suggested that the location of the acceleration region can be "controlled" by varying the neutral density in the near-field of the thruster. However, there did exist a risk for magnetically shielded thrusters that this would lead to higher erosion if the location was not precisely controlled. However, these data indicate that this is not a large concern as theses shifts in the plasma location here did not drastically alter the ion flux to the wall.

7.3 Nested Hall Thrusters

In Chapter 6, we presented data for the X2 showing improved performance in dual channel mode as compared to the summation of single channel modes. In addition, we measured parameters such as the acceleration region location, divergence angle, and near-field pressure

to quantify how these parameters change between the two conditions. Here, we use these quantities to attempt to "calculate" the thrust in dual channel mode based on single-channel results and our theory for neutral impacts from Chapter 3. We also measured the near wall behavior of the N30 and showed that there was no appreciable difference due to outer channel flow. Here, we discuss why we believe this result was seen.

7.3.1 Mechanism for improved performance

As a reminder, we proposed an expression for thrust in dual-channel mode for a two-channel thruster that would be,

$$F_{th} = F_{inner} + F_{outer} + F_{div} + F_{ing}, \tag{7.1}$$

where F_{inner} is the inner channel thrust measured alone, F_{outer} is the outer channel thrust measured alone, F_{div} is the thrust gained from divergence reductions, and F_{ing} is the thrust gained from ingestion of adjacent channel neutrals. We measured the dual channel thrust to be 357.0 ± 4.5 mN. When simply summing the two channels in single channel mode (at equal background pressure), we calculated a total thrust of 340.8 ± 4.3 mN. This 16.2 mN difference is what we aim to explain. It is important to note that when we measured the thrust of each individual channel operating alone (with the flow of the adjacent channel on) and summed them together, 358.9 ± 4.7 mN of thrust was produced. Thus, simply by replicating the neutral environment, the thrust was recovered. Therefore, we believe this increase in thrust is rooted in the presence of additional neutrals and their effects on the plasma state, not another plasma-derived phenomenon. In order to calculate the increase in thrust due to reduced beam divergence, we use the tabulated divergence efficiencies shown in Table 6.4 and Eqn. 3.23. We measured values for the change in divergence which we got by running individual channels and flowing gas through the adjoining. These changes are factored into term F_{div}. We have also estimated the ingested mass flow and thrust from

increased neutrals from the adjoining channel. This is based on Eqn. 3.14 and impacts F_{ing}. We should note that when channel ingestion was done, we kept the channel at constant power. Combining these, it can be seen that going from single channel to dual channel mode would result in an 8.7 ± 1.2 mN increase in thrust. Based on this result, we see that changes in divergence accounts for a significant portion of the improvement in thrust during dual channel operation.

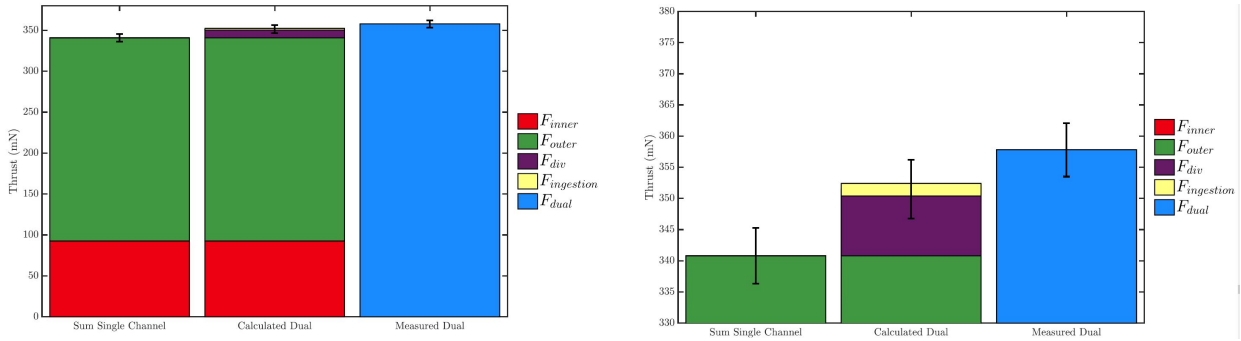

(a) (b)

Figure 7.2: Comparison of the sum of individual channel thrusts, the calculated dual channel thrust, and the measured dual channel thrust shows that the calculated value based on divergence and neutral ingestion models predicts the actual value within uncertainty. The left figure shows the full scale while the right shows a zoomed scale to visualize differences.

Similarly, we use the ion exit velocity, measured neutral density, Eqn. 3.14, and an ionization probability of 15% to calculate the thrust due to neutral ingestion. This estimated improvement was computed to be 2.0 +0/-0.2 mN. Combining the two measurements, the expected increase in thrust due to both neutral ingestion and divergence angle changes is calculated to be 10.7 ± 1.3 mN. As seen in Fig. 7.2, these calculated increases account for the measured increase within uncertainty. The total calculated dual channel thrust is 351.5 ± 4.4 mN. Of critical importance is that, based on the theory described in Chapter 3, the dual channel thrust and performance were accurately explained by neutral ingestion and divergence within the uncertainty. In particular, divergence changes drove the majority of the improved performance. This result suggests that local neutral ingestion and divergence

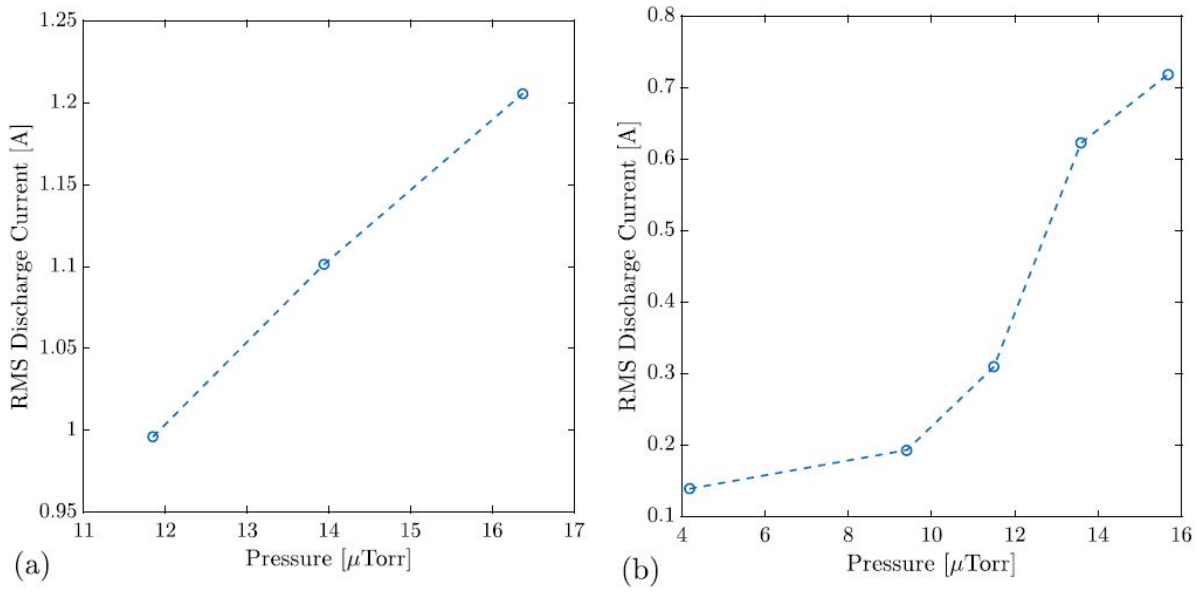

Figure 7.3: RMS discharge current oscillations for the inner and outer channels of the X2. (a) RMS of the outer channel discharge current as a function of facility background pressure. Gas is injected via the inactive channel. (b) RMS of the inner channel discharge current as a function of facility background pressure. Gas is injected via the inactive channel. Reproduced from Cusson et al. [6]

angle are the dominant second order processes affecting nested Hall thruster performance. However, there are still other processes that could affect the performance to a lesser extent, such as plasma oscillations or cathode pressure gradients.

To further discuss other potential processes, we look at the oscillatory behavior of the X2. Hall thruster discharges generally sustain low frequency, 10 kHz to 1MHz, oscillations and the literature has shown that they can affect thruster performance. [182–187] Whether these oscillations improve or diminish thruster performance is still an active area of research. [183] Figure 7.3 shows that the oscillation strength (RMS) versus background pressure (neutral density) for each channel of the X2 during this experiment. In these figures, we see that discharge oscillations increased monotonically with pressure, an effect that has been previously observed. [22] For typical Hall thruster discharge current oscillations, the statistical relationship, $I_{P2P} \approx 6I_{rms}$, can be used as an estimate of the average peak-to-peak.

Using this approximation to estimate the peak-to-peak oscillations during this experiment, we find that $I_{P2P} \approx 0.51 I_{DC}$ for the inner channel, and $I_{P2P} \approx 0.34 I_{DC}$ for the outer. For reference, peak-to-peak discharge oscillations have been directly measured to exceed 100% of the mean current for other thrusters. [22] Since the literature is divided in its conclusions, we neglected any contribution to the thrust due to discharge oscillations in our calculations. However, if the change in discharge oscillations between single and multi-channel modes were large, then this may be an additional process that affects the thrust from a NHT.

Considering the above results, in combination with the N30 oscillation strength with and without the outer channel flow, we see that nested Hall thrusters generally have larger oscillations with higher neutral density. Therefore, while there may be improved performance in multi-channel operation, there appears to less stability. This is an important consideration for the transition to flight as there is a desire to ensure thruster stability on orbit. However, we do note that all these studies occurred at a constant magnetic field strength. We may be able to recover the same stability in dual channel mode by varying the magnetic field.

Overall, we have developed the following physical picture for neutral impacts on the performance of nested Hall thrusters: neutrals from the adjacent channel enhance performance due to reduced divergence and neutral ingestion. Neutral ingestion only leads to a small increase in performance likely for two reasons: only a small fraction of the ingested neutrals are ionized and they may be born partially through the acceleration region leading to less thrust production. However, neutral from the adjacent channel cause the acceleration region to shift inward and compress. This movement reduces the divergence angle of the channel and leads to more axial production of thrust. Based on this informed physical picture, we can predict dual channel performance from single channel measurements. However, more research is necessary to understand why the acceleration region moves and how parameters such as oscillations fit into this picture.

7.3.2 Lifetime

The final consideration for this investigation is the impact of outer channel neutrals on the lifetime of the inner channel of a magnetically shielded Hall thruster. Chapter 6 showed the near-wall ion trajectories and IVDFs for the inner channel walls of the N30. The results showed that we do not see a significant difference in the IEDF or the ion trajectories with the addition of the outer channel flow. We do note that the lack of data near the exit plane does present an incomplete picture, with the possibility of increased erosion at this position. We believe the large change in oscillatory behavior between the two cases is the reason for both the small signal-to-noise ratio for the outer flow case and the lack of a clear trend for the LIF study. Ideally, this study would be repeated with the outer channel plasma on, as without the plasma, the neutral density is higher than would be expected in dual-channel mode. This may have contributed to change in oscillation behavior. Alternatively, we consider that the acceleration region did not actually shift and was instead just compressed, as the results suggested. If this was true, while the downstream ion velocity profile (as well as potential and electron temperature) profiles would change, the upstream profile would not change. Thus, the grazing line would be intersecting the centerline at the same electron temperature in both cases and high potential would be maintained along the wall in all cases. This would suggest that no change in ion wall trajectories would be expected as the results show. Overall, this study indicates that the erosion profile of the thruster is not dependent on firing configuration; however, follow up studies are needed. In particular, wall electron temperature measurements will indicate whether subtle changes are impacting the overall sheath potential and therefore erosion.

7.4 Conclusions

In this chapter, we first contextualized our results and discussed our improved physical picture for the way in which neutrals impact high-power Hall thrusters. In particular, we

showed how single-channel Hall thrusters are neutral source agnostic, and the neutral density in the exit plane of the thruster drives changes in performance due to acceleration region movement. These shifts are also leading to measurable changes in the high energy tail in the near-wall region. For nested Hall thrusters, our physical pictures of a compressing acceleration region and neutral ingestion leading enhanced performance is consistent with the results of single-channel Hall thrusters, including the lack of change in the near-wall behavior. Overall, our comprehension of how neutrals impact these devices is improved by the results discussed in this chapter. However, there are certainly areas of research required to better clarify these changes. In Chapter 8, we provide a summary of the work presented here before discussing the future work needed to deepen our understanding.

CHAPTER 8

Conclusions and Future Work

8.1 Summary of Work

We presented an investigation into the influence of neutrals on the behavior of high-power Hall thrusters. To enable this investigation, we first presented a theoretical framework for how neutrals impact Hall thrusters. We focused on two different Hall thruster types: magnetically shielded Hall thrusters and nested Hall thrusters (both shielded and unshielded). In Chapter 2, we detailed how neutrals can change the divergence and voltage utilization of single-channel thrusters. In particular, we discussed how acceleration region movements due to neutral changes can modify these parameters which should then correlate to changes in performance. We also detailed the physics of magnetic shielding which increases the lifetime of these thrusters by upwards of three orders of magnitude. However, the technology is predicated on the grazing line sampling deep enough in the channel and on having a cool electron temperature which results in high potential near the wall. A shifted acceleration region could potentially change this temperature leading to a reduced thruster lifetime with increased neutral density. In space, where there is a lower density, this could actually increase the lifetime. Next, in Chapter 3, we detailed how neutrals emanating from adjacent channels in nested Hall thrusters can lead to neutral ingestion and divergence changes. In turn, this yields increased performance in multi-channel operation as compared to single-channel operation. Finally, we briefly detailed how a shifted acceleration region could

also impact the lifetime of magnetically shielded nested Hall thrusters, in the same manner as single-channel Hall thrusters.

After presenting our theoretical framework, we detailed the experimental methods in Chapter 4 including the thrusters used (H9, X2 and N30) and the diagnostics. Critically, we detailed LIF which was used during all the experimental investigations to measure the ion velocity distribution function on centerline and near the wall of these thrusters. This then allowed us to quantify the location of the acceleration region. We also discussed the Faraday probes used to measure the divergence angle, the thrust stand, the Langmuir probe to measure coupling voltage, and the pressure gauge to measure the near-field neutral density. Once our experimental methods were established, we presented our results, beginning with the H9. First, we showed that the acceleration of the thruster shifts inward with increasing neutral density. We varied the neutral density both by changing the background pressure and the cathode flow fraction. This occurred for both internally and externally mounted cathodes. This effect appeared to "saturate" in that neutral density changes above a certain level did not lead to continued shifting. We then showed that the cathode coupling voltage was not impacted largely by the change in neutral density and did not correlate to the shifts in acceleration region. Finally, we showed that the change in the acceleration region led to measurable changes in thrust for the externally mounted cathode. Furthermore, we were able to reduce these changes by "saturating" the neutral density.

We then moved on to presenting the near-wall LIF measurements. They showed that the average velocity vector did not change significantly with neutral density, and given our estimates for electron temperature the tail of the IEDF also did not change substantially with changing pressure. In Chapter 6, we showed that by turning on adjacent channels, we changed the neutral density in the near-field of the X2. This, in turn, led to measurable changes in thrust, divergence angle, beam current, and the IVDF. However, when the

adjacent channel flow was on, dual channel and single-channel measurements generally matched within uncertainty. This suggested that the changes induced from single-channel to dual-channel mode were due to the increased neutral density. Finally, we showed the near wall velocity vectors and IEDFs were not changed on the inner channel of the N30 when the outer channel flow was turned on.

After presenting the experimental results, we concluded our work with a discussion in Chapter 7. In this discussion, we started by showing that the H9 acceleration region shifts were correlated with both background pressure and cathode flow fraction. Estimating the change in neutral density due to both of these impacts show that at the exit plane, the change in neutral density was similar. Additionally, the source of the neutrals was not critical. This suggested that we could predict a shift in the acceleration region based on this change in neutral density. Additionally, it indicates that controlling that density would allow for some control of the location of the acceleration region, and therefore performance of the thruster. We have hypothesized some potential explanations for this asymptotic (and agnostic to source) behavior of the discharge, though this is still an open question. We also discussed how higher neutral density would lead to higher thruster erosion. However, since pressure decreases from ground facilities to flight, this is not a large concern. We then moved on the nested Hall thruster results. We successfully showed that we can explain the improvements in performance of a dual channel versus single channel thruster by taking into consideration the shifts in divergence angle and ingestion that result from gas "recycled" from adjoining channels. This showed that the changes were induced by neutrals. We briefly touched on the differences in oscillations, however their impact was not quantified. Finally, we discussed how a compression instead of a shift of the acceleration region could have led to the lack of changes in the near-wall behavior on the N30.

Overall, we have better developed our physical description of neutral impacts on

magnetically shielded Hall thrusters. In general, neutrals near the exit plane can shift and compress the acceleration region. The source of these neutrals is not critical – it can be the background, the cathode, another channel, etc. This change in the acceleration then leads to a change in the divergence and beam current of the thruster. In turn, this leads to a change in thrust and efficiency. These neutrals do not appreciably change the near-wall behavior of ions, likely because the electron temperature profile in that region is relatively flat. Thus, there is little change to the erosion and overall lifetime of high-power magnetically-shielded Hall thrusters.

8.2 Future Work

While the work presented here significantly improved our understanding of neutral density effects on high-power Hall thrusters, there are many areas of continued research needed to complete the physical picture. Several areas of investigation were identified as a result of these studies. Listed below is a summary of the clearest, and perhaps most critical, next steps in the research area as seen by the author. This is not an exhaustive list. Finally, we would like to note that the future work listed below can be investigated experimentally, numerically, or analytically.

8.2.1 Analytical Prediction of Parameters

In Chapters 2 and 3, we detailed a theoretical outline for neutral impacts on both single-channel and nested Hall thrusters. In order to investigate this framework, we performed a number of experimental investigations. Indeed, many of the parameters we aimed to predict required experimental data as inputs. For instance, our nested-Hall thruster performance model required the measurement of ion velocity, divergence, beam current and local neutral density in order to accurately predict multi-channel thrust. To use this model a priori to optimize thruster design, we must have analytical (or at a minimum empirical) expressions for

all these parameters and not rely on experimental data. The development of expressions for the impact of neutrals on various thruster parameters is critical. In fact, many of the studies detailed below aim at a better understanding of many factors required for this analytical prediction. [188]

8.2.2 Neutral Impacts on Lifetime

The results here showed the ion trajectories in the near-wall region of two magnetically-shielded Hall thrusters. Overall, the tail of ion energy distribution function is close to the sputtering threshold of 30 eV after sheath acceleration, assuming an electron temperature of 5 eV for the grazing line. While this temperature was based on heritage [20], it was not measured. Therefore, it was difficult to assess whether a shift in the centerline profile led to a change in the temperature of the grazing line. First and foremost, we believe a direct measurement of the wall temperature, and how it changes with neutral density, is critical. The sputtering threshold of 30 eV is not a well-established threshold so a measurement of the low energy sputtering threshold for various materials is also critical. Finally, ground testing yields a build-up of conductive carbon on the walls of Hall thrusters due to the use of a beam-dump. However, this slow change from an insulator to a conductor changes the sheath conditions considerably. A better understanding of this transition, or conversely the differences between insulator and conductor near wall behavior, is critical as this beam-dump is not present on orbit.

8.2.3 Acceleration Region Movements

We correlated the movement of the acceleration region to a change in neutral density near the exit plane of the thruster. We also showed that divergence angle changes as a result of this movement of the acceleration region. Finally, we analyzed these changes in divergence and showed that they lead to changes in thrust. All these impacts were predicated on measuring the shift in the acceleration region. The shift had a non-linear response to neutral density,

eventually saturating and no longer shifting. What exactly causes this movement remains unclear. While the acceleration region typically sits near the peak radial magnetic field, its exact location is not predictable. This location is likely intrinsically linked with electron transport, which as of now cannot be analytically predicted. Regardless, investigations into the mechanism behind acceleration region movement are critical to our understanding of neutral impacts and Hall thruster physics. The leading theory of electron transport in Hall thrusters is that it is driven by turbulence. [189–192] Additional neutral gas can increase electron-neutral and ion-neutral collisions which most likely would reduce the transport of electrons in the near-field plume through a damping of this turbulence. This enhanced resistivity could stretch the acceleration region downstream. However, this theory is not consistent with the results presented here and thus further investigation is necessary.

8.2.4 Oscillatory Behavior

Throughout this work, we noted that the oscillatory strength and behavior of these thrusters was varying with neutral density. Much of the previous work described in Chapter 2 also investigated how background neutrals changed the oscillations of Hall thruster. However, there remains no clear physical picture of how neutrals change the oscillations of Hall thrusters or why there are differences between thrusters. In this work, we did not attempt to correlate changes in oscillations to changes in thruster behavior or lifetime. Again, because the exact mechanism of these oscillations remains an area of investigation, this task is difficult. Continued investigations into Hall thruster oscillations, neutral impacts on these oscillations, and critically, how these oscillations impact performance is another clear area in need of additional investigation. This investigation is complicated by the fact that many parameters of Hall thrusters impact the oscillations and thus it is very difficult to isolate this variable.

8.2.5 Cathode Coupling

We briefly discussed changes in cathode coupling in this work. However, we found these changes to be minimal and there was no clear trend. Previous works [88,174] have attempted to predict the cathode coupling voltage versus neutral density. However, a more dedicated experimental and analytical treatment is warranted.

8.2.6 Other Efficiencies

In this investigation, we focused on two Hall thruster efficiencies: voltage utilization and beam divergence. However, there are many other efficiencies that drive Hall thruster operation such as charge utilization and beam utilization. While we did not present a mechanism by which these efficiencies would be impacted by neutrals, that does not preclude the existence of one. Therefore, further systematic investigations into neutral impacts on the other aspects of Hall thruster operation are critical.

8.2.7 N30 Studies

Our investigations only explored a very small parameter space for nested Hall thrusters. In particular, our study for performance changes was only performed on a single thruster and that thruster was unshielded. A clear extension of this work is to repeat this experiment on the N30 to see if the results hold for magnetically shielded NHTs. Additionally, our lifetime studies were limited to the inner channel alone and the inner channel with outer flow on. There exist at least three other conditions that need to be studied: the outer channel alone, the outer channel with inner flow on, and both channel in dual channel operation. Again, wall electron temperature measurements are also critical. Finally, we did not investigate the impact that change in the cathode flow (as will occur for dual channel mode) will have on both the performance and lifetime of these thrusters. While there are many other areas of investigation for NHTs, the above are the clear next steps to better understand neutral

impacts on these devices.

8.2.8 Cathode Injection Scheme

In Chapter 7, we discussed the ability to reduce the susceptibility to background neutrals by changing the cathode flow fraction. In particular, the critical parameter is the addition of neutrals, not a change in the cathode plume. However, we noted that the changing the cathode flow fraction impacts the cathode lifetime. Our suggestion to mitigate this issue was neutral injection through the cathode-keeper gap since we believe neutrals are driving the response. Thus, a simple experiment repeating centerline IVDF measurements versus cathode flow where the excess flow is injected in this gap will confirm this behavior.

8.3 Concluding Remarks

Overall, this work has quantified the way in which neutrals impact the operation of Hall thrusters. Furthermore, it has provided potential mechanisms to "control" the response of these thrusters to changing background neutrals. For nested Hall thrusters, the work substantially improved our understanding of how their operation differs from single-channel Hall thrusters which provides critical information towards increasing the technology readiness level. This work provides a backbone for future investigations into Hall thruster susceptibility to neutrals and for future work into high-power nested channel Hall thrusters. Ultimately, this work improved our understanding of the ground-to-flight transition, which reduces the risk of flying Hall thrusters and increases their overall applicability to space missions.

APPENDIX A

H9 Acceptance Testing

A.1 Introduction

In this Appendix, we provide detailed acceptance testing results from the H9 Hall thruster. We begin by detailing the purpose and objectives and specifications for the thruster. [123] We then move on to describe equipment used that was not previously described: the Owen's Chamber at JPL and the thrust stand employed at JPL. After discussing the necessary test equipment, we detail the anode flow uniformity testing, the magnetic field mapping, and the performance of the thruster.

A.1.1 Purpose and Objectives

The primary purpose for the H9 was to continue the collaborative tradition of the H6 as a testbed for studies of thruster physics and developments in diagnostics and thruster technology. The specific objectives of the new thruster were to:

- Implement a magnetic circuit that retains magnetic shielding at discharge voltages up to 800 V,
- Provide a medium power (5-10 kW), high-specific impulse (2500-3000 s) laboratory thruster that can be tested at less than 20 μTorr in a wide variety of vacuum facilities in the United States,

- Provide a mechanical design that is simple and flexible enough to accommodate various plasma diagnostics and potential hardware changes,
- Provide a common thruster with a well-documented configuration across several institutions so that results can be easily compared, and
- Serve as a benchmark for the inner channel of a two-channel Nested Hall Thruster (NHT) incorporating magnetic shielding. This new development, which is being led by UM in collaboration with JPL, will demonstrate the ability to magnetically shield NHTs and could potentially be integrated in to UMs 100 kW-class X3 NHT [141].

A.1.2 Specification

The H9 design specification was derived from the motivation and objectives in the previous section. Similar to the NASA-173M design relative to the P5 [56], the H9 magnetic field topography is the primary design variable that was changed relative to the H6MS and H6US. In this way, we can compare the operation and performance of the H9 relative to the H6 while holding other design features essentially constant. The main elements of the H6MS that are retained include:

- The discharge chamber geometry (mid-channel diameter, channel width, channel length)
- A segmented discharge channel with replaceable rings near the exit region
- The anode/gas distributor [5, 157]
- A compact, centrally-mounted LaB6 hollow cathode [64, 154]

As elaborated on further in the sections that follow, new elements of the H9 design include:

- A magnetic circuit that provides a higher degree of magnetic shielding than the H6MS
- Improvements in the thermal and mechanical design that enable 9 kW operation

- Incorporation of graphite pole covers to mitigate pole erosion [42]

Figure A.1 depicts the operating envelope of the H9 and several Reference Firing Conditions (RFCs), which are listed in Table A.1, that are used to benchmark performance. Aside from operation demonstrated at the RFCs, the operating envelope is a conservative prediction based on experience operating the H6US, H6MS, and HERMeS [111,112,125]. For example, the upper current limit of 40 A is based on H6US operation [193,194], the lower current limit of 2 A is based on the H6MS [28], and the minimum current for voltages greater than 300 V is estimated from experience operating the H6MS and the high-I_{sp} truncation for HERMeS described in Ref. [125]. Operation up to 12 kW is an expected capability of this laboratory design, but is not included here as it may prove challenging if this laboratory model were developed for flight. The maximum, estimated thrust of 560 mN for this operating envelope occurs at 225 V, 40 A. At 600 V, the maximum specific impulse at the minimum power would be about 2600 s, while at 800 V, the maximum specific impulse at the minimum power would be about 2900 s.

Table A.1: Reference Firing Conditions used during the initial testing of each H9 thruster.

Discharge Voltage (V)	Discharge Current (A)	Discharge Power (kW)
300	15	4.5
300	20	6
400	15	6
500	15	7.5
600	15	9
800	11.25	9

A.2 Test Equipment

A.2.0.1 Owen's Chamber

Thrust measurements on SN03 were performed in the Owens Chamber at JPL (Figure A.2). The Owens chamber is a 3 meter by 10 meter cryogenically-pumped vacuum facility. This

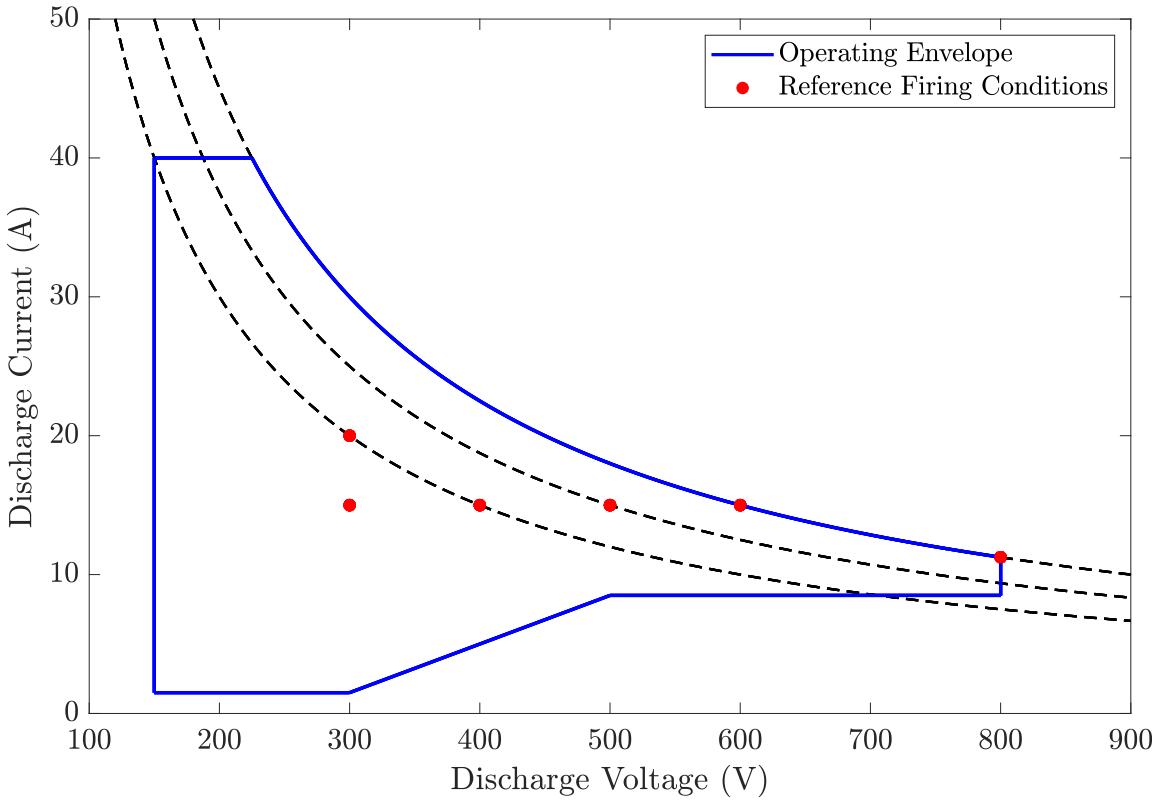

Figure A.1: H9 operating envelope and Reference Firing Conditions used during the initial testing of each thruster

Figure A.2: The H9 SN03 installed in the Owen's Chamber at the Jet Propulsion Laboratory for thrust measurement testing.

facility has been used previously to test gridded ion and Hall thrusters at power levels exceeding 20 kW [64, 156, 195, 196]. We monitored pressure in the Owens with a pair of ionization gauges. The first ionization gauge, used to measure the best pressure of the facility, was calibrated for nitrogen and mounted to the chamber wall downstream of the thruster exit plane. The base pressure during the tests was 9.9×10^{-7} Torr-N_2. The second ionization gauge was calibrated for xenon, mounted at the thruster exit plane and used to measured operational pressure.

A.2.1 Diagnostics

A.2.1.1 Thrust Stand (JPL)

We employed a water-cooled inverted-pendulum thrust stand at JPL (Fig. A.2) to make thrust measurements [111]. The thrust stand operated in displacement mode with active inclination control and damping. The thruster was run through a 4 hour outgassing and

warming procedure (up to 800 V) prior to any measurements being acquired. The thruster was run at a constant power for 20 to 30 minutes during which the inclination was controlled to a dead band for thrust measurements. Thermal drift and inclination of the thrust stand were accounted for during post-processing. No corrections were made for the effects of neutral ingestion due to the backpressure that ranged from 10.4-13.5 utorr-Xe. Prior testing on the H6MS has shown that the thrust is nearly invariant with backpressure and that the flow rate correction to vacuum from these pressures is about 1% [28]. Calibrations were performed by deploying a series of known weights. When inclination and thermal drift were accounted for, the response of the thrust stand was repeatable and linear to the applied force. Analysis of thrust stand data indicated an uncertainty of 1%.

A.3 Acceptance Testing

In addition to standard part and tolerance inspections upon assembly, we performed two additional acceptance tests on the three assembled units: an anode flow uniformity check and magnetic field mapping.

A.3.1 Anode Flow Uniformity

The azimuthal flow uniformity was assessed by neutral density testing with a Series 370 Stabil Ion Gauge at JPL (Fig. A.3) The H9 discharge chamber and anodes were placed on a rotary stage with the gauge inlet located radially on channel centerline and axially midway through the discharge chamber. Each anode was measured at 36 evenly-space radial locations. We performed tests at xenon flow rates of 2 mg/s and 20 mg/s. The dwell time at each test point was 10 seconds. An acceptable flow uniformity criteria of deviations up to 10% (δP_{max}) from the mean value ($\bar{P}$) was used during testing [197]. Results, seen in Figure A.4, show that all anodes were within the acceptable criteria for uniformity.

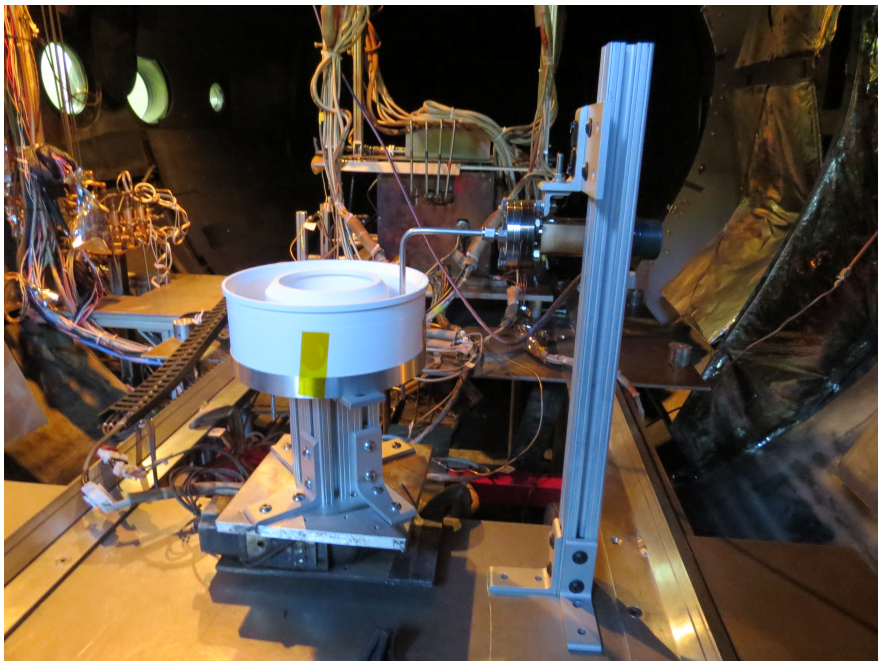

Figure A.3: Test setup for anode flow uniformity testing at JPL.

During low flow testing (2 mg/s), the highest deviation minus lowest deviation with respect to the mean pressure ($\frac{\delta P_{max}}{\bar{P}} \times 100\%$) was 9.23% for SN01, 4.57% for SN02, and 4.05% for SN03. As our acceptance criterion allows for a maximum allowable deviation of 10%, the three anodes thus all passed the acceptance test at this flow condition. During high flow testing, the same metric was 6.46%, 3.64%, and 3.35% for SN01, SN02, and SN03 respectively. Based on these data, all anodes similarly passed the acceptance test at the high-flow condition.

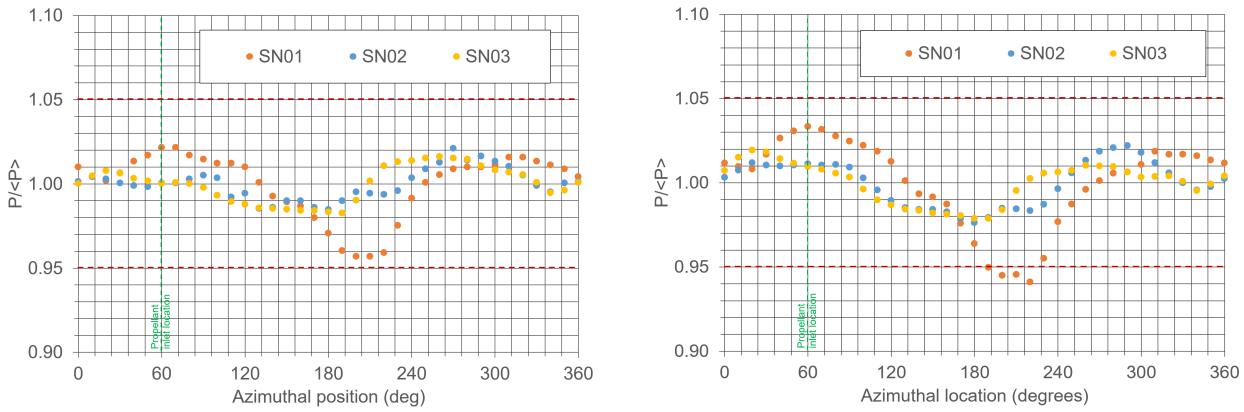

(a) (b) Nested Hall thruster

Figure A.4: Flow uniformity testing results for all anodes (a) high flow testing showing all anodes within the allowable ±5% range and (b) low flow testing showing only SN01 with deviations greater than 5% from the mean. However, for SN01 the total $\frac{\delta P_{max}}{\bar{P}} \times 100\%$ was still less than 10%.

A.3.2 Magnetic Field Testing

In order to verify that the magnetic circuit was constructed properly, we mapped each thruster's magnetic field with a translating Gauss probe and compared the measurements between thrusters as well as to a reference design field shape. This latter field was originally specified during the design phase when the thruster's circuit was modeled with Infolytica's MagNet v7.7. The mapping revealed that each thruster matched the simulation and each of the other thruster's very well. In addition to two-dimensional maps, we also measured the maximum centerline radial magnetic field for each thruster. Figure A.5 shows the results of this test versus inner coil current. Figure A.5a shows that the magnetic field magnitude generated by the circuit is linear up to 50% higher than the nominal magnetic field strength. Additionally, Figure A.5b shows that up to 5.5 A each thruster is within 2% of the value expected based on inner coil current of 2 A until the curve begins to deviate from linearity. The deviation plotted here is the difference between the actual value at the given coil current and the value predicted based on proportionally scaling the magnetic field strength at 2 A for each thruster. Figure A.5b shows each thrusters magnetic field peak is within 2% of all other

thrusters for all measured inner coil currents. Given these small variations in magnitude and the fact that the magnet field maps in the channel were all quantitatively very similar, we ultimately determined that all thrusters passed this acceptance test.

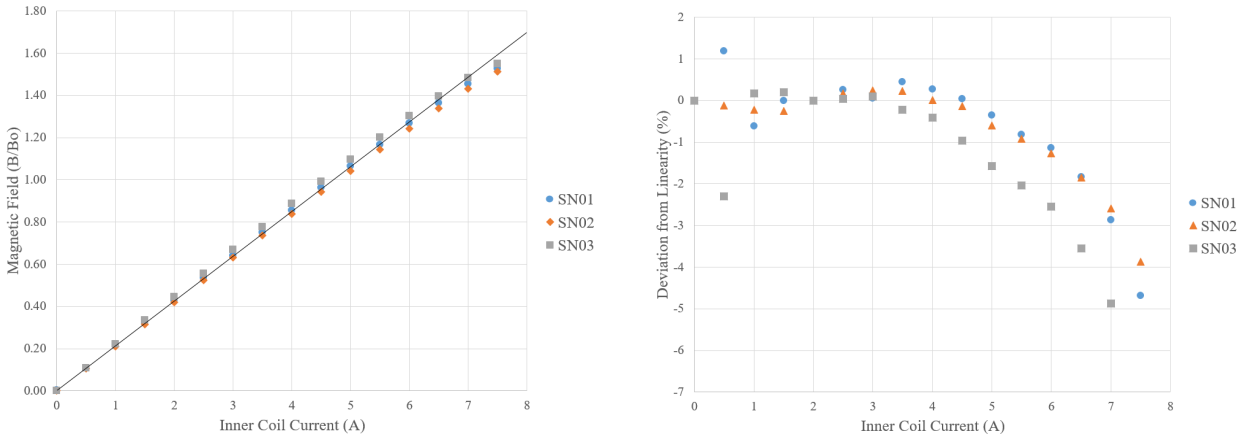

(a) (b) Nested Hall thruster

Figure A.5: (a) Inner coil current versus relative magnetic field strength showing linearity in the circuit up to 50% above the nominal magnetic field setting for each thruster. (b) Deviation in expected magnetic field strength in percent based on a proportional scaling relative to inner coil current at two amps. Results show that each thruster is within 2% of each other thruster.

A.4 Performance Testing

We performed thrust measurements at JPL only on the thruster built for the University of Michigan, the SN02. In this section, we detail the performance as well as indications of magnetic shielding for the SN02.

A.4.1 Indications of magnetic shielding

Throughout the testing campaigns, there were many qualitative indications that the magnetic shielding topography had been achieved. Figure B.11(b) shows, for example, noticeable carbon deposition on the thruster discharge chamber after approximately 10 hours of firing. With an unshielded thruster, we would expect to

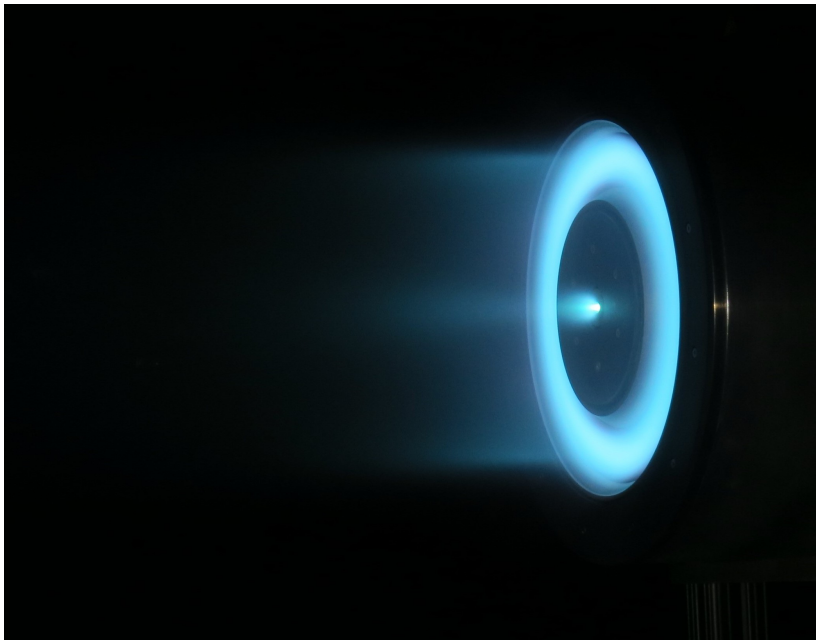

Figure A.6: The H9 SN02 firing in the Owen's Chamber at JPL during initial performance testing.

see carbon deposition deep in the discharge chamber, but closer to the exit plane where erosion from beam interaction occurs, the rings should remain white. Figure B.11(b) shows that carbon is coating the entirety of the discharge chamber and rings. This is the first qualitative indication of magnetic shielding [20]. As a second indication (Figure A.7), we observed during operation that there was a zone of high light emission in the center of the channel, with decreased intensity near the walls to the point that the anode could be seen while the thruster was firing. This again is a qualitative indication of magnetic shielding as it indicates a cooler electron temperature at the discharge chamber boundary. This was previously noted for the H6MS shielded thruster

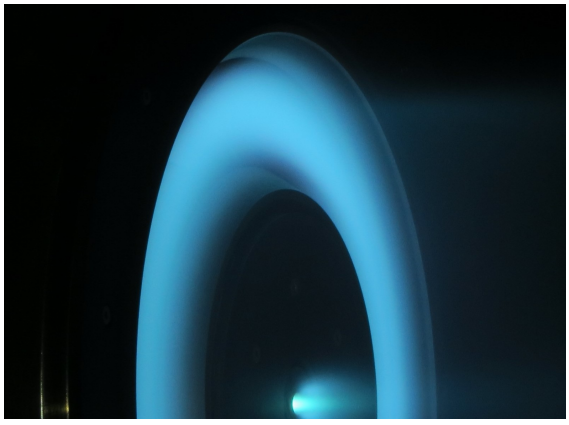

Figure A.7: Zoomed in photo of the H9 SN02 discharge chamber during testing at JPL.

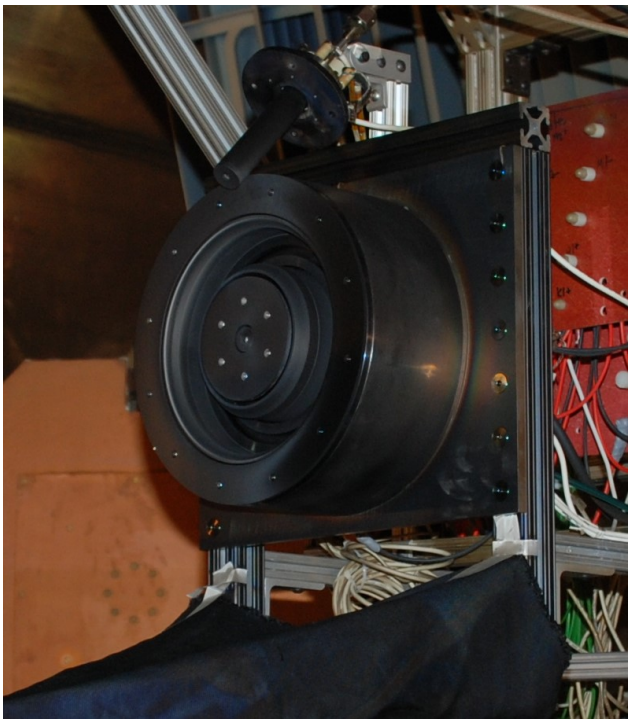

Figure A.8: The H9 after approximately 100 hours of firing at the University of Michigan. Build up of carbon along the entirety of the discharge chamber walls is a qualitative indication of achieving a magnetic shielding topology.

in Ref. [111]. Despite these qualitative indications, we do note here that these observations are necessary but not sufficient criteria to claim that the thrusters are shielded. However, since these qualitative indications are present, as well as the H9 following the same design philosophy of the H6MS and HERMeS, both of which have quantitative measurements of shielding, we are able to say that the thrusters are shielded.

A.4.2 Thrust

Before taking thrust measurements at each operating condition, we first performed a magnetic field optimization. In brief, we parametrically varied the magnetic field intensity at each operating condition and monitored oscillations in the discharge current. We selected the

Table A.2: Performance results for the reference firing conditions taken from SN02 at JPL.

Test Point	Voltage [V]	Current [A]	Power [kW]	Thrust [mN]	Total I_{sp} [s]	Total Efficiency
1	300	15	4.5	283.4	1914	0.60
2	300	20	6	372.3	1987	0.60
3	400	15	6	345.5	2196	0.62
4	500	15	7.5	392.9	2422	0.62
5	600	15	8	436.2	2652	0.63

magnetic field based on where these oscillations are minimized. With this in mind, we show in Table A.2 the results of H9 SN02 thrust measurements from the campaign conducted at JPL. As would be expected, the thrust increases with current and discharge voltage: $T \propto I_d\sqrt{V_d}$. From these measurements, the flow rates, and input power, we similarly were able to determine the specific impulse $I_{sp} = \frac{T}{\dot{m}g}$ and total efficiency $\eta = \frac{T^2}{2\dot{m}P}$, also shown in Table A.2. The values indicate state-of-the-art performance with throttle-ability all while maintaining total efficiency above 60%. In general, the H9 performance is on par with other state-of-the-art magnetically shielded thrusters showing thrust-to-power up to 65 mN/kW and efficiencies up to 63%.

APPENDIX B

N30 Acceptance Testing

B.1 Introduction

In this Appendix, we provide detailed acceptance testing results from the N30 Hall thruster. We begin by detailing the operational envelope for the thruster as well as the component features. [123] We describe the equipment used for acceptance testing and initial performance measurements. While some of this equipment was described in Appendix A, we repeat it here in light of subtle changes to the setup. We then detail the anode flow uniformity testing, the magnetic field mapping, and the performance of the thruster. Finally, we provide discussion on the implications of the thruster and challenges moving forward.

B.2 Operational Envelope

Table B.1 details the matrix of Reference Firing Conditions (RFCs) used to benchmark performance. There exist 18 reference firing conditions. The first six conditions in the table (first three columns) are for the inner channel operating alone and are identical to the H9 RFCs. [123] The next six (columns four to six) are for the outer channel operating alone. They are scaled from the inner channel RFCs to maintain the same current density among the two channels. Finally, the last six conditions are dual channel operation and are simply the summation of the inner channel operating alone and the outer channel operating alone. The total power for these six conditions is listed in the last column of the table.

Table B.1: Reference Firing Conditions for the N30.

Inner Voltage (V)	Inner Current (A)	Inner Power (kW)	Outer Voltage (V)	Outer Current (A)	Outer Power (kW)	Total Power (kW)
300	15	4.5	300	38.9	11.7	16.2
300	20	6	300	51.8	15.5	21.5
400	15	6	400	38.9	15.5	21.5
500	15	7.5	500	38.9	19.4	27.0
600	15	9	600	38.9	23.3	32.3
800	11.25	9	800	29.2	23.3	32.3

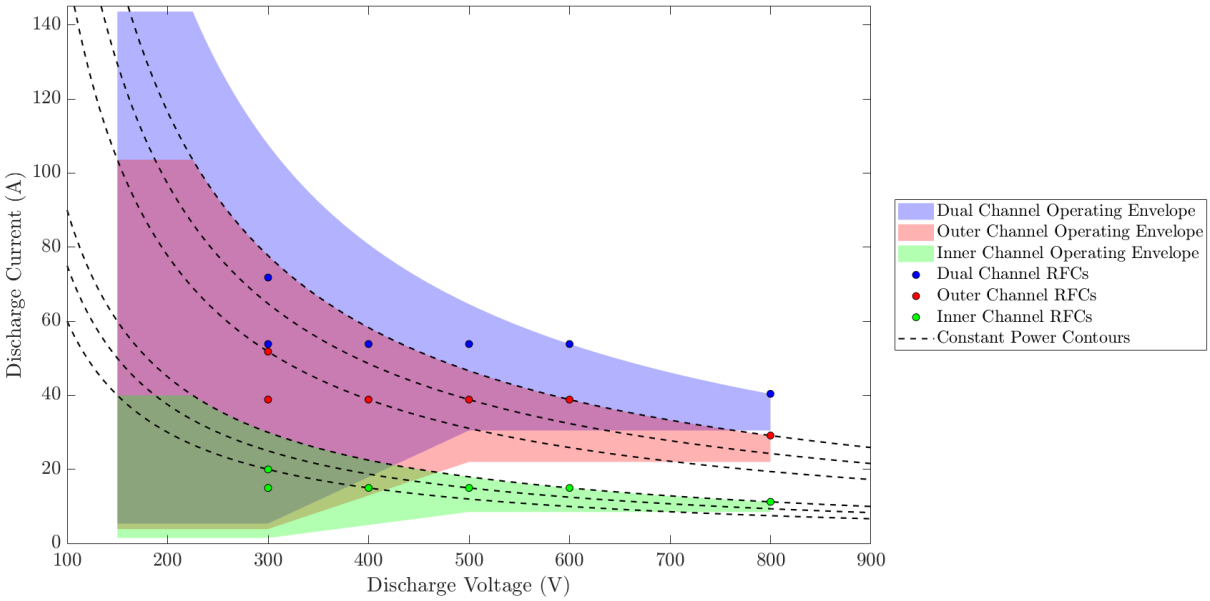

Figure B.1: A graphic representation of the full operational envelope of the thruster. The dots are the reference firing conditions for each firing configuration: inner channel only, outer channel only, and dual channel.

Figure B.1 depicts the full operational envelope for the N30. This operational envelope is estimated from experience with the H6, H6MS, H9 and HERMeS Hall thrusters. [111, 112, 123, 125] Similar to the H9, the maximum possible combined (inner and outer channel) thrust is estimated to be 2.0 N at a discharge current of 144 A and voltage of 225 V. At 800 V, we expect the specific impulse to reach at least 2900 s. These predictions assume

power can be added linearly when predicting dual channel operation despite knowing that the channels interact. One feature that is evident from the operating envelope is the overlap of achievable powers between different operating conditions. This feature, unique to nested Hall thrusters, allows for a larger range of thrust and specific impulse values for a given power depending on current mission needs. In other words, this graph depicts that high specific impulse performance is achievable over a much wider range of power levels (7 kW to 32 kW) than traditional Hall thrusters.

B.3 Component Features

B.3.1 Discharge Chamber

Similar to the H9, both discharge chambers (inner and outer) have a "U-shaped" wall and replaceable "rings" near the exit. [123] This design, originally from the H6, allows for easy integration of wall probes or a change of material to study plasma interactions. [**?**, **?**, 62, 120]

Figure B.2 schematically shows this base and ring configuration. Nominally, both discharge chambers and all rings are made from a borosilicate ceramic. The inner discharge chamber shares the same mean diameter, length, and channel width as the H9. The outer discharge chamber shares the same length as the inner. The scaling for the mean diameter and the width for the outer channel was based on previous experience with the X2 and X3 as well as necessary spacing to fit the magnetic circuit. [131, 162]

B.3.2 Anode/Gas Distributor

The combined anode and gas distributor is used to inject neutral propellant into the discharge chamber as well as provide the bias for the axial electric field. The anode for the inner channel, previously described [5, 157], ensures high azimuthal uniformity of the neutral gas which is critical to efficient operation.

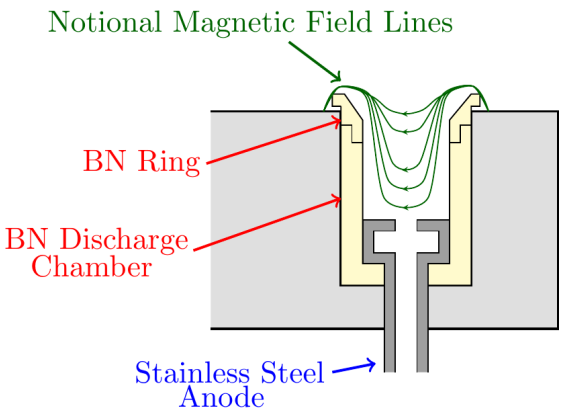

Figure B.2: A notional schematic of each discharge chamber for the NHT featuring an anode, a discharge chamber base and removable rings. Not to scale.

While the gas distributor geometry for the outer channel was scaled similarly to the scaling for the discharge chamber, the scaling of a few key parameters meant to achieve high flow uniformity, such as number of propellant inlets, were initially unknown. Thus, to ensure that the outer anode achieved similar performance to the inner anode, we performed numerical simulation on a variety of geometries. A three-dimensional simulation of xenon neutrals was performed using the computer code Monaco, an implementation of the direct simulation Monte Carlo method (DSMC). [198, 199] The geometries considered were the entire anode geometry as well as the discharge chamber and rings. We used a diffuse wall condition at the thruster channel walls, and particles were allowed to escape the domain at the discharge chamber exit plane. The only location of inflow was at the anode inlet tubes. Simulated number density profiles were then extracted, in the same axial location as previous experimental anode flow uniformity tests to compare case to case. [**?**, 123] Once a sufficiently uniform (criteria to be discussed in Section B.5,B.5.1) was achieved with the simulation, the design for the outer anode was finalized.

B.3.3 Cathode

The cathode supplies electrons for both the discharge and neutralization of the plume. Here, we use a centrally-mounted lanthanum hexaboride (LaB_6) hollow cathode. This device is similar to the cathodes used for all the H6 and H9 testing. [**?**,64,156] The original component used for the H9 testing has been operated up to 60 A during development. [154,155] However, at its highest nominal operating condition, the N30 requires 71.8 amperes of current. Thus, a new cathode was required for this thruster. In order to achieve higher current, the LaB_6 insert size was increased to permit currents up to 100 A. However, the overall form factor of the cathode did not change. This was critical to enable this device to be used with both the H9 and N30 thrusters. Additionally, there are design features on the cathode that ensure the exit plane of the keeper is at the same axial location on both thrusters. During initial testing, the cathode was operated up to 60 A. This device is now the nominal electron source for both thrusters.

B.3.4 Magnetic Circuit

The magnetic field was numerically simulated using Infolytica's MagNetv7.7 software. A significant portion of the effort during the design phase was spent on the magnetic field, as the design of nested Hall thruster magnetic fields is inherently more complicated than single channel thrusters. This complexity is illustrated in Figure B.3. When the thruster is operating in single channel mode (either the inner or outer), a NHT magnetic circuit acts similar to a standard Hall thruster. That is to say, the channel has two dedicated electromagnets and similar pole pieces. There still exists more physical magnetic material; however, the material from the other channel does not impact the field shape significantly. When running in dual channel mode, the outer magnetic poles for the inner channel also act as the inner magnetic poles for the outer channel. This shared pole makes the design of the magnetic circuit complicated as small changes impact both field shapes. Additionally, previous work showed that NHT magnetic fields are not simply the summation of single

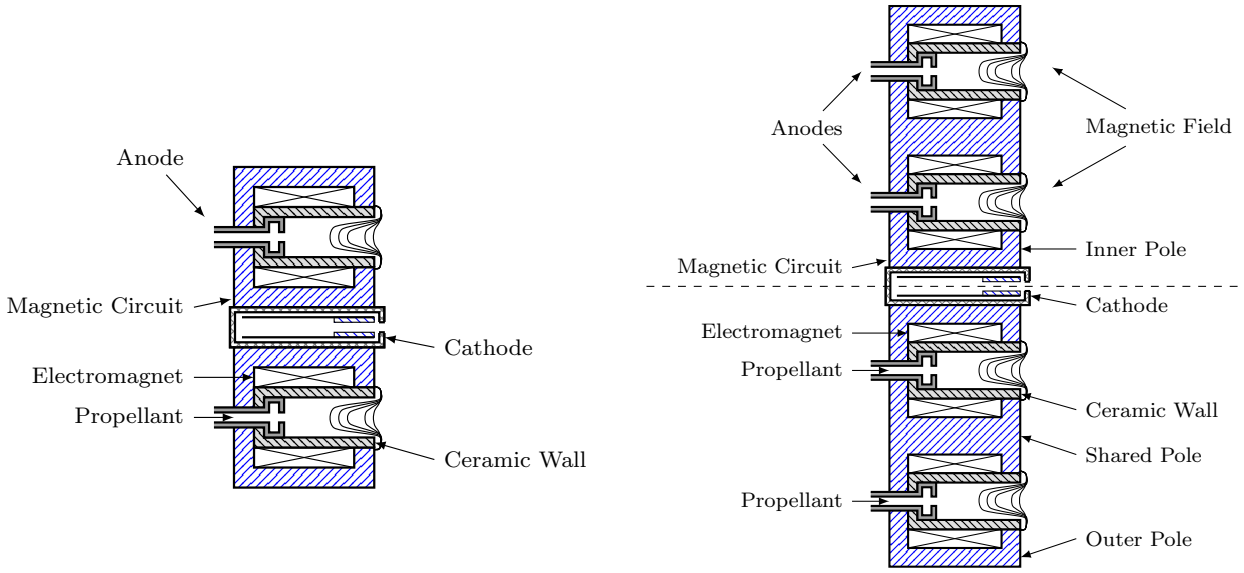

Figure B.3: A schematic detailing the differences between a standard Hall thruster (left) and a nested Hall thruster (right). Most notably, the nested Hall thruster has shared magnetics between each channel making magnetic field design challenging.

channel field and each firing condition must have its field optimized separately. [**?**]

Similar to the H9, the NHT does not use discrete outer coils. This ensures azimuthal uniformity of the magnetic field. In order to achieve the magnetic field shape and structure, we employ four electromagnets, two dedicated to each channel. These electromagnets allow us to vary the strength of the magnetic field and easily achieve 800 V operation of the thruster while remaining fully shielded. The saturation properties of the magnetic circuit for each channel are equal or better to those of the H9's circuit. While the starting geometry for the inner channel was that of the H9's, changes were made to the poles to ensure that the field in the discharge chamber was nearly identical to that of the H9's. The outer channel field has a similar shape, symmetry, and centerline profile as the inner channel. The downstream gradient of the field reduced in magnitude due to the widening of the channel as seen in Figure B.4. Importantly, the depth of the grazing line is similar between the two channels.

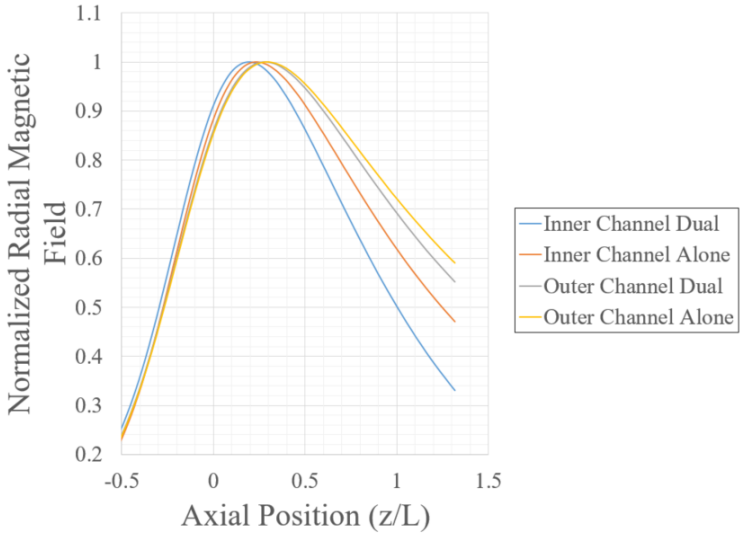

Figure B.4: Centerline profiles for all configurations of the magnetic field. The increase in the gradient for the inner channel alone versus in dual channel mode is evident.

Simulations by Mikellides et al. of the X3 showed that the difference in magnetic field gradient on channel centerline between the outer channel and the inner and middle channels led to changes in downstream plasma potential. [160] They suggested that there was further room for magnetic field optimization because this change of gradient could impact the cathode coupling voltage and accelerating voltage for the channel. However, we found here that this change in magnetic field gradient difference of the peak is in fact inherent to the design of nested Hall thrusters. A simple dipole model shows that the presence of an outer magnetic field in fact "squeezes" the gradient on the inner channel. Thus, the inner channel gradient will always be greater than the outer channels in dual channel mode (as seen in Figure B.4). This leads to the conclusion that it will always be challenging to get the same plasma potential downstream of the inner and outer channels. Additionally, cathode coupling will always be slightly different between the two channels.

The final and most critical part of the magnetic field design process was to optimize the field for all firing configurations. Previous worked showed that not optimizing the field

for each firing configuration of an NHT could drive the plasma into the walls, leading to degrading performance and higher thruster oscillations. [161] Additionally, since magnetically shielded thrusters require the plasma to be "shielded" from the walls, non-optimized field could impact thruster lifetime. Thus, prior to manufacturing, simulations were performed to ensure that each firing configuration produced a shielded topology and to optimize the fields only changes to the electromagnet setpoints were necessary.

B.3.5 Other Features

While the component features listed above are most critical, there are several other important features of the thruster worth noting. First, many steps were taken to mitigate the high thermal load of the plasma and maintain reasonable temperatures for the thruster. These include the anodization of the thruster stand and a spray coating on the outer guide of the thruster. These processes both aim to increase the emissivity of their respective parts to enhance radiative heat transfer. Similarly, many parts of the magnetic circuit were "sand-blasted" to enhance their emissivity and encourage heat transfer to the outer surfaces of the thruster. In order to monitor the temperatures of the thruster, many thermocouples were integrated and embedded throughout to observe real-time thruster health.

The final two features of note are the pole covers and the thruster electrical configuration. Graphite pole covers were incorporated on the downstream surface of all poles. These pole covers prevent the erosion of the magnetic pole surfaces, which is known to be higher for magnetically shielded thrusters than unshielded thrusters. [**?**, 102] Additionally, while there is the ability to run the thruster in any electrical configuration, the nominal configuration is "cathode-tied," where the body voltage is electrically-tied to cathode potential. This configuration limits the floating potential of the thruster to reduce pole erosion and extend lifetime. [125, 158, 159]

B.4 Test Equipment

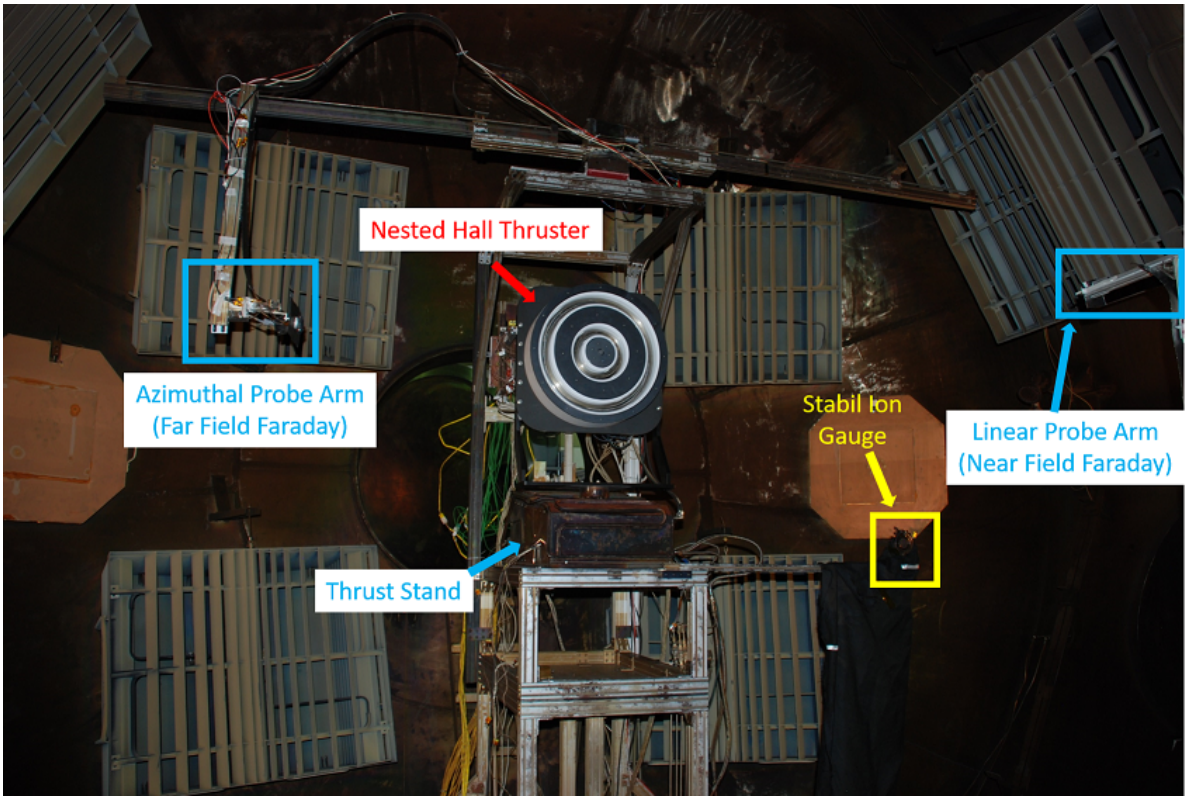

Figure B.5: A picture of the full setup inside the Large Vacuum Test Facility for initial firing

All testing (including anode flow testing) occurred in the Large Vacuum Test Facility at the University of Michigan. The facility was previously described in Chapter 4. Additionally, we used the telemetry system and thrust stand previously described in Chapter 4. During testing, base pressures were below 0.1 μTorr-Xe and typical operational pressures varied from 4 to 16 μTorr-Xe. While nested Hall thrusters can be run off a single power supply, we used an independent commercially-available power supply for each channel. The inner and outer channel power supplies have a maximum output power of 60-kW and 150-kW respectively. The negative side of the power supplies (cathode return) were shorted together at the power feedthrough into the chamber.

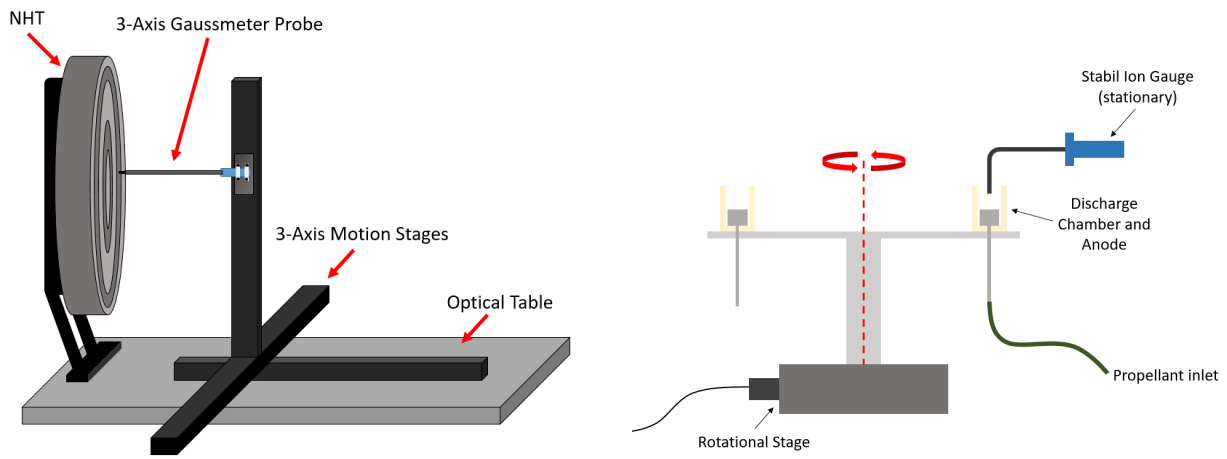

(a) (b)

Figure B.6: Schematic of the setup for both (a) the magnetic field mapping and (b) the anode flow uniformity testing.

B.4.1 Diagnostics

B.4.1.1 Acceptance Testing

Similar to the testing described in Appendix A, in order to verify that both the magnetic circuit was properly constructed and that the field matched our simulations, we mapped the thruster's magnetic field with a 3-axis Gaussmeter and compared the measurements to the simulations. We again detail the exact setup used below. A schematic of the setup can be seen in Figure B.6(a). We took two-dimensional (r-z) maps. Additionally, we measured the maximum centerline radial magnetic field to assess saturation of the circuit. Finally, we performed all these studies in all three magnetic field configurations. In order to pass acceptance testing, we establish the follow criteria: a qualitative agreement of the two-dimensional maps of simulated versus measured fields and a 25% margin on the nominal magnetic field for saturation onset (greater than 5% deviation from linearity).

The second major acceptance test performed was the anode flow uniformity test. The setup for this test can be seen in Figure B.6(b). Azimuthal flow uniformity was assessed by neutral density testing with a Series 370 Stabil Ion Gauge. The discharge chamber,

BN rings and anode were placed on a rotational stage with the ion gauge inlet located radially on channel centerline and axially midway through the discharge chamber. [5] Each anode (inner and outer) were measured at 36 evenly distributed azimuthal points. For the inner channel, we performed these tests at 2 mg/s and 20 mg/s. For the outer channel, we performed these tests at 5 mg/s and 50 mg/s. The dwell time at each test point was 10 seconds. For the inner anode, an acceptable flow uniformity criterion of deviations up to 10% (δp_{max}) from the mean value ($\langle p \rangle$) was used during testing. [**?**] For the outer anode, while the same criterion is desired, this would be particularly challenging at the lower flow rate since the internal volume of the anode is significantly larger. The X3 Hall thruster used deviations of up to 24% from the mean value for the large anodes. [**?**] The middle anode of that thruster exhibited fluctuations of 14.7%. [**?**] Based on this, we relax our criterion from the inner anode to be 20% of the mean value for the low flow case while maintaining a criterion of 10% for the high flow case.

B.4.1.2 Probes

To assess plume symmetry, we used a far-field Faraday probe. The probe had a collector diameter of 6.1 mm and was swept azimuthally from 0 to 180 degrees. To ensure ion saturation, the collector and guard ring were biased to -20 V. Current was measured using a Keithley Series 2400 Sourcemeter.

B.5 Acceptance Testing

In this section, we first present the results from the anode flow uniformity testing and then the results from the magnetic field mapping.

B.5.1 Anode Flow Uniformity

Figure B.7 shows the results of the anode flow uniformity testing. The facility pressure during this testing was between 1 and 10 μTorr-Xe. The inner anode is well within acceptable limits with the largest deviations at low flow being 4.6% and at high flow being 4.0%. For the outer anode, the largest deviations were 15.3% at low flow and 8.4% at high flow. The low flow condition saw higher deviations from the mean than high flow, however this is expected and the outer anode is never expected to run at 5 mg/s. Regardless, all conditions met the acceptance criteria and thus we determined that both anodes passed flow uniformity testing.

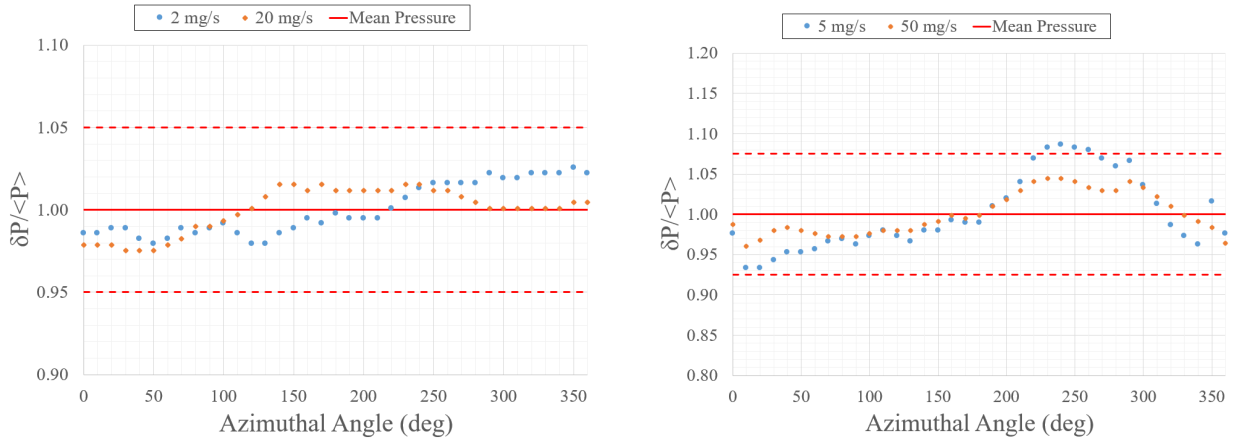

(a) Inner Anode

(b) Outer Anode

Figure B.7: Results of the anode flow uniformity testing for both anodes.

B.5.2 Magnetic Field Testing

Overall, the two-dimensional mapping revealed that each thruster configuration matched the simulation very well. Figure B.8(a) shows the response of the magnetic circuit with increasing inner coil current with a constant coil ratio. In order to facilitate ease of comparison between cases, the inner coil current has been normalized. Note that only simulation data above normalized current of 0.5 is presented. Overall, the results indicate that the circuit is linear up to magnetic fields 50% higher than nominal strengths. This allows for a margin on

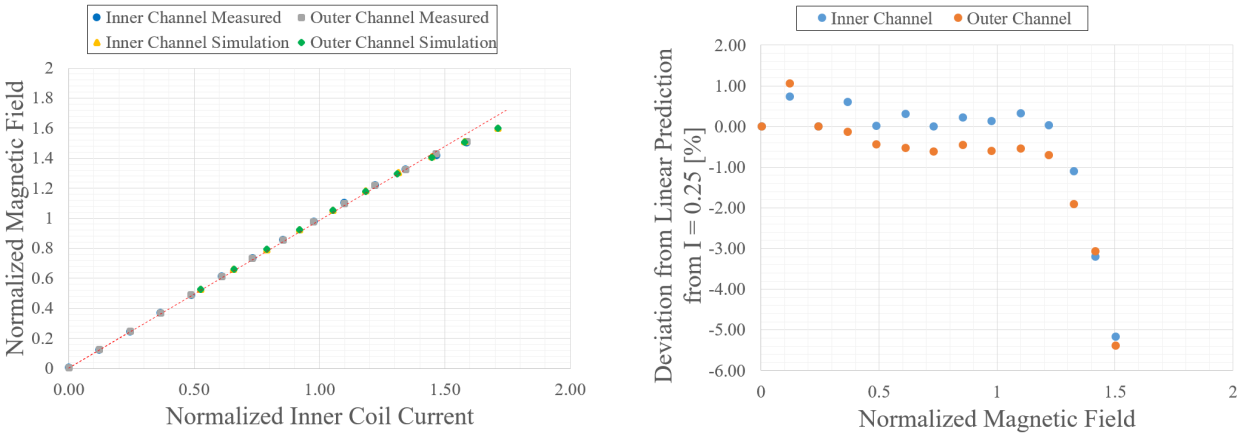

(a) (b)

Figure B.8: Saturation Profile for the Dual Channel Magnetic Field

the strength and expanded research capabilities. Figure B.8(b) shows this more clearly by plotting the departure from linearity versus magnetic field. In order to generate this plot, we predict the strength for a given coil current based on the strength at a normalized inner current of 0.25 (using a ratio). We then compared the predicted value to the actual measured value. This departure does not go above 5% until the normalized magnetic field is above 1.5. It is also critical to note that Figure B.8(a) demonstrates very close agreement with the simulation, particularly in the saturation region. At many of the points, the simulation and experimental data are indistinguishable.

Similarly, Figure B.9 indicates the deviations from linearity for the single channel configurations. These results show that the single channel configurations show less saturation as compared to the dual channel field. This indicates that these fields actually have greater margin than in dual channel mode. This is likely due to less magnetic flux being pushed through the material in single channel mode. Given these results and qualitative observations of the two-dimensional mapping, we ultimately determined that all three thruster configurations pass acceptance testing.

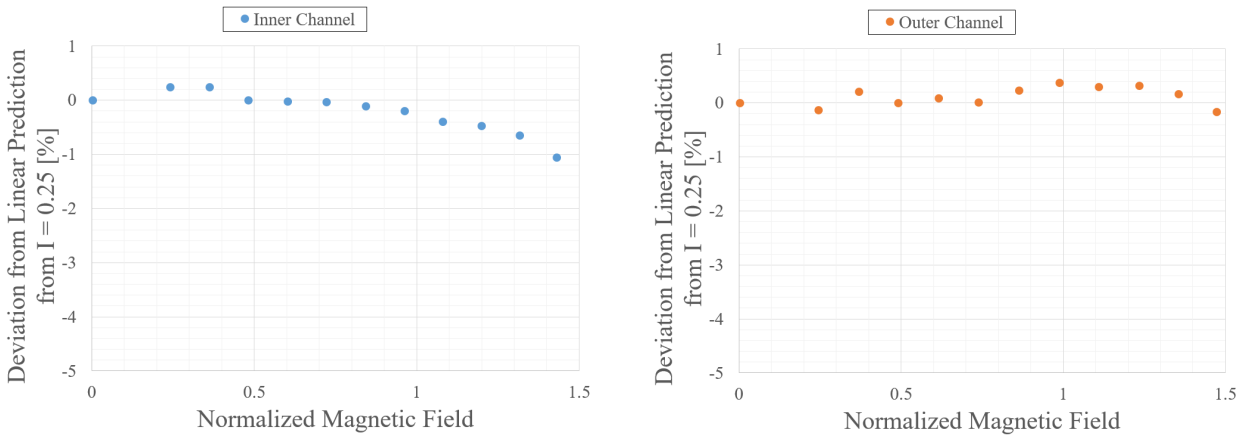

Figure B.9: Saturation profiles for the inner channel only magnetic field (a) and outer channel only magnetic field (b).

B.6 Performance Testing

In this section, we present the initial performance testing of the thruster including evidence of magnetic shielding, current density, oscillation and thrust measurements. Unanticipated challenges in the implementation of a continuous monolithic piece of borosilicate ceramic for the outer channel discharge chamber precluded most outer channel and all dual channel measurements in this initial campaign (discussed more in Sec. B.7). Therefore, we only report inner channel performance.

A picture of the thruster, during first lighting, is shown in Figure B.10. We see both the inner and outer channels running alone here. Qualitatively, the plumes look characteristic of typical Hall thruster plumes.

B.6.1 Magnetic Shielding

Throughout the test campaign, there were many qualitative indications that the channels were magnetically shielded. Typical qualitative indications of magnetic shielding include low luminosity near the walls and carbon build-up on the walls. [**?**, 123] For an unshielded

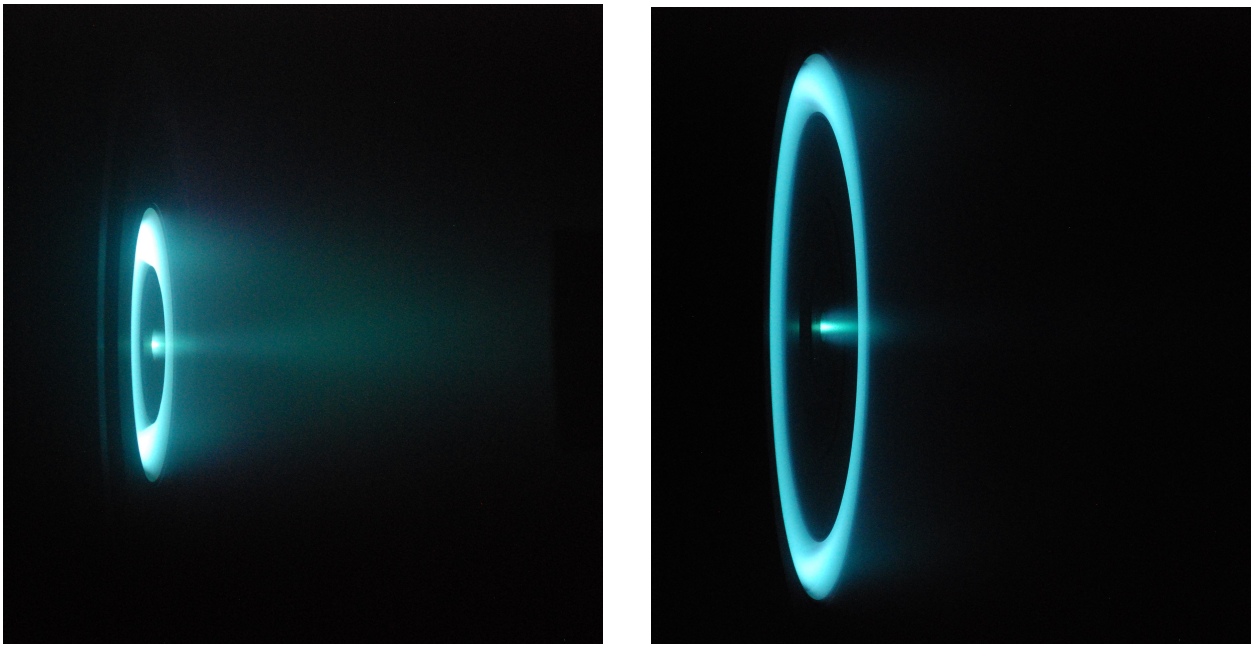

(a) (b)

Figure B.10: A picture of the inner channel running alone at 300 V, 15 A (a) and the outer channel running alone at 300 V, 38.85 A (b). Note, the camera settings are not the same between these two photographs.

thruster, there is high luminescence radially throughout the discharge chamber. However, with a magnetically shielded thruster, a low electron temperature is expected near the wall because the grazing line samples low temperature plasma near the anode and magnetic field lines are approximately isothermal. This low electron temperature then leads to low luminescence. This feature can been seen on the inner channel in Figure B.11(a).

Additionally, for unshielded thrusters, we expect to see carbon deposition (from the downstream beam dump) deep into the discharge chamber. Closer to the exit plane however, the rings should remain white from erosion. For shielded thrusters, the walls would remain coated even near the exit plane. Figure B.11(b) shows a picture of the inner channel after approximately 50 hours of firing. We see that the entirety of the discharge chamber (both inner and outer walls) is coated in carbon, again suggesting that the thruster is magnetically shielded. Additionally, chamfer laser induced fluorescence measurements confirming

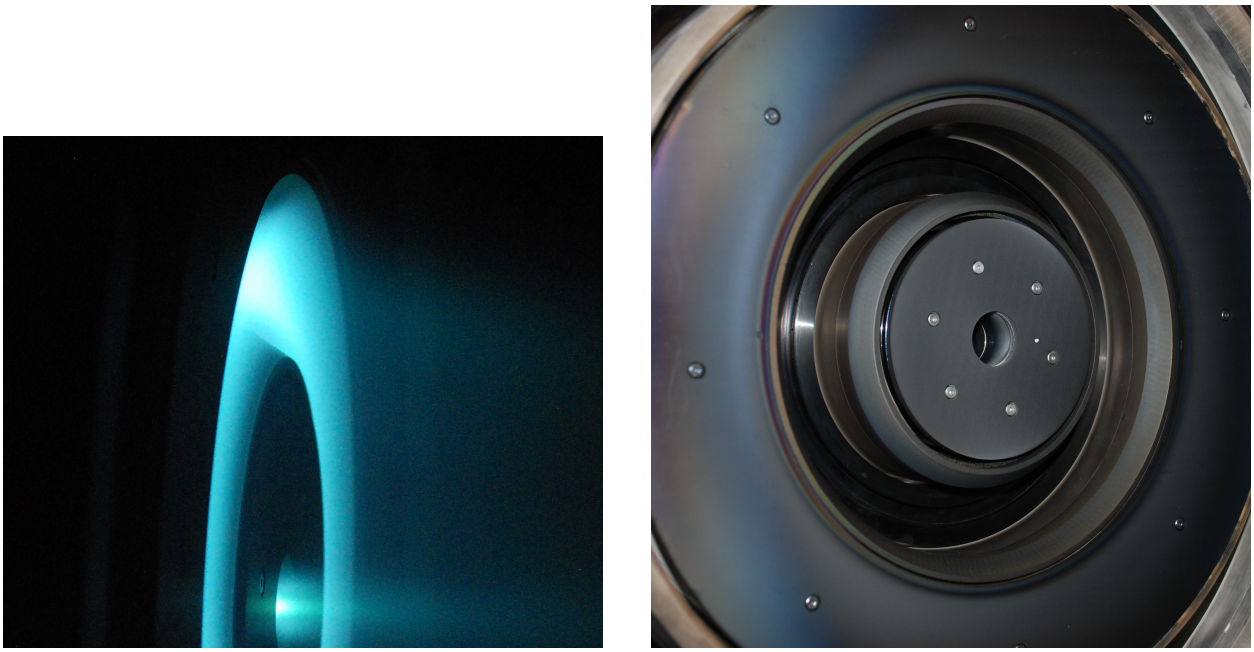

(a) (b)

Figure B.11: A picture of the inner channel running (a) where a region of high light emission can be seen at the center of the channel; near the walls, there is significantly lower light emission. A picture of the inner channel (b) after approximately 50 hours of firing showing carbon buildup over the entire wall.

magnetic shielding were taken and will be published in the near future. We note that these observations alone are not sufficient to claim the thruster is shielded. However, these indications, in combination with the heritage from the H9 and H6MS, give us confidence to say that it is shielded. Finally, while we are unable to assess the shielding of dual channel mode, we are confident that this configuration will also be magnetically shielded based on the magnetic field mapping, heritage, and the indications given in single channel mode.

B.6.2 Oscillations

We characterized the plasma oscillations of each channel. Table B.2 shows the anode current peak-to-peak, discharge voltage peak-to-peak, and the first and second peak frequencies (highest and second highest amplitude) of the power spectrum for each reference firing condition for the inner channel. The peak magnetic field strength was the same for each

Table B.2: Plasma Oscillations for the Inner Channel Reference Firing Conditions

Voltage (V)	Current (A)	Current P2P (A)	I_{P2P}/I_d (%)	Voltage P2P (V)	V_{P2P}/V_d (%)	1^{st} Peak Freq. (kHz)	2^{nd} Peak Freq. (kHz)
300	15	5.2	34.8	23	7.7	43.9	8.4
300	20	6.8	34	27	9	9.3	46.2
400	15	12.5	83.4	48	12	24.8	9.8
500	15	12.5	84.5	55	11	63.1	14.8
600	15	12.1	81.3	53	8.8	66.4	10.8
800	11.25	8.8	78.2	68	8.5	77.6	14.0

condition and the same as the H9. Interestingly, the peak frequency for each condition is higher than a typical Hall thruster breathing mode. We believe this frequency to be associated with the cathode. [**?**, 200] It is possible that these cathode oscillations are stronger than the original H9 measurements because the cathode used is a new cathode with a higher nominal current and flow rate. Thus, at lower currents and flow rates, the cathode oscillations increase. [156] By comparison, the cathode oscillations did not dominate the H9 until 500 V. Based on this evidence, we believe the breathing frequency to be the frequency of the second highest amplitude. These frequencies are similar to the H9 breathing frequencies (between 9 and 18 kHz). [123]

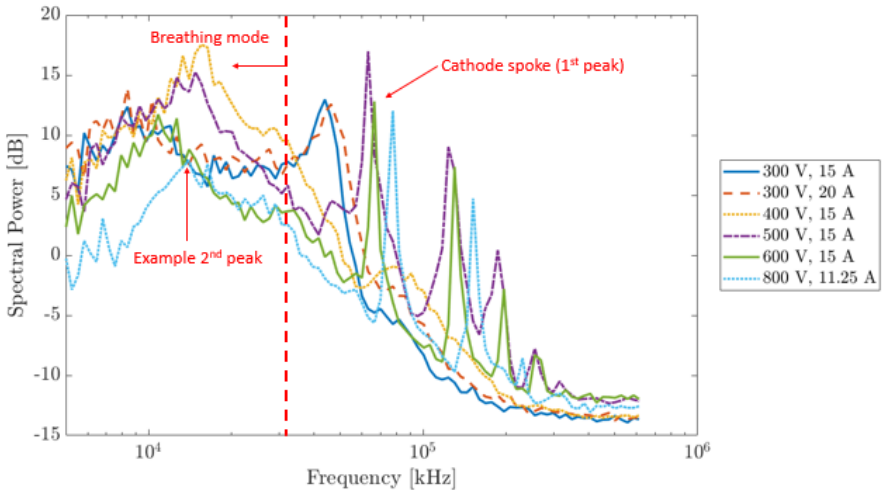

Figure B.12: Power spectrum of the discharge (anode) current oscillations for all reference firing conditions for the inner channel.

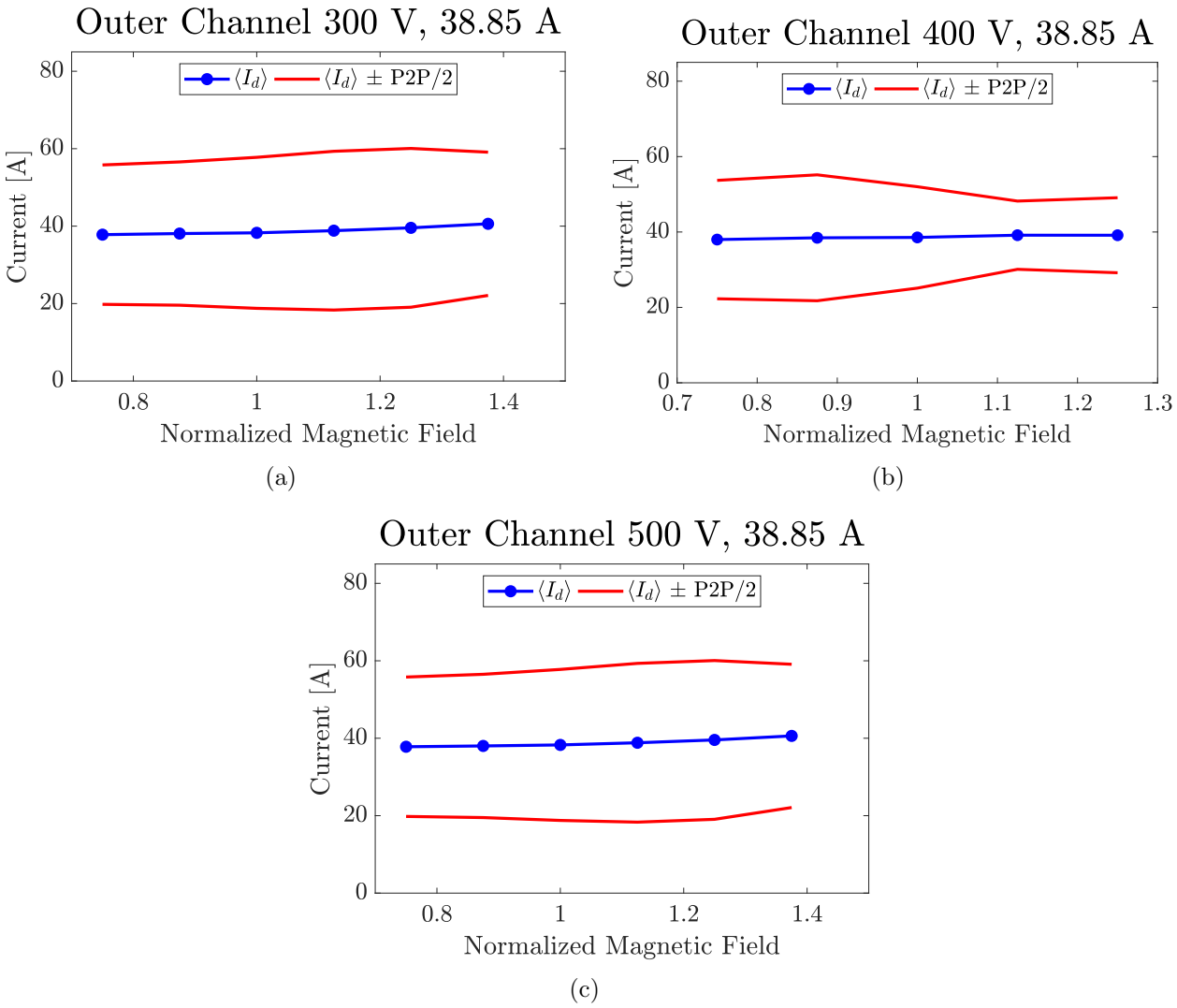

Figure B.13: Magnetic field sweeps for a selection reference firing condition for the outer channel. The plots show mean discharge current and peak-to-peak for varying magnetic field strength.

Figure B.12 shows the power spectrum of these oscillations in which the cathode oscillation and breathing frequency are evident. Similar to the H9, there still exists a clear transition at about 500 V where the cathode oscillations become more peaked. Oscillation data from the outer channel (300-500 V) showed no prominent cathode peak until 500 V; however, the breathing frequency was much higher (19-35 kHz). This emergence of the cathode peak at higher voltages is similar to the behavior of the H9. The lack of cathode oscillations at

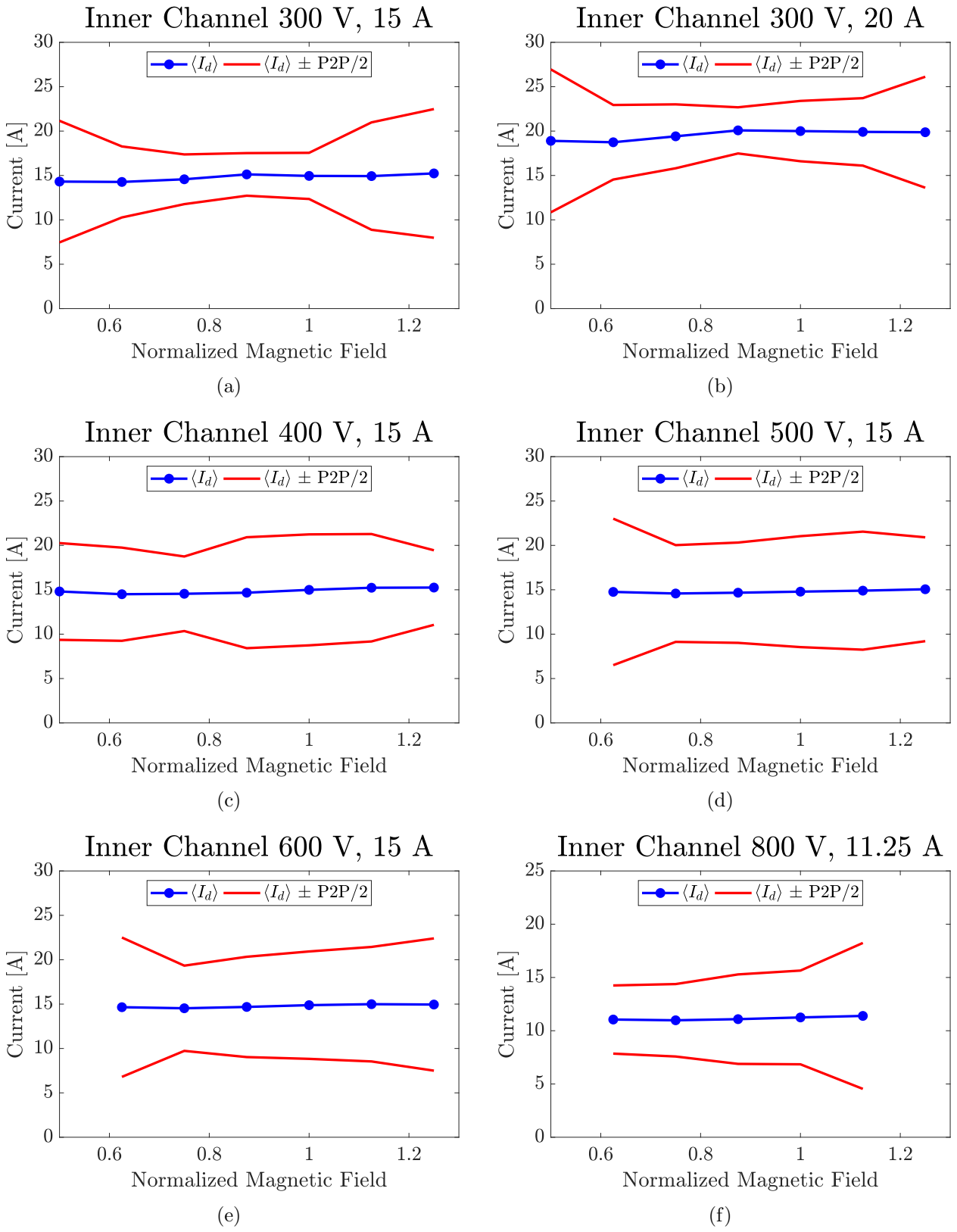

Figure B.14: Magnetic field sweeps for each reference firing condition for the inner channel. The plots show mean discharge current and peak-to-peak for varying magnetic field strength.

low voltage is likely due to the much higher flow rates through the cathode (2.7x at 300 V), which have been shown to damp oscillations. [156]

Finally, Figures B.13 and B.14 plot the mean current and peak-to-peak oscillations for the firing conditions presented here. Overall, we see that the N30 is stable over the RFCs with the highest peak-to-peak amplitude at 101% of the mean current. The dominant frequencies are typical of magnetically shielded Hall thrusters. [**?**, 123, 200] The magnetic field sweeps also show a wide range of magnetic stability margin. [125]

B.6.3 Performance

Once the "nominal" magnetic field had been determine, we performed thrust measurements at each of the RFCs for the inner channel. Table B.3 shows the results from this study. Telemetry shows that the cathode-ground voltage varied from -10.6 to -12.1 V and the body current varied from -0.56 to -1.73 A. The negative sign indicates electron current is collected on the body . Overall, the thrust, efficiency, and specific impulse are in line with other state-of-the-art magnetically shielded thrusters. [**?**,20,123,125] The thrust ranges from 292.1 to 450.6 mN with a peak specific impulse of 2831 seconds at 800 V discharge voltage and a peak efficiency of 65.2% at 600 V.

Table B.3: Thrust and Performance Metrics for the Inner Channel at all RFCs

V_d (V)	I_d (A)	P_d (kW)	Anode (mg/s)	Cathode (mg/s)	$\frac{P_{mag}}{P_d}$	Thrust (mN)	Total I_{sp} (s)	Total Eff	Pressure (μTorr-Xe)
300	15	4500	14.70	1.03	1.60%	292.1	1893	0.593	5.1
300	20	6000	18.30	1.28	1.20%	376.6	1960	0.596	6.3
400	15	6000	15.26	1.07	1.19%	351.2	2189	0.619	5.3
500	15	7500	15.91	1.11	0.94%	406.4	2434	0.641	5.5
600	15	9000	16.00	1.12	0.78%	450.6	2680	0.652	5.6
800	11.25	9000	13.18	0.98	0.82%	392.9	2831	0.603	4.7

B.6.4 Ion Current Density

Figure B.15 shows the far-field ion current density traces for both the inner and outer channels. Qualitatively, for both channels, we see evidence of plume symmetry at each operating point. There are some slight differences (imperceptible) in the height of the two peaks for each case, which can be attributed to variations in neutral density azimuthally as shown in anode flow uniformity measurements. However, the difference in peak height is less than 10% for all traces taken (all six conditions for the inner channel and the three cases presented for the outer channel). These traces indicate that each channel performs as expected across the nominal operating envelope.

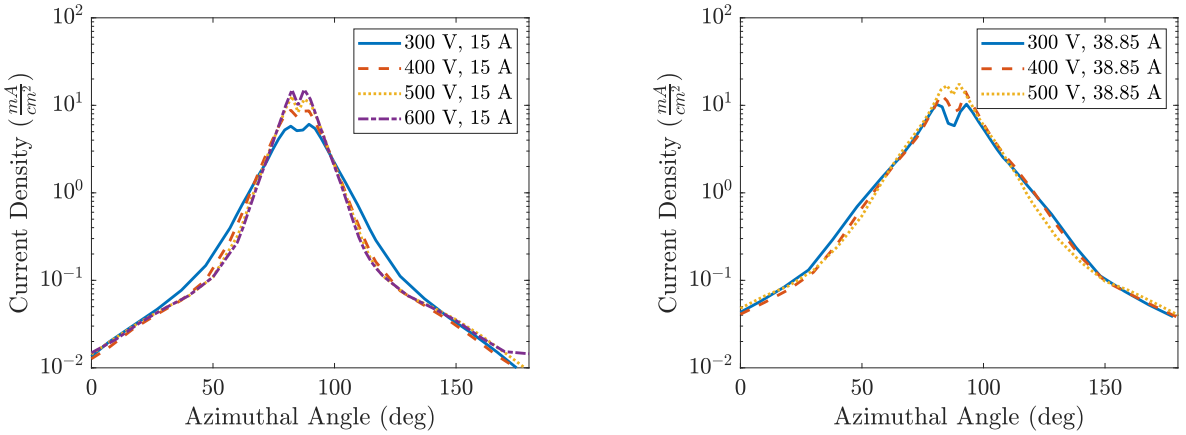

Figure B.15: Ion current density measurements with increasing voltage for the inner channel (a) and outer channel (b) at constant current.

B.7 Discussion

One the key goals of the N30 was to create a nested Hall thruster where the inner channel is geometrically the same as the H9. Thus, we would have the ability to make direct comparisons between the performance of the inner channel in the thruster is various modes

with the H9. As a baseline, we compare the inner channel operating alone and the H9. The differences between these two configurations are the amount of magnetic material present, the thermal environment, and subtle changes to the magnetic field shape in the far-field. The peak magnetic field magnitude was the same. The results of this comparison are seen in Table B.4. The 800 V condition is not presented because data for the H9 at the same settings is not available. Overall, we see that the H9 and the inner channel of the NHT have very similar performance. Almost all values are within their uncertainties. This result indicates two key findings: (1) we were able to reproduce the H9 as the inner channel of an NHT and (2) running a thruster in a different thermal and magnetic material environment does not have drastic impacts on the performance.

Table B.4: Comparison of the inner channel of the N30 and the H9 at five RFCs. Standard error for the NHT results was 3%.

	Thrust (mN)			Total I_{sp} (s)			Total Efficiency		
Condition	H9	NHT	% Diff	H9	NHT	% Diff	H9	NHT	% Diff
300V, 15A	286.8	292.1	1.8%	1914	1893	-1.1%	0.598	0.593	-0.8%
300V, 20A	371.8	376.6	1.3%	1987	1960	-1.4%	0.603	0.596	-1.1%
400V, 15A	345.1	351.2	1.8%	2196	2189	-0.3%	0.619	0.619	0.1%
500V, 15A	392.8	406.4	3.5%	2422	2434	0.5%	0.622	0.641	3.0%
600V, 15A	435.6	450.6	3.4%	2652	2680	1.0%	0.629	0.652	3.5%

While there are no drastic differences between the H9 and the NHT inner channel, there are a few key variations to note. The body current collected is notably higher for the NHT than the H9. This is not surprising as the NHT has a much larger area to collect body current over due to the presence of another channel. Additionally, the mass flow rates (2-3%) and thrust (1.3-3.5%) were slightly higher for the NHT than the H9. Regardless, the performance differences are on the order of the uncertainty of the measurements. That is why, despite having slightly higher thrust for all conditions, the specific impulse and efficiency see both increase and decreases between the two thrusters. However, it is important to note that the NHT inner channel studies occurred at 60-70% lower pressures

than the H9 due to differences in pumping speed between the two tests. Based on H6MS results, changes in pressure should not lead to large changes in thrust; however, it can have a more noticeable impact on total flow. Therefore, at equal pressures, the flow rates would likely be the same [28] Should this be true, when operating at the same pressures, there may exist a 2-3% increase in specific impulse and efficiency for the inner channel of the NHT as compared to the H9 across the board. This is likely due to the thermal differences, where the NHT was, on average, operating at approximately 200 °C less than the H9. Additionally, subtle changes in the far-field magnetic field could impact the location of the acceleration region and the cathode coupling. Movement of the acceleration region, with pressure, could account for differences in mass flow rates as well.

The N30 is a significant step for nested Hall thruster technology, and we showed here state-of-the-art performance and magnetic shielding. However, there do remain some key challenges. First and foremost, we have yet to run this thruster up to full power. Based on heritage arguments and some basic thermal calculations, we believe the thruster will be thermally stable over its entire operating range. However, it is challenging to know whether we will encounter thermal issues at 33 kW until we test at this condition. While we took measured steps to improve the thermal environment, the compactness of the thruster will always make thermal stability a difficult endeavor. Finally, a large area for improvement lies in discharge chamber materials. As mentioned earlier, challenges with the discharge chamber precluded most testing with the outer channel. Likely, this was due to thermal expansion mismatches and tolerance-ing of the machined parts. For much larger parts (such as this discharge chamber compared to the inner), small issues with either of these can have much larger consequences due to accumulated errors on large diameters. We believe moving away from a single monolithic piece of ceramic would be advantageous. Due to advances in magnetic field topologies, graphite discharge chamber walls are now feasible. [62] Applying these new materials and designs to large channels in nested Hall thrusters is critical for

future next generation missions from a cost and manufacturing perspective.

The main goals of the N30 were to design and implement a nested-channel thruster with a magnetic shielding topology, capable of 25-50 kW of discharge power. Additionally, we wanted the inner channel to share geometry with the H9 to enable channel interaction studies, to provide a NHT testbed, and to make the design modular for ease of diagnostic and mechanical changes. Considering the work presented here, we believe all of these goals have been accomplished. Indeed, all expect the discharge power capabilities have been demonstrated and considering the power levels each individual channel has been capable of, there exist no indications that this last goal has not been achieved.

APPENDIX C

Example Thrust Stand Calibration

In this Appendix, we provide an example thrust stand calibration. First, we show the raw signal followed by the corresponding calibration. These data were taken with the H9 installed on the thrust stand with extra applied mass during validation of the new configuration for the N30.

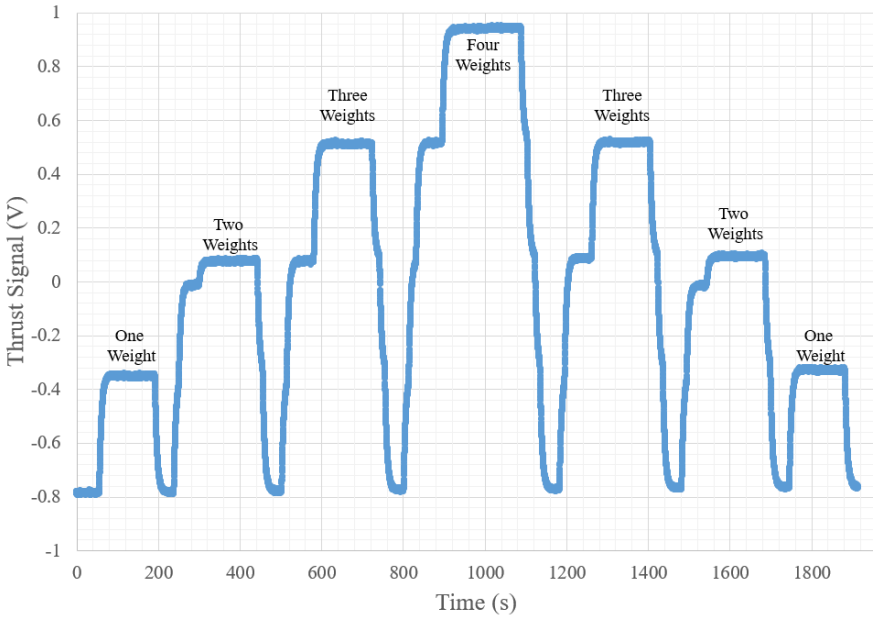

Figure C.1: Thrust signal versus time during calibration. The dropping of each weight is seen. The thrust stand returns to "zero" after each successive weight to provide a reference signal.

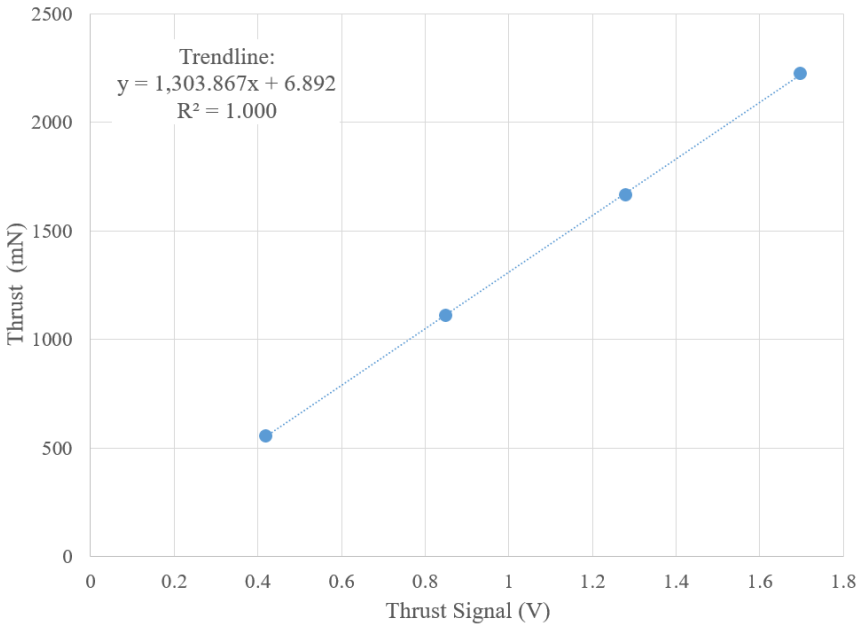

Figure C.2: The resulting calibration for thrust versus signal from the calibration. The line of best fit shows there is perfect correlation between the signal and the thrust.

BIBLIOGRAPHY

[1] Liang, R., *The Combination of Two Concentric Discharge Channels into a Nested Hall-Effect Thruster*, Ph.D. Dissertation, University of Michigan, Ann Arbor, MI, 2013.

[2] Hofer, R. R. and Gallimore, A. D., "High-Specific Impulse Hall Thrusters, Part 2: Efficiency Analysis," *Journal of Propulsion and Power*, Vol. 22, No. 4, 2006, pp. 732–740.

[3] Mikellides, I. G., Katz, I., Hofer, R. R., and Goebel, D. M., "Magnetic shielding of a laboratory Hall thruster. I. Theory and validation," *Journal of Applied Physics*, Vol. 115, No. 4, 2014, pp. 043303.

[4] Brophy, J., Gershman, R., Strange, N., Landau, D., Merrill, R., and Kerslake, T., "300-kW solar electric propulsion system configuration for human exploration of near-earth asteroids," *47th AIAA/ASME/SAE/ASEE Joint Propulsion Conference & Exhibit*, 2011, p. 5514.

[5] Reid, B. M., *The Influence of Neutral Flow Rate in the Operation of Hall Thrusters.*, Ph.D. thesis, 2009.

[6] Cusson, S. E., Georgin, M. P., Dragnea, H. C., Dale, E. T., Dhaliwal, V., Boyd, I. D., and Gallimore, A. D., "On channel interactions in nested Hall thrusters," *Journal of Applied Physics*, Vol. 123, No. 13, 2018, pp. 133303.

[7] "In-Space Propulsion Systems Roadmap," *National Aeronautics and Space Administration, Office of the Chief Technologist*, 2015.

[8] Goebel, D. M. and Katz, I., *Fundamentals of electric propulsion: ion and Hall thrusters*, Vol. 1, John Wiley & Sons, 2008.

[9] Kim, V., "Main physical features and processes determining the performance of stationary plasma thrusters," *Journal of Propulsion and Power*, Vol. 14, No. 5, 1998, pp. 736–743.

[10] Ahedo, E., Martınez-Cerezo, P., and Martınez-Sánchez, M., "One-dimensional model of the plasma flow in a Hall thruster," *Physics of Plasmas*, Vol. 8, No. 6, 2001, pp. 3058–3068.

[11] Manzella, D., Yim, J., and Boyd, I., "Predicting Hall thruster operational lifetime," *40th AIAA Joint Propulsion Conf., Fort Lauderdale, FL*, 2004.

[12] Gamero-Castano, M. and Katz, I., "Estimation of Hall thruster erosion using HPHall," 2005.

[13] Abgaryan, V., Kaufman, H., Kim, V., Ovsyanko, D., Shkarban, I., Semenov, A., Sorokin, A., and Zhurin, V., "Calculation analysis of the erosion of the discharge chamber walls and their contamination during prolonged SPT operation," *Proc. 30th Joint Propulsion Conference Indianapolis, IN, AIAA*, 1994, pp. 94–2859.

[14] Manzella, D., "Low cost electric propulsion thruster for deep space robotic missions," *2007 NASA Science Technology Conference*, 2007, pp. 07–0116.

[15] Garrigues, L., Hagelaar, G., Bareilles, J., Boniface, C., and Boeuf, J., "Model study of the influence of the magnetic field configuration on the performance and lifetime of a Hall thruster," *Physics of Plasmas*, Vol. 10, No. 12, 2003, pp. 4886–4892.

[16] Morozov, A., "The conceptual development of stationary plasma thrusters," *Plasma Physics Reports*, Vol. 29, No. 3, 2003, pp. 235–250.

[17] Mazouffre, S., Dannenmayer, K., and Pérez-Luna, J., "Examination of plasma-wall interactions in Hall effect thrusters by means of calibrated thermal imaging," *Journal of Applied Physics*, Vol. 102, No. 2, 2007, pp. 023304.

[18] Mikellides, I. G., Katz, I., Hofer, R. R., Goebel, D. M., De Grys, K., and Mathers, A., "Magnetic shielding of the channel walls in a Hall plasma accelerator," *Physics of Plasmas*, Vol. 18, No. 3, 2011, pp. 033501.

[19] Mikellides, I. G., Katz, I., Hofer, R. R., and Goebel, D. M., "Magnetic shielding of walls from the unmagnetized ion beam in a Hall thruster," *Applied Physics Letters*, Vol. 102, No. 2, 2013, pp. 023509.

[20] Hofer, R. R., Goebel, D. M., Mikellides, I. G., and Katz, I., "Magnetic shielding of a laboratory Hall thruster. II. Experiments," *Journal of Applied Physics*, Vol. 115, No. 4, 2014, pp. 043304.

[21] Huang, W., Kamhawi, H., and Haag, T., "Facility effect characterization test of NASAs HERMes Hall thruster," *52nd AIAA/SAE/ASEE Joint Propulsion Conference*, 2016, p. 4828.

[22] Randolph, T., Kim, V., Kaufman, H., Kozubsky, K., Zhurin, V., and Day, M., "Facility effects on stationary plasma thruster testing," *23rd International Electric Propulsion Conference*, 1993, pp. 1993–093.

[23] Kamhawi, H., Haag, T., Huang, W., Yim, J., Herman, D. A., Peterson, P. Y., Williams, G., Gilland, J., Hofer, R. R., and Mikellides, I. G., "Performance, Facility Pressure Effects, and Stability Characterization Tests of NASAs 12.5-kW Hall Effect Rocket with Magnetic Shielding Thruster," *52nd AIAA/SAE/ASEE Joint Propulsion Conference*, 2016, p. 4826.

[24] Hofer, R. R., Peterson, P. Y., and Gallimore, A. D., "Characterizing vacuum facility backpressure effects on the performance of a Hall thruster," IEPC-01-045, 27th International Electric Propulsion Conference, Pasadena, CA, 2001.

[25] Brown, D. L. and Gallimore, A. D., "Evaluation of facility effects on ion migration in a Hall thruster plume," *Journal of Propulsion and Power*, Vol. 27, No. 3, 2011, pp. 573–585.

[26] Nakles, M. and Hargus, W., "Background pressure effects on internal and near-field ion velocity distribution of the BHT-600 Hall thruster," *44th AIAA/ASME/SAE/ASEE Joint Propulsion Conference & Exhibit*, 2008, p. 5101.

[27] Cusson, S. E., Dale, E. T., Jorns, B. A., and Gallimore, A. D., "Acceleration region dynamics in a magnetically shielded Hall thruster," *Physics of Plasmas*, Vol. 26, No. 2, 2019, pp. 023506.

[28] Hofer, R. R. and Anderson, J. R., "Finite pressure effects in magnetically shielded Hall thrusters," *50th AIAA/ASME/SAE/ASEE Joint Propulsion Conference*, 2014, p. 3709.

[29] Ahedo, E., "Plasmas for space propulsion," *Plasma Physics and Controlled Fusion*, Vol. 53, No. 12, 2011, pp. 124037.

[30] Hoskins, W. A., Cassady, R. J., Morgan, O., Myers, R. M., Wilson, F., King, D. Q., and DeGrys, K., "30 years of electric propulsion flight experience at Aerojet Rocketdyne," *33rd International Electric Propulsion Conference*, 2013, pp. 1–12.

[31] Morozov, A. and Savelyev, V., "Fundamentals of stationary plasma thruster theory," *Reviews of plasma physics*, Springer, 2000, pp. 203–391.

[32] Kaufman, H. R., "Technology of closed-drift thrusters," *AIAA journal*, Vol. 23, No. 1, 1985, pp. 78–87.

[33] Esipchuk, Y. V. and Tilinin, G., "Drift instability in a Hall-current plasma accelerator," *Sov. Phys.-Tech. Phys.(Engl. Transl.);(United States)*, Vol. 21, No. 4, 1976.

[34] Choueiri, E. Y., "Fundamental difference between the two Hall thruster variants," *Physics of Plasmas*, Vol. 8, No. 11, 2001, pp. 5025–5033.

[35] Oleson, S., "Advanced electric propulsion for space solar power satellites," *35th AIAA Joint Propulsion Conference, Los Angeles, CA*, 1999.

[36] Oleson, S. and Sankovic, J., "Advanced Hall electric propulsion for future in-space transportation," *Spacecraft Propulsion*, Vol. 465, 2000, p. 717.

[37] Jacobson, D., John, J., Manzella, D., and Peterson, P., "An Overview of Hall Thruster Development at NASA's John H. Glenn Research Center," *41st AIAA/ASME/SAE/ASEE Joint Propulsion Conference & Exhibit*, 2005, p. 4242.

[38] Jacobson, D., Manzella, D., Hofer, R., and Peterson, P., "NASA's 2004 Hall Thruster Program," *40th AIAA/ASME/SAE/ASEE Joint Propulsion Conference and Exhibit*, 2004, p. 3600.

[39] Tahara, H., Nikai, Y., Yasui, T., and Yoshikawa, T., "Hall thruster research at Osaka University," *35th Joint Propulsion Conference and Exhibit*, 1999, p. 2570.

[40] Bouchoule, A., Cadiou, A., Héron, A., Dudeck, M., and Lyszyk, M., "An overview of the French research program on plasma thrusters for space applications," *Contributions to plasma Physics*, Vol. 41, No. 6, 2001, pp. 573–588.

[41] Darnon, F., Arrat, D., d'Escrivan, S., Chesta, E., and Pillet, N., "Overview of electric propulsion activities in France," *43rd AIAA/ASME/SAE/ASEE Joint Propulsion Conference & Exhibit*, 2007, p. 5165.

[42] Gonzalez, J. and Saccoccia, G., "ESA electric propulsion activities," *32nd International Electric Propulsion Conference*, Vol. 2, 2011.

[43] Brown, D. L., Beal, B. E., and Haas, J. M., "Air Force Research Laboratory high power electric propulsion technology development," *2010 IEEE Aerospace Conference*, IEEE, 2010, pp. 1–9.

[44] Kaufman, H. R., "Technology of electron-bombardment ion thrusters," *Advances in Electronics and Electron Physics*, Vol. 36, Elsevier, 1975, pp. 265–373.

[45] Kozubskii, K., Murashko, V., Rylov, Y. P., Trifonov, Y. V., Khodnenko, V., Kim, V., Popov, G., and Obukhov, V., "Stationary plasma thrusters operate in space," *Plasma Physics Reports*, Vol. 29, No. 3, 2003, pp. 251–266.

[46] Goebel, D. M., Watkins, R. M., and Jameson, K. K., "LaB6 hollow cathodes for ion and Hall thrusters," *Journal of Propulsion and Power*, Vol. 23, No. 3, 2007, pp. 552–558.

[47] Boeuf, J.-P., "Tutorial: Physics and modeling of Hall thrusters," *Journal of Applied Physics*, Vol. 121, No. 1, 2017, pp. 011101.

[48] Raitses, Y., Ashkenazy, J., and Guelman, M., "Propellant utilization in Hall thrusters," *Journal of Propulsion and Power*, Vol. 14, No. 2, 1998, pp. 247–253.

[49] Zhurin, V., Kaufman, H., and Robinson, R., "Physics of closed drift thrusters," *Plasma Sources Science and Technology*, Vol. 8, No. 1, 1999, pp. R1.

[50] Raitses, Y., Guelman, M., Ashkenazy, J., and Appelbaum, G., "Orbit transfer with a variable thrust Hall thruster under drag," *Journal of Spacecraft and Rockets*, Vol. 36, No. 6, 1999, pp. 875–881.

[51] Oleson, S., "Mission advantages of constant power, variable Isp electrostatic thrusters," *36th AIAA/ASME/SAE/ASEE Joint Propulsion Conference and Exhibit*, 2000, p. 3413.

[52] Beal, B., Gallimore, A., Morris, D., Davis, C., and Lemmer, K., "Development of an annular helicon source for electric propulsion applications," *42nd AIAA/ASME/SAE/ASEE Joint Propulsion Conference & Exhibit*, 2006, p. 4841.

[53] Beal, B. and Gallimore, A., "Development of the linear gridless ion thruster," *37th Joint Propulsion Conference and Exhibit*, 2001, p. 3649.

[54] Gallimore, A., Reichenbacher, M., Marrese, C., Kim, S.-W., and Foster, J., "Preliminary characterization of a low power end-Hall thruster," *30th Joint Propulsion Conference and Exhibit*, 1994, p. 3012.

[55] Hofer, R. and Gallimore, A., "The Role of Magnetic Field Topography in Improving the Performance of a High Voltage Hall Thruster," *38th AIAA/ASME/SAE/ASEE Joint Propulsion Conference & Exhibit*, 2002, p. 4111.

[56] Hofer, R. R., *Development and characterization of high-efficiency, high-specific impulse xenon Hall thrusters*, Ph.D. thesis, University of Michigan, 2004.

[57] Garner, C., Brophy, J., Polk, J., and Pless, L., "A 5,730-hr cyclic endurance test of the SPT-100," *31st Joint Propulsion Conference and Exhibit*, 1995, p. 2667.

[58] Peterson, P., Jacobson, D., Manzella, D., and John, J., "The performance and wear characterization of a high-power high-Isp NASA Hall thruster," *41st AIAA/ASME/SAE/ASEE Joint Propulsion Conference & Exhibit*, 2005, p. 4243.

[59] Mikellides, I. G. and Ortega, A. L., "Numerical Simulations of a 100-kW Class Nested Hall Thruster with the 2-D Axisymmetric Code Hall2De," *35th International Electric Propulsion Conference, IEPC-2017-220, Electric Rocket Propulsion Society, Atlanta, GA*, 2017.

[60] Cheng, S. Y.-M., *Modeling of Hall thruster lifetime and erosion mechanisms*, Ph.D. thesis, Massachusetts Institute of Technology, 2007.

[61] de Grys, K., Mathers, A., Welander, B., and Khayms, V., "Demonstration of 10,400 hours of operation on 4.5 kw qualification model hall thruster," *46th AIAA/ASME/SAE/ASEE Joint Propulsion Conference & Exhibit*, 2010, p. 6698.

[62] Goebel, D. M., Hofer, R. R., Mikellides, I. G., Katz, I., Polk, J. E., and Dotson, B. N., "Conducting wall Hall thrusters," *IEEE Transactions on Plasma Science*, Vol. 43, No. 1, 2014, pp. 118–126.

[63] Spektor, R. and Tighe, W. G., "Laser Induced Fluorescence Measurements in a Hall Thruster as a Function of Background Pressure," *52nd AIAA/SAE/ASEE Joint Propulsion Conference*, 2016, p. 4624.

[64] Hofer, R. R., Johnson, L. K., Goebel, D. M., and Wirz, R. E., "Effects of internally mounted cathodes on Hall thruster plume properties," *IEEE Transactions on Plasma Science*, Vol. 36, No. 5, 2008, pp. 2004–2014.

[65] Herman, D. A., Tofil, T. A., Santiago, W., Kamhawi, H., Polk, J. E., Snyder, J. S., Hofer, R. R., Picha, F. Q., Jackson, J., and Allen, M., "Overview of the Development and Mission Application of the Advanced Electric Propulsion System (AEPS)," 2018.

[66] Crusan, J. C., Smith, R. M., Craig, D. A., Caram, J. M., Guidi, J., Gates, M., Krezel, J. M., and Herrmann, N. B., "Deep space gateway concept: Extending human presence into cislunar space," *2018 IEEE Aerospace Conference*, IEEE, 2018, pp. 1–10.

[67] McGuire, M. L., Burke, L. M., McCarty, S. L., Hack, K. J., Whitley, R. J., Davis, D. C., and Ocampo, C., "Low thrust cis-lunar transfers using a 40 KW-class solar electric propulsion spacecraft," 2017.

[68] Frisbee, R. and Hoffman, N., "Electric propulsion options for Mars cargo missions," *32nd Joint Propulsion Conference and Exhibit*, 1996, p. 3173.

[69] Andrews, D. and Wetzel, E., "Solar Electric SpaceTug to Support Moon and Mars Exploration Missions," *Space 2005*, 2005, p. 6739.

[70] Manzella, D. H. and Hack, K., "High-power Solar electric propulsion for future NASA missions," *50th AIAA/ASME/SAE/ASEE Joint Propulsion Conference*, 2014, p. 3718.

[71] Jackson, J., Allen, M., Myers, R., Hoskins, A., Soendker, E., Welander, B., Tolentino, A., Hablitzel, S., Hall, S., Gallimore, A., et al., "100 kW Nested Hall Thruster System Development," 2017.

[72] Hofer, R. R. and Randolph, T. M., "Mass and cost model for selecting thruster size in electric propulsion systems," *Journal of Propulsion and Power*, Vol. 29, No. 1, 2012, pp. 166–177.

[73] Brophy, J. R., "NASAs Deep Space 1 ion engine (plenary)," *Review of Scientific Instruments*, Vol. 73, No. 2, 2002, pp. 1071–1078.

[74] Koppel, C. R. and Estublier, D., "The SMART-1 Hall effect thruster around the moon: In flight experience," *29th International electric propulsion conference*, 2005, p. 119.

[75] NISHIYAMA, K., HOSODA, S., UENO, K., TSUKIZAKI, R., and KUNINAKA, H., "Development and testing of the Hayabusa2 ion engine system," *Transactions of the Japan Society For Aeronautical and Space Sciences, Aerospace Technology Japan*, Vol. 14, No. ists30, 2016, pp. Pb_131–Pb_140.

[76] Anselmi, A. and Scoon, G. E., "BepiColombo, ESA's Mercury cornerstone mission," *Planetary and Space Science*, Vol. 49, No. 14-15, 2001, pp. 1409–1420.

[77] Oh, D., Collins, S., Goebel, D., Hart, B., Lantoine, G., Snyder, S., Whiffen, G., Elkins-Tanton, L., Lord, P., Pirkl, Z., et al., "Development of the Psyche Mission for NASA's Discovery Program," *IEPC-2017-153, 35th International Electric Propulsion Conference*, 2017.

[78] Strange, N., Merrill, R., Landau, D., Drake, B., Brophy, J., and Hofer, R., "Human missions to phobos and deimos using combined chemical and solar electric propulsion," *47th AIAA/ASME/SAE/ASEE Joint Propulsion Conference & Exhibit*, 2011, p. 5663.

[79] Díaz, F. C., Carr, J., Johnson, L., Johnson, W., Genta, G., and Maffione, P. F., "Solar electric propulsion for human mars missions," *Acta Astronautica*, Vol. 160, 2019, pp. 183–194.

[80] Taylor, R., "Prometheus Project final report," Tech. rep., National Aeronautics and Space Administration, 2005.

[81] Oleson, S., "Electric Propulsion Technology Development for the Jupiter Icy Moon Orbiter Project," *40th AIAA/ASME/SAE/ASEE Joint Propulsion Conference and Exhibit*, 2004, p. 3449.

[82] Strange, N., Landau, D., Hofer, R., Snyder, J., Randolph, T., Campagnola, S., Szabo, J., and Pote, B., "Solar electric propulsion gravity-assist tours for Jupiter missions," *AIAA/AAS Astrodynamics Specialist Conference*, 2012, p. 4518.

[83] Hofer, R. R., "High-Efficiency Nested Hall Thrusters for Robotic Solar System Exploration," 2013.

[84] Bennett, G. L., Hemler, R. J., and Schock, A., "Space nuclear power-an overview," *Journal of propulsion and power*, Vol. 12, No. 5, 1996, pp. 901–910.

[85] Gibson, M. A., Oleson, S. R., Poston, D. I., and McClure, P., "NASA's Kilopower reactor development and the path to higher power missions," *2017 IEEE Aerospace Conference*, IEEE, 2017, pp. 1–14.

[86] Huang, W., Kamhawi, H., and Haag, T., "Effect of background pressure on the performance and plume of the hivhac hall thruster," 2013.

[87] Walker, J. A., Frieman, J. D., Walker, M. L., Khayms, V., King, D., and Peterson, P. Y., "Electrical facility effects on Hall-effect-thruster cathode coupling: discharge oscillations and facility coupling," *Journal of Propulsion and Power*, Vol. 32, No. 1, 2016, pp. 844–855.

[88] Cusson, S. E., Jorns, B., and Gallimore, A., "Simple Model for Cathode Coupling Voltage Versus Background Pressure in a Hall Thruster," *53rd AIAA/SAE/ASEE Joint Propulsion Conference*, 2017, p. 4889.

[89] Tilley, D., de Grys, K., and Myers, R., "Hall thruster-cathode coupling," *35th Joint Propulsion Conference and Exhibit*, 1999, p. 2865.

[90] Sommerville, J. and King, L., "Effect of Cathode Position on Hall-Effect Thruster Performance and Near-Field Plume Properties," *44th AIAA/ASME/SAE/ASEE Joint Propulsion Conference & Exhibit*, 2007, p. 4996.

[91] R. Walker, M. L. and Gallimore, A. D., "Hall thruster cluster operation with a shared cathode," *Journal of Propulsion and Power*, Vol. 23, No. 3, 2007, pp. 528–536.

[92] McDonald, M. and Gallimore, A., "Cathode position and orientation effects on cathode coupling in a 6-kW Hall thruster," *31st International Electric Propulsion Conference*, Vol. 113, 2009.

[93] Jameson, K. K., Goebel, D. M., Hofer, R. R., and Watkins, R. M., "Cathode coupling in Hall thrusters," *30th International Electric Propulsion Conference*, 2007, pp. 2007–278.

[94] Diamant, K. D., Liang, R., and Corey, R. L., "The effect of background pressure on SPT-100 Hall thruster performance," *50th AIAA/ASME/SAE/ASEE Joint Propulsion Conference*, 2014, p. 3710.

[95] Byers, D. and Dankanich, J. W., "A review of facility effects on Hall effect thrusters," *31st International Electric Propulsion Conference*, 2009, pp. 2009–076.

[96] Sankovic, J. M., Hamley, J. A., and Haag, T. W., "Performance evaluation of the Russian SPT-100 thruster at NASA LeRC," 1994.

[97] Nakles, M. R. and Hargus, W. A., "Background pressure effects on ion velocity distribution within a medium-power Hall thruster," *Journal of Propulsion and Power*, Vol. 27, No. 4, 2011, pp. 737–743.

[98] Raitses, Y., Parker, J., Davis, E., and Fisch, N., "Background gas pressure effects in the cylindrical Hall thruster," *46th AIAA/ASME/SAE/ASEE Joint Propulsion Conference & Exhibit*, 2010, p. 6775.

[99] Estublier, D. L., "The SMART-1 spacecraft potential investigations," *IEEE Transactions on Plasma Science*, Vol. 36, No. 5, 2008, pp. 2262–2270.

[100] Lopez Ortega, A., Mikellides, I. G., and Jorns, B., "First-principles modeling of the IAT-driven anomalous resistivity in hollow cathode discharges II: Numerical simulations and comparison with measurements," *52nd AIAA/SAE/ASEE Joint Propulsion Conference*, 2016, p. 4627.

[101] Jorns, B., Lopez Ortega, A., and Mikellides, I. G., "First-principles modelling of the IAT-driven anomalous resistivity in hollow cathode discharges I: Theory," *52nd AIAA/SAE/ASEE Joint Propulsion Conference*, 2016, p. 4626.

[102] Jorns, B., Dodson, C. A., Anderson, J. R., Goebel, D. M., Hofer, R. R., Sekerak, M. J., Lopez Ortega, A., and Mikellides, I. G., "Mechanisms for pole piece erosion in a 6-kW magnetically-shielded Hall thruster," *52nd AIAA/SAE/ASEE Joint Propulsion Conference*, 2016, p. 4839.

[103] Ortega, A. L., Mikellides, I. G., and Chaplin, V. H., "Numerical Simulations for the Assessment of Erosion in the 12.5-kW Hall Effect Rocket with Magnetic Shielding (HERMeS)," *35th International Electric Propulsion Conference, IEPC-2017*, Vol. 154, 2017.

[104] Hargus Jr, W. and Cappelli, M., "Laser-induced fluorescence measurements of velocity within a Hall discharge," *Applied Physics B*, Vol. 72, No. 8, 2001, pp. 961–969.

[105] MacDonald-Tenenbaum, N., Pratt, Q., Nakles, M., Pilgram, N., Holmes, M., and Hargus Jr, W., "Background Pressure Effects on Ion Velocity Distributions in an SPT-100 Hall Thruster," *Journal of Propulsion and Power*, Vol. 35, No. 2, 2019, pp. 403–412.

[106] Haas, J., Gulczinski, III, F., Gallimore, A., Spanjers, G., and Spores, R., "Performance characteristics of a 5 kW laboratory Hall thruster," *34th AIAA/ASME/SAE/ASEE Joint Propulsion Conference and Exhibit*, 1998, p. 3503.

[107] Hofer, R. and Gallimore, A., "Efficiency analysis of a high-specific impulse Hall thruster," *40th AIAA/ASME/SAE/ASEE Joint Propulsion Conference and Exhibit*, 2004, p. 3602.

[108] Hofer, R. R., Peterson, P. Y., Gallimore, A. D., and Jankovsky, R. S., "A high specific impulse two-stage Hall thruster with plasma lens focusing," IEPC-01-036, 27th International Electric Propulsion Conference, Pasadena, CA, 2001.

[109] Hofer, R. and Jankovsky, R., "A Hall thruster performance model incorporating the effects of a multiply-charged plasma," *37th Joint Propulsion Conference and Exhibit*, 2001, p. 3322.

[110] Garrigues, L., Boyd, I. D., and Boeuf, J., "Computation of Hall thruster performance," *Journal of Propulsion and Power*, Vol. 17, No. 4, 2001, pp. 772–779.

[111] Hofer, R., Goebel, D., Mikellides, I., and Katz, I., "Design of a laboratory Hall thruster with magnetically shielded channel walls, phase II: Experiments," *48th AIAA/ASME/SAE/ASEE Joint Propulsion Conference & Exhibit*, 2012, p. 3788.

[112] Hofer, R. R., Jorns, B., Polk, J., Mikellides, I., and Snyder, J., "Wear test of a magnetically shielded Hall thruster at 3000 seconds specific impulse," *33rd International Electric Propulsion Conference*, 2013, pp. 1–24.

[113] Mikellides, I. G., Hofer, R. R., Katz, I., and Goebel, D. M., "Magnetic shielding of Hall thrusters at high discharge voltages," *Journal of Applied Physics*, Vol. 116, No. 5, 2014, pp. 053302.

[114] Dunaevsky, A., Raitses, Y., and Fisch, N. J., "Secondary electron emission from dielectric materials of a Hall thruster with segmented electrodes," *Physics of Plasmas*, Vol. 10, No. 6, 2003, pp. 2574–2577.

[115] Hobbs, G. and Wesson, J., "Heat flow through a Langmuir sheath in the presence of electron emission," *Plasma Physics*, Vol. 9, No. 1, 1967, pp. 85.

[116] Garnier, Y., Viel, V., Roussel, J.-F., and Bernard, J., "Low-energy xenon ion sputtering of ceramics investigated for stationary plasma thrusters," *Journal of Vacuum Science & Technology A: Vacuum, Surfaces, and Films*, Vol. 17, No. 6, 1999, pp. 3246–3254.

[117] Kamhawi, H., Huang, W., Haag, T., Shastry, R., Soulas, G., Smith, T., Mikellides, I., and Hofer, R., "Performance and Thermal Characterization of the NASA-300MS 20 kW Hall Effect Thruster," 2013.

[118] Conversano, R., Goebel, D., Hofer, R., Mikellides, I., Katz, I., and Wirz, R., "Development and Validation Overview for the Design of Low Power Magnetically Shielded Hall Thrusters," *62nd JANNAF Propulsion Meeting*, JANNAF Nashville, TN, 2015.

[119] Grimaud, L. and Mazouffre, S., "Ion behavior in low-power magnetically shielded and unshielded Hall thrusters," *Plasma Sources Science and Technology*, Vol. 26, No. 5, 2017, pp. 055020.

[120] Grimaud, L. and Mazouffre, S., "Performance comparison between standard and magnetically shielded 200 W Hall thrusters with BN-SiO 2 and graphite channel walls," *Vacuum*, Vol. 155, 2018, pp. 514–523.

[121] Goebel, D. M., Hofer, R. R., Mikellides, I. G., Katz, I., Polk, J. E., and Dotson, B. N., "Conducting wall Hall thrusters," *IEEE Transactions on Plasma Science*, Vol. 43, No. 1, 2015, pp. 118–126.

[122] Grimaud, L. and Mazouffre, S., "Conducting wall Hall thrusters in magnetic shielding and standard configurations," *Journal of Applied Physics*, Vol. 122, No. 3, 2017, pp. 033305.

[123] Hofer, R. R., Cusson, S. E., Lobbia, R. B., and Gallimore, A. D., "The H9 Magnetically Shielded Hall Thruster," *35th International Electric Propulsion Conference*, 2017.

[124] Hofer, R., Polk, J., Mikellides, I., Lopez Ortega, A., Conversano, R., Chaplin, V., Lobbia, R., Goebel, D., Kamhawi, H., Verhey, T., et al., "Development Status of the 12.5 kW Hall Effect Rocket with Magnetic Shielding (HERMeS)," *35th International Electric Propulsion Conference, IEPC-2017-231, Atlanta, GA*, 2017.

[125] Hofer, R. R., Polk, J. E., Sekerak, M. J., Mikellides, I. G., Kamhawi, H., Sarver-Verhey, T. R., Herman, D. A., and Williams, G., "The 12.5 kW Hall effect rocket with magnetic shielding (HERMeS) for the asteroid redirect robotic mission," *52nd AIAA/SAE/ASEE Joint Propulsion Conference*, 2016, p. 4825.

[126] Herman, D. A., Santiago, W., Kamhawi, H., Polk, J. E., Snyder, J. S., Hofer, R. R., and Sekerak, M. J., "The Ion Propulsion System for the Asteroid Redirect Robotic Mission," *52nd AIAA/SAE/ASEE Joint Propulsion Conference*, 2016, p. 4824.

[127] Snyder, J. S., Lock, R. E., Manzella, D., Nicholas, A., Lisman, D., and Woolley, R., "Additional mission applications for NASA's 13.3-kW Ion propulsion system," *2016 IEEE Aerospace Conference*, IEEE, 2016, pp. 1–13.

[128] Jankovsky, R., Tverdokhlebov, S., and Manzella, D., "High power Hall thrusters," *35th Joint Propulsion Conference and Exhibit*, 1999, p. 2949.

[129] Hall, S. J., Jorns, B., Gallimore, A., and Hofer, R. R., "Expanded Thruster Mass Model Incorporating Nested Hall Thrusters," *53rd AIAA/SAE/ASEE Joint Propulsion Conference*, 2017, p. 4729.

[130] Liang, R. and Gallimore, A., "Constant-Power Performance and Plume Properties of a Nested-Channel Hall-Effect Thruster," *32nd International Electric Propulsion Conference, IEPC-2011-030, Wiesbaden, Germany*, Vol. 79, 2011, p. 97.

[131] Liang, R., *The Combination of Two Concentric Discharge Channels into a Nested Hall-Effect Thruster*, Ph.D. thesis, University of Michigan, 2013.

[132] "Electric Rocket Engines for Spacecraft," *Machinostroenie, Moscow, USSR*, 1989.

[133] "Shared Magnetic Hall Thruster," *NASA SBIR/STTR Technologies*, 2006.

[134] Szabo, J., Pote, B., Hruby, V., Byrne, L., Tadrake, R., Kolencik, G., Kamhawi, H., and Haag, T., "A commercial one Newton Hall effect thruster for high power in-space missions," *47th AIAA/ASME/SAE/ASEE Joint Propulsion Conference & Exhibit*, 2011, p. 6152.

[135] Liang, R. and Gallimore, A. D., "A 6-kW Laboratory Hall Thruster with Two Concentric Discharge Channels," *31st International Electric Propulsion Conference*, 2009.

[136] Liang, R. and Gallimore, A., "Performance of a Laboratory Hall Thruster with Two Concentric Discharge Channels," *57th Joint Army Navy NASA Air Force (JANNAF) Propulsion Meeting*, 2010.

[137] Liang, R. and Gallimore, A., "Far-field plume measurements of a nested-channel hall-effect thruster," 2011.

[138] Florenz, R., Gallimore, A. D., and Peterson, P. Y., "Developmental status of a 100-kW class laboratory nested channel hall thruster," *32nd International Electric Propulsion Conference, Wiesbaden, Germany*, 2011, pp. 1–9.

[139] Florenz, R. E., *The X3 100-kW Class Nested-Channel Hall Thruster: Motivation, Implementation, and Initial Performance*, Ph.D. Dissertation, University of Michigan, Ann Arbor, MI, 2013.

[140] Florenz, R. E., Hall, S. J., Gallimore, A. D., Kamhawi, H., Griffiths, C. M., Brown, D. L., Hofer, R. R., and Polk, J. E., "First firing of a 100-kW nested-channel hall thruster," *33rd International Electric Propulsion Conference*, 2013.

[141] Hall, S. J., Florenz, R. E., Gallimore, A. D., Kamhawi, H., Brown, D. L., Polk, J. E., Goebel, D. M., and Hofer, R. R., "Implementation and Initial Validation of a 100-kW Class Nested-channel Hall Thruster," *AIAA*, Vol. 3815, 2014, pp. 28–30.

[142] Hall, S. J., Florenz, R. E., Gallimore, A. D., Kamhawi, H., Brown, D., Peterson, P. Y., Polk, J., and Hofer, R. R., "Design Details of a 100-kW class Nested-Channel Hall Thruster," *62nd Joint Army Navy NASA Air Force (JANNAF) Propulsion Meeting*, 2015.

[143] Hall, S. J., Cusson, S. E., and Gallimore, A. D., "30-kW Performance of a 100-kW Class Nested-channel Hall Thruster," *34th International Electric Propulsion Conference*, 2015.

[144] Hall, S. J., *Characterization of a 100-kW Class Nested-Channel Hall Thruster*, Ph.D. Dissertation, University of Michigan, Ann Arbor, MI, 2017.

[145] Hall, S. J., Jorns, B., Gallimore, A. D., Kamhawi, H., Haag, T. W., Mackey, J. A., Gilland, J. H., Peterson, P. Y., and Baird, M. J., "High-Power Performance of a 100-kW Class Nested Hall Thruster," *35th International Electric Propulsion Conference*, 2017.

[146] Hofer, R. R., Jankovsky, R. S., and Gallimore, A. D., "High-specific impulse Hall thrusters, part 1: influence of current density and magnetic field," *Journal of Propulsion and Power*, Vol. 22, No. 4, 2006, pp. 721–731.

[147] NASA, "Next Space Technologies for Exploration Partnerships Broad Agency Announcement," 2014.

[148] Jorns, B., Gallimore, A., Hall, S. J., Goebel, D. M., Shark, S., and Welander, B., "Update on the Nested Hall Thruster Subsystem for the NextSTEP XR-100 Program," *2018 Joint Propulsion Conference*, 2018, p. 4418.

[149] Shark, S. W., Hablitzel, S. T., Tolentino, A., Welander, B. A., Jackson, J., Hall, S. J., Gilland, J. H., Jorns, B., and Hofer, R. R., "High Power Demonstration of a 100 kW Nested Hall Thruster System," *AIAA Propulsion and Energy 2019 Forum*, 2019, p. 3809.

[150] Frieman, J. D., Liu, T. M., and Walker, M. L., "Background flow model of Hall thruster neutral ingestion," *Journal of Propulsion and Power*, Vol. 33, No. 5, 2017, pp. 1087–1101.

[151] Georgin, M. P., Dhaliwal, V., and Gallimore, A., "Investigation of channel interactions in a nested Hall thruster part i: Acceleration region velocimetry," *52nd AIAA/SAE/ASEE Joint Propulsion Conference*, 2016, p. 5030.

[152] Cusson, S., Hofer, R., Lobbia, R., Jorns, B., and Gallimore, A., "Performance of the H9 Magnetically Shielded Hall Thrusters," *35th International Electric Propulsion Conference, IEPC-2017-239, Atlanta, GA*, 2017.

[153] Haas, J. M., Hofer, R. R., Brown, D. L., Reid, B. M., and Gallimore, A. D., "Design of the H6 Hall Thruster for High Thrust/Power Investigation," *54th JANNAF Propulsion Meeting, Denver, CO*, 2007, pp. 14–17.

[154] Hofer, R. R., Goebel, D. M., and Watkins, R. M., "Compact high current rare-earth emitter hollow cathode for hall effect thrusters," March 27 2012, US Patent 8,143,788.

[155] Hofer, R., Goebel, D., and Watkins, R., "Compact LaB6 Hollow Cathode for the 6-kW Hall Thruster," *54th JANNAF Propulsion Meeting*, pp. 14–17.

[156] Goebel, D., Jameson, K. K., and Hofer, R. R., "Hall thruster cathode flow impact on coupling voltage and cathode life," *Journal of Propulsion and Power*, Vol. 28, No. 2, 2012, pp. 355–363.

[157] Reid, B., Gallimore, A., Hofer, R., Li, Y., and Haas, J., "Anode design and verification for a 6-kW Hall thruster," *JANNAF Journal of Propulsion and Energetics*, Vol. 3, No. 1, 2010, pp. 29–43.

[158] Katz, I., Lopez Ortega, A., Goebel, D. M., Sekerak, M. J., Hofer, R. R., Jorns, B. A., and Brophy, J. R., "Effect of solar array plume interactions on Hall thruster cathode common potentials," 2016.

[159] Hofer, R. R., Jorns, B. A., Katz, I., and Brophy, J. R., "Hall effect thruster electrical configuration," Oct. 5 2017, US Patent App. 15/474,480.

[160] Mikellides, I. G. and Ortega, A. L., "2D (r–z) numerical simulations of the plasma and channel erosion in a 100 kW class nested Hall thruster," *Plasma Sources Science and Technology*, Vol. 27, No. 7, 2018, pp. 075001.

[161] Cusson, S., Hall, S., Hofer, R., Jorns, B., and Gallimore, A., "The Impact of Magnetic Field Coupling Between Channels in a Nested Hall Thruster," *Proceedings of the 35th International Electric Propulsion Conference, Atlanta, Georgia*, 2017.

[162] Florenz, R., *The X3 100-kW Class Nested-Channel Hall Thruster: Motivation, Implementation, and Initial Performance*, Ph.D. thesis, University of Michigan, 2014.

[163] Sekerak, M., Hofer, R., Polk, J., Jorns, B., and Mikellides, I., "Wear testing of a magnetically shielded hall thruster at 2000 s specific impulse," *34th International Electric Propulsion Conference, IEPC-2015-155, Kobe, Japan*, 2015.

[164] Trent, K. R., McDonald, M. S., Lobbia, R. B., and Gallimore, A. D., "Time-resolved Langmuir probing of a new lanthanum hexaboride (LaB6) hollow cathode," Tech. rep., MICHIGAN UNIV ANN ARBOR PLASMA DYNAMICS AND ELECTRIC PROPULSION LAB, 2011.

[165] Dankanich, J. W., Walker, M., Swiatek, M. W., and Yim, J. T., "Recommended practice for pressure measurement and calculation of effective pumping speed in electric propulsion testing," *Journal of Propulsion and Power*, Vol. 33, No. 3, 2016, pp. 668–680.

[166] Haag, T. W., "Thrust stand for high-power electric propulsion devices," *Review of Scientific Instruments*, Vol. 62, No. 5, 1991, pp. 1186–1191.

[167] Xu, K. G. and Walker, M. L., "High-power, null-type, inverted pendulum thrust stand," *Review of Scientific Instruments*, Vol. 80, No. 5, 2009, pp. 055103.

[168] Dragnea, H., *Development and Application of Multidimensional Computational Models for Hall Thrusters*, Ph.D. thesis, University of Michigan, 2018.

[169] Rovey, J. L., Walker, M. L., Gallimore, A. D., and Peterson, P. Y., "Magnetically filtered Faraday probe for measuring the ion current density profile of a Hall thruster," *Review of Scientific Instruments*, Vol. 77, No. 1, 2006, pp. 013503.

[170] Reid, B. M. and Gallimore, A. D., "Near-field ion current density measurements of a 6-kW Hall thruster," *31st International Electric Propulsion Conference, IEPC-2009-124, Ann Arbor, MI*, 2009.

[171] Cedolin, R., Hargus Jr, W., Storm, P., Hanson, R., and Cappelli, M., "Laser-induced fluorescence study of a xenon Hall thruster," *Applied Physics B*, Vol. 65, No. 4-5, 1997, pp. 459–469.

[172] Mazouffre, S., "Laser-induced fluorescence diagnostics of the cross-field discharge of Hall thrusters," *Plasma Sources Science and Technology*, Vol. 22, No. 1, 2012, pp. 013001.

[173] Chaplin, V. H., Conversano, R. W., Lobbia, R. B., Ortega, A. L., Mikellides, I. G., Hofer, R. R., and Jorns, B. A., "Laser-Induced Fluorescence Measurements of the Acceleration Zone in the 12.5 kW HERMeS Hall Thruster," *35th International Electric Propulsion Conference*, Vol. 229, 2017, pp. 8–12.

[174] Spektor, R., Tighe, W., Stoltz, P., and Beckwith, K., "Facility Effects on Hall Thruster Performance Through Cathode Coupling," *Proc. 34rd Int. Electric Propulsion Conf., Kobe*, 2015.

[175] Huang, W., Kanhawi, H., and Herman, D., "Ion Velocity Distribution in the Channel and Near-Field of the HERMeS Hall Thruster," *AIAA paper*, 2018.

[176] Shastry, R., Huang, W., and Kamhawi, H., "Near-Surface Plasma Characterization of the 12.5-kW NASA TDU1 Hall Thruster," *51st AIAA/SAE/ASEE Joint Propulsion Conference*, 2015, p. 3919.

[177] Mazouffre, S. and Bourgeois, G., "Spatio-temporal characteristics of ion velocity in a Hall thruster discharge," *Plasma Sources Science and Technology*, Vol. 19, No. 6, 2010, pp. 065018.

[178] Mikellides, I. G., Lopez-Ortegra, A., Chaplin, V. H., Snyder, J. S., and Lenguito, G., "Mechanism Behind the Dependence of Thrust on Facility Backpressure and Implications on the Operation of the SPT-140 Onboard the Psyche Mission," *36th International Electric Propulsion Conference*, 2019.

[179] Goebel, D. M. and Chu, E., "High-current lanthanum hexaboride hollow cathode for high-power hall thrusters," *Journal of Propulsion and Power*, Vol. 30, No. 1, 2013, pp. 35–40.

[180] Goebel, D. M., Becatto, G., Reilly, S., Tilley, K., and Hall, S., "High Current Lanthanum Hexaboride Hollow Cathode for 20-200 kW Hall Thrusters," 2017.

[181] Lopez-Ortegra, A., Mikellides, I. G., Chaplin, V. H., Snyder, J. S., and Lenguito, G., "Facility Pressure Effects on a Hall Thruster with an External Cathode, I: Numerical Simulations," *36th International Electric Propulsion Conference*, 2019.

[182] Huang, W., Drenkow, B., and Gallimore, A., "Laser-induced fluorescence of singly-charged xenon inside a 6-kW Hall thruster," *45th AIAA/ASME/SAE/ASEE Joint Propulsion Conference & Exhibit*, 2009, p. 5355.

[183] Sekerak, M. J., Gallimore, A. D., Brown, D. L., Hofer, R. R., and Polk, J. E., "Mode transitions in Hall-effect thrusters induced by variable magnetic field strength," *Journal of Propulsion and Power*, 2016, pp. 903–917.

[184] Boeuf, J. and Garrigues, L., "Low frequency oscillations in a stationary plasma thruster," *Journal of Applied Physics*, Vol. 84, No. 7, 1998, pp. 3541–3554.

[185] Choueiri, E., "Plasma oscillations in Hall thrusters," *Physics of Plasmas*, Vol. 8, No. 4, 2001, pp. 1411–1426.

[186] Chesta, E., Lam, C. M., Meezan, N. B., Schmidt, D. P., and Cappelli, M. A., "A characterization of plasma fluctuations within a Hall discharge," *IEEE transactions on plasma science*, Vol. 29, No. 4, 2001, pp. 582–591.

[187] McDonald, M. S. and Gallimore, A. D., "Rotating spoke instabilities in Hall thrusters," *IEEE Transactions on Plasma Science*, Vol. 39, No. 11, 2011, pp. 2952–2953.

[188] Su, L., Hall, S., Cusson, S., and Jorns, B., "Model for the Increase in Thruster Efficiency from Cross-Channel Coupling in Nested Hall Thrusters," *36th International Electric Propulsion Conference*, 2019.

[189] Ducrocq, A., Adam, J., Héron, A., and Laval, G., "High-frequency electron drift instability in the cross-field configuration of Hall thrusters," *Physics of Plasmas*, Vol. 13, No. 10, 2006, pp. 102111.

[190] Tsikata, S., Lemoine, N., Pisarev, V., and Gresillon, D., "Dispersion relations of electron density fluctuations in a Hall thruster plasma, observed by collective light scattering," *Physics of Plasmas*, Vol. 16, No. 3, 2009, pp. 033506.

[191] Cavalier, J., Lemoine, N., Bonhomme, G., Tsikata, S., Honoré, C., and Gresillon, D., "Hall thruster plasma fluctuations identified as the E× B electron drift instability: Modeling and fitting on experimental data," *Physics of Plasmas*, Vol. 20, No. 8, 2013, pp. 082107.

[192] Héron, A. and Adam, J., "Anomalous conductivity in Hall thrusters: Effects of the non-linear coupling of the electron-cyclotron drift instability with secondary electron emission of the walls," *Physics of Plasmas*, Vol. 20, No. 8, 2013, pp. 082313.

[193] Shastry, R., Hofer, R. R., Reid, B. M., and Gallimore, A. D., "Method for analyzing E× B probe spectra from Hall thruster plumes," *Review of Scientific Instruments*, Vol. 80, No. 6, 2009, pp. 063502.

[194] Jameson, K. K., *Investigation of hollow cathode effects on total thruster efficiency in a 6 kW Hall thruster*, Ph.D. thesis, University of California, Los Angeles, 2008.

[195] Randolph, T. and Polk, J., "An overview of the nuclear electric xenon ion system (NEXIS) activity," *40th AIAA/ASME/SAE/ASEE Joint Propulsion Conference and Exhibit*, 2004, p. 3450.

[196] Hofer, R. R., Goebel, D. M., Snyder, J. S., and Sandler, I., "BPT-4000 hall thruster extended power throttling range characterization for NASA science missions," *31st International Electric Propulsion Conference, IEPC-2009-085, Ann Arbor, MI*, 2009.

[197] de Grys, K., Meckel, N., Callis, G., Greisen, D., Hoskins, A., King, D., Wilson, F., Werthman, L., and Khayms, V., "Development and testing of a 4500 watt flight type Hall thruster and cathode," *IEPC Paper*, 2001, pp. 01–011.

[198] Boyd, I. D., Van Gilder, D. B., and Liu, X., "Monte Carlo simulation of neutral xenon flows in electric propulsion devices," *Journal of propulsion and power*, Vol. 14, No. 6, 1998, pp. 1009–1015.

[199] Bird, G. A. and Brady, J., *Molecular gas dynamics and the direct simulation of gas flows*, Vol. 5, Clarendon press Oxford, 1994.

[200] Jorns, B. A. and Hofer, R. R., "Plasma oscillations in a 6-kW magnetically shielded Hall thruster," *Physics of Plasmas*, Vol. 21, No. 5, 2014, pp. 053512.